Discovery of the Higgs boson and study of its properties using photons and leptons with the ATLAS experiment at the LHC

Marine Kuna

▶ **To cite this version:**

Marine Kuna. Discovery of the Higgs boson and study of its properties using photons and leptons with the ATLAS experiment at the LHC. High Energy Physics - Experiment [hep-ex]. Université Grenoble Alpes, 2019. tel-02180385

HAL Id: tel-02180385
https://theses.hal.science/tel-02180385

Submitted on 11 Jul 2019

HAL is a multi-disciplinary open access archive for the deposit and dissemination of scientific research documents, whether they are published or not. The documents may come from teaching and research institutions in France or abroad, or from public or private research centers.

L'archive ouverte pluridisciplinaire **HAL**, est destinée au dépôt et à la diffusion de documents scientifiques de niveau recherche, publiés ou non, émanant des établissements d'enseignement et de recherche français ou étrangers, des laboratoires publics ou privés.

Communauté Université Grenoble Alpes

HABILITATION À DIRIGER DES RECHERCHES

Spécialité : **Physique Subatomique et Astroparticules**

présentée par

Marine KUNA

Discovery of the Higgs boson and study of its properties using photons and leptons with the ATLAS experiment at the LHC

soutenue publiquement le 26 Juin 2019 devant le jury composé de

Président :	Pr.	Johann Collot	Université Grenoble Alpes
Rapporteurs :	Dr.	Guillaume Unal	CERN
	Dr.	Anne-Catherine Le Bihan	IPHC
	Pr.	Pierre Savard	Université de Toronto
Examinateur :	Dr.	Arnaud Lucotte	LPSC

Table of contents

Index

1. Introduction

1.1 Scope of this HDR

This ***Habilitation à diriger des recherches*** **(HDR)** is an overview of the research activities I carried out since the defence of my PhD thesis in October 2010. Because it takes place within the framework of the ATLAS collaboration, this content benefits from being put into the perspective of the LHC data taking schedule which timeline is illustrated on Figure 1.1 and put in parallel with my activities on Table 1.1.

When writing this document, one of my intention was for it to be self-explanatory and not too obscure to scientists who are not experts to the field of particle physics. In the attempt to be understandable to a wider audience, I included an index at the beginning of the document which the reader is encouraged to make use whenever facing an unclear terminology.

This HDR is structured in three distinct thematic parts that also unroll chronologically.

Part I describes all of my activities involving physics with photons. After providing necessary introductory notions about how photons are reconstructed, identified and isolated in ATLAS (2.1), it relates my involvement in the photon efficiency (2.2) and the standard model di-photon cross section (2.3) measurements, and finally for my part in the search and discovery of the Higgs boson (3.1) as well as the measurement of its first properties, specifically its spin (3.2). This corresponds to my first post-doc at the Laboratoire de Physique Nucléaire et des hautes Énergies (LPNHE) in Paris which covers a period of time from early 2011 to mid-2013 and a dataset of 37 pb^{-1} of 7 TeV data and $\simeq$ 25 fb^{-1} of 7 and 8 TeV data.

From mid-2013 until mid-2017 I was employed by the University of Rome, La Sapienza, and then very briefly by the University of Texas Austin, being based in Italy for two years and then at CERN as a simi-fellow for another two years. During that entire time I focused my efforts towards the observation of the Higgs boson produced in association with a pair of top quarks ($t\bar{t}H$) in view of the top-to-Higgs Yukawa coupling measurement. Part II of this document is dedicated to explaining my interest and contributions to the $t\bar{t}H$ process by first providing motivations for it in chapter 4, then detailing in chapter 5 the final state with leptons which has been my focus, to finally put it into the perspective of my contributions to the $t\bar{t}H$ statistical combination of all final states and providing it for general Higgs bosons couplings measurements in chapter 6, which also include the adaptation of the analysis into a search for beyond standard model flavour changing neutral currents. These results use LHC data ranging from the $\simeq$ 24 fb^{-1} of Run 1 to 80 fb^{-1} of Run 2 data.

The analysis of the totality of the 140 fb^{-1} of Run 2 data and preparation for Run 3 is treated in part III of this HDR as my research project and plans. It encloses a chapter about possible improvements of the $t\bar{t}H \rightarrow$ ML analysis (chapter 7), prospects about the future of Higgs boson couplings measurements (chapter 9) and potential object reconstruction performance

improvements (chapter 8). These future activities will take place at the Laboratoire de Physique des Particules et de Cosmologie (LPSC) in Grenoble and University Grenoble Alpes where I was hired as a Maître de conférence in September 2017.

All of this research took place within the ATLAS experiment. The detector as well as problematic of pile-up at the LHC is quickly described in sections 1.2.1 and 1.2.2. The theoretical context around the Higgs boson that captures most of the topics treated in this HDR is explained in section 1.2.3.

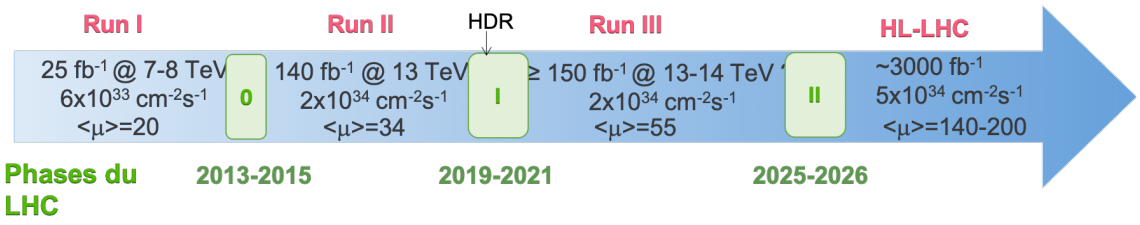

FIGURE 1.1 – Time-wise position of the HDR with respect to the LHC schedule.

Year	Run #	$\sqrt{s}$	$\mathcal{L}$	$\langle\mu\rangle$	Documentation
2007	Cosmic muons				Thesis [1]
2008	Splash events				
2009	First collisions	900 GeV	9 μb^{-1}		
2010	Run I	7 TeV	37 pb^{-1}	9.1	$H \to \gamma\gamma$ I
2011			4 fb^{-1}		
2012		8 TeV	20 fb^{-1}	20.7	$t\bar{t}H$ II
2013-14	Shutdown				
2015	Run II	13 TeV	3 fb^{-1}	13.4	$t\bar{t}H$ II
2016			33 fb^{-1}	25.1	
2017			44 fb^{-1}	37.8	
2018			59 fb^{-1}	37.3	Project III
2019-2020	Shutdown				
2021	Run III	13/13.5/14 TeV ?	150 fb^{-1} ?	55 ?	Project III

TABLE 1.1 – Summary of ATLAS recorded LHC data, integrated luminosity ($\mathcal{L}$), average number of interactions per bunch crossing ($\langle\mu\rangle$) and chronology of work.

1.2 General introductory notions

1.2.1 Instrumental setup

The ATLAS [1] experiment [2] is one of the four detectors (ALICE, LHCb, CMS, ATLAS) of the proton-proton collider LHC [2] at CERN [3], Geneva. ATLAS is a multipurpose particle detector with a forward-backward symmetric cylindrical geometry and nearly 4π coverage in solid angle. It uses a right-handed coordinate system with its origin at the nominal interaction point (IP) in the centre of the detector and the z-axis along the beam pipe. The x-axis points from the IP to the centre of the LHC ring, and the y-axis points upwards. Cylindrical coordinates (r, ϕ) are used in the transverse plane, ϕ being the azimuthal angle around the z-axis. The pseudo-rapidity η is defined in terms of the polar angle θ as η = -$ln(tan(\frac{\theta}{2}))$. Angular distance is measured in units of $\Delta R = \sqrt{\Delta\eta^2 + \Delta\phi^2}$ (see Figure 1.2b).

ATLAS consists of an inner tracking detector surrounded by a superconducting solenoid providing a 2 Tesla axial magnetic field, electromagnetic and hadron calorimeters, and a muon spectrometer (see Figure 1.2a). The inner tracking detector, covering the pseudo-rapidity range $|\eta| < 2.5$, is made of silicon pixel and silicon microstrip tracking (SCT) detectors inside a transition-radiation tracker (TRT) that covers $|\eta|$=2.0. It includes since run 2 a newly installed innermost pixel layer, the insertable B-layer. Lead/liquid-argon (LAr) sampling calorimeters, also called EM calorimeters provide electromagnetic (EM) energy measurements up to $|\eta|$ <3.2, from which up to $|\eta|$ <2.5 with high granularity and longitudinal segmentation thanks to the presence of the first layer. A hadron calorimeter consisting of steel and scintillator tiles covers the central pseudo-rapidity range ($|\eta|$ <1.7). The end-cap and forward regions are instrumented with LAr calorimeters for EM and hadronic energy measurements up to $|\eta|$=4.9. The muon spectrometer surrounds the calorimeters and is based on three large air-core toroid superconducting magnets with eight coils each. It includes a system of precision tracking chambers ($|\eta|$ <2.7) and fast detectors for triggering ($|\eta|$ <2.4). A two-level trigger system is used to select events. The first-level trigger is implemented in hardware and uses a subset of the detector information to reduce the accepted rate to a design maximum of 100 kHz. This is followed by a software-based trigger with a sustained average accepted event rate of about 1 kHz.

From 2026, a high luminosity upgrade of the LHC, the HL-LHC is expected to provide collisions with a few times higher instantaneous luminosity (see figure 1.1). Luminosity levelling will be used, that modifies the beam characteristics, like crossing angle and focus, to momentarily lower the instantaneous luminosity at the beginning of runs in order not to go beyond upper limits tolerated by triggers. Thanks to this technique, the average, and therefore the integrated luminosity is expected to be much larger. All experiments are preparing for their instruments to be ready for this phase. In particular, ATLAS inner tracker will be entirely replaced during the phase 2 shutdown. France is highly involved in the construction of the new all-silicon inner tracker (ITK), designed to cope with the increased occupancy and radiation environment while improving the tracking performance. The analyses described in this document rely on the comparison of Monte Carlo simulations (MC) with LHC data to establish the existence of new particles, and properties of existing production and decay processes. Particles are produced by generators (MadGraph5_aMC@NLO [3], Powheg [4], Sherpa [5, 6] ...), pass through showering algorithms (Pythia 6/8 [7, 8], Herwig++/7 [9] ...), and in a third step interact with a full simulation of the

1. A Toroïdal LHC ApparatuS
2. LArge Hadron Collider
3. the European Organization for Nuclear Research

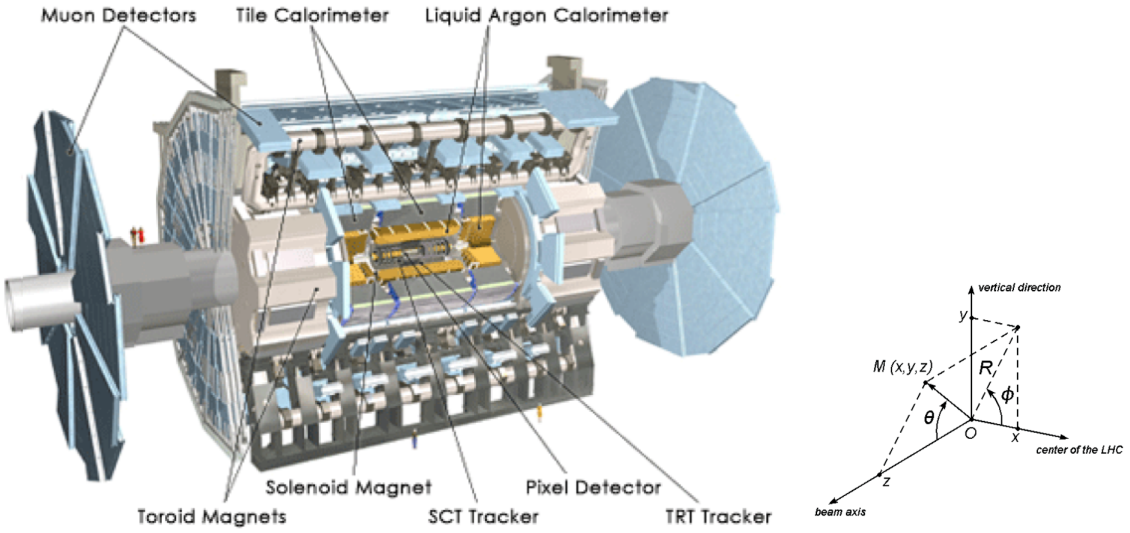

(a) ATLAS detector (b) $\eta = ln(tan(\frac{\theta}{2}))$

FIGURE 1.2 – ATLAS sub-detectors scheme and coordinate system .

above described ATLAS detector based on GEANT4 [10].

The LHC being a hadron collider, events of interest are buried in a background of low momentum strong interactions on top of the hard-scattering processes. Underlying events are multiple interactions and initial or final state radiation (ISR/FSR) arising from the same pair of colliding protons as the process of interest. Pile-up or minimum bias entails anything produced by proton-proton collisions in the same and nearby bunch crossings outside the p-p process of interest.

Simulated events are generated and reweighed to match the pile-up conditions observed in the data and are reconstructed using the same procedure as for the data (see section 1.2.2).

The work described in this document is entirely obtained analysing collision data recorded by the ATLAS experiment. Results are often compared to equivalent studies performed by similar multipurpose experiments, either based on previous generations of colliders like LEP [4] and the TeVatron [5] for D0 and CDF, or from the LHC-based CMS (Compact Muon Solenoïd) built together with ATLAS to fully validate discoveries with two independent datasets and instrumental setups.

1.2.2 Luminosity and in time pile-up

The luminosity, expressed in inverse barns (where 1 barn = 10^{-24} cm^2), is given by $\mathscr{L} = \frac{n_b \langle \mu \rangle}{\sigma_{inel}}$ where n_b is the number of bunch crossings, $\langle \mu \rangle$ is the bunch-averaged pile-up parameter and σ_{inel} is the cross section of inelastic proton-proton collisions. Luminosity measurement at the ATLAS detector is detailed in [11]. In-time pile-up, due to the increase of the instantaneous luminosity and thus the occurrence of more numerous interactions per bunch crossing (see Figure 1.3), causes an accumulation of tracks in the inner tracker and muon chambers, and an accumulation

4. Large Electron Positron collider at CERN (1989-2000), most powerful lepton collider built up to date ($\sqrt{s}$=209 GeV) and its four detectors : ALEPH, OPAL, L3 et DELPHI.

5. Proton anti-proton collider at Fermilab in Chicago (1987-2011) with an energy in the centre of mass close to 2 TeV

of energy deposits in the calorimeters. Sub-detectors are also sensitive to the out-of-time pile-up arising from the collisions period (a bunch collision every 25 ns, ie a frequency of 40 MHz) being shorter than sub-detectors response time, that is the time spent going back to their baseline.

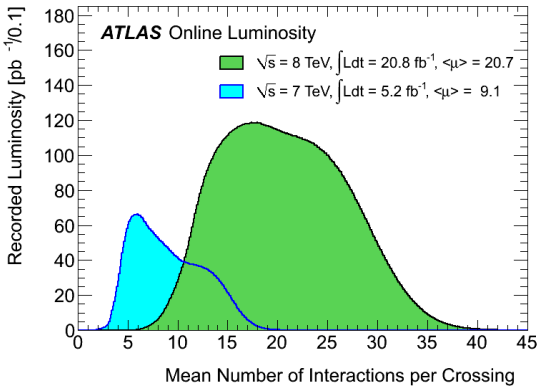

(a) Run 1 $< \mu >$ 2011-2012

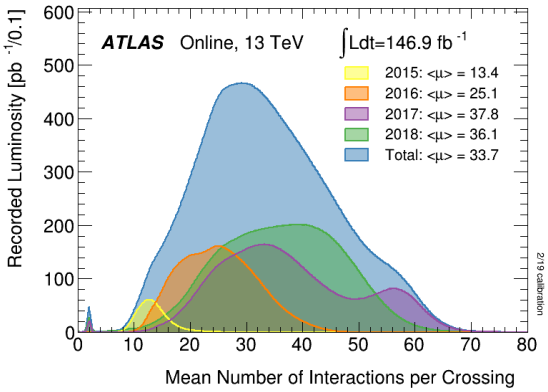

(b) Run 2 $< \mu >$ 2015-2018

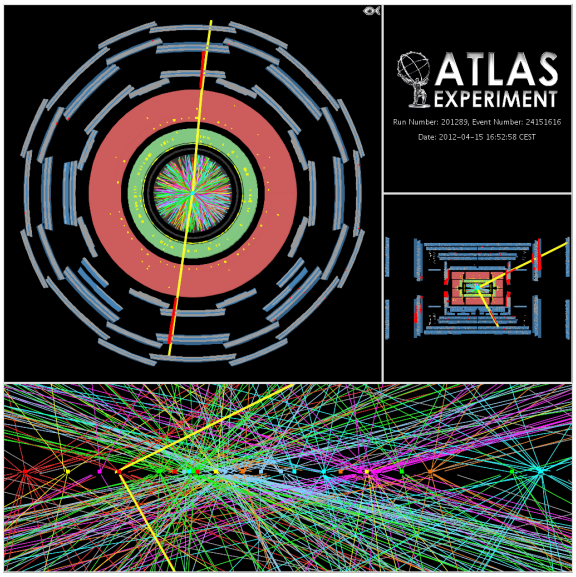

(c) $N_{vtx} = 25$ Event display

FIGURE 1.3 – Average number of interactions per bunch crossing $\langle \mu \rangle$ for run 1 (top left) and run 2 (right) [12] and example of an event display for a $Z \rightarrow e^+e^-$candidate with a number of vertices $N_{vtx} = 25$ (bottom) [13]

1.2.3 Theoretical context

As one of the major items on the LHC physics program, and the main topic of study of this document, the theoretical section will focus on the Higgs mechanism. Indeed a large part of my work is related to the discovery of the Higgs boson (Section 3.1) and the study of its properties : in particular the spin (Section 3.2) and coupling to top quark (Section II) which motivation to measure is also provided here.

Until 2012, the Standard Model of particle physics was almost complete apart from the unexplained observed masses for the $W^{\pm}$ and Z^0 bosons, which are expected to be massless in order to respect the gauge invariance of the electro-weak group $SU(2)_L \times U(1)_Y$. An electro-weak symmetry breaking mechanism (EWSB) must be introduced in order to explain that only the electro-magnetic group remains invariant, the photon being massless : $SU(2)_L \times U(1)_Y \rightarrow U(1)_{EM}$. One of the mechanisms to break electro-weak symmetry breaking is to introduce a Higgs field giving their mass to the other elementary particles. This field was theoretically predicted in 1964 by Higgs, Englert and Brout [14, 15, 16, 17, 18, 19]. The simplest field needed for the symmetry breaking is a complex doublet of scalar fields :

$$\phi = \begin{pmatrix} \phi^+ = \frac{\phi_1 + i\phi_2}{\sqrt{2}} \\ \phi^0 = \frac{\phi_3 + i\phi_4}{\sqrt{2}} \end{pmatrix} \tag{1.1}$$

The Lagrangian $\mathscr{L}_{Higgs}$ of the Higgs field ϕ is given by the subtraction of the kinematic (T) and potential (V) terms :

$$\mathscr{L}_{Higgs} = T - V = (D_\mu \phi)(D^\mu \phi)^\dagger - V(\mid \phi \mid^2) \tag{1.2}$$

where D_μ is the covariant derivative defined as $D_\mu = \partial_\mu - ig'YB_\mu - i\frac{\sigma_a}{2} g W_\mu^a$ ($a = 1...3$), g' and g the respective coupling constants of $U(1)_Y$ and $SU(2)_L$. B_μ and W_μ^a here represent massless gauge bosons, and σ_a are Pauli matrices, representation for the $SU(2)$ group.

Potential term to the Higgs field : Higgs mass, self-coupling and quartic coupling

The Higgs potential is written :

$$V(\phi) = \mu^2 \mid \phi \mid^2 + \lambda \mid \phi \mid^4 \tag{1.3}$$

where μ^2 must be negative in order to have a symmetry breaking as opposed to a minimum of potential for $\phi = 0$, and the quartic coupling λ must be positive in order to ensure the stability of the vacuum. The potential minima are found by solving $\frac{\partial V(\phi)}{\partial \phi} = 0$. A continuum of solutions is found and illustrated in two dimension instead of four by the famous Mexican hat on Figure 1.4. These solutions verify :

$$\sqrt{\mid \phi_{Vmin} \mid^2} = \sqrt{\frac{-\mu^2}{2\lambda}} = \frac{v}{\sqrt{2}} \tag{1.4}$$

where

$$v = \sqrt{-\frac{\mu^2}{\lambda}} \tag{1.5}$$

is the value of the Higgs field in vacuum, or vacuum expectation value (*vev*). Its value is known and measured to be $v = 246$ GeV thanks to its relation to the Fermi constant directly at work in the muon decay $\mu \rightarrow e^- + \bar{\nu}_e + \nu_\mu$, or, modulo other effects, in the well measured radioactive β

decays such as $n \to p + e^- + \bar{\nu}_e$. $G_F \propto \frac{g^2}{m_W^2}$ is proportional to $\frac{1}{m_W^2}$ because a W boson is exchanged, and g^2 because of the presence of two electroweak vertices of amplitude g ($n \to p + W^-$ and $W^- \to e^- + \bar{\nu}_e$). Once the mass of the W boson is injected, one can see the Fermi constant is inversely proportional to the square of the *vev* : $G_F \propto \frac{g^2}{m_W^2} \propto \frac{g^2}{\frac{1}{4}g^2v^2} \propto \frac{4}{v^2}$. The value of the *vev* sets the scale of the electro-weak symmetry breaking around a few hundreds of GeV.

The hypercharge Y is taken to be 1 in equation 1.1, since as it is shown below it allows $U(1)_{EM}$ to stay unbroken. The first component of the Higgs doublet ϕ^+, with an isospin $T_3 = \frac{1}{2}$ has therefore an electric charge $Q = T_3 + \frac{Y}{2} = \frac{1}{2} + \frac{1}{2} = +1$, whereas the ϕ^0 component of isospin $T_3 = -\frac{1}{2}$ is neutral : $Q_{\phi^0} = T_3 + \frac{Y}{2} = -\frac{1}{2} + \frac{1}{2} = 0$. In order for the $U(1)_{EM}$ symmetry to remain unbroken, there must be a local conservation of the electric charge. The vacuum expectation value of ϕ^+ must be 0, and the neutral part of the field must develop around the field minimum v (*vev*) $\phi_3 + i\phi_4 = h + v$. Although the ϕ_3 and ϕ_4 components of the Higgs field can both take part of the vacuum expected value, the field can be rotated with a gauge transformation of any angle so that h becomes real, so that one can attribute the Higgs field entirely to the real component $\phi_3 = h + v$ and set the complex one to zero $\phi_4 = 0$ [6], resulting in :

$$\begin{pmatrix} \phi^+ = 0 \\ \phi^0 = \frac{\phi_3 + i\phi_4}{\sqrt{2}} = \frac{v+h}{\sqrt{2}} \end{pmatrix}$$

The expression once re-injected in the expression of the potential in equation 1.3 implies, when developed and factorised again by orders of the Higgs field h :

$$\begin{aligned} V(\phi) &= \mu^2(v+h)^2 + \lambda(v+h)^4 \\ &= \frac{1}{2}\mu^2(v^2 + \frac{\mu^2}{2}) - \mu^2 h^2 + \frac{\mu^2}{v}h^3 + \frac{\mu^2}{4v^2}h^4 \end{aligned} \tag{1.6}$$

From that expression of the Higgs potential, the term remaining constant as a function of the Higgs boson potential h could be part of the cosmological constant contributing to the vacuum energy [20]. The Higgs mass is attributed to the quadratic term through a canonical normalisation : $\frac{1}{2}m_h^2 = -\mu^2 \implies m_h^2 = -2\mu^2$. The Higgs boson has therefore a mass resulting in the Higgs boson's field coupling with itself :

$$m_h = \sqrt{-2\mu^2} = \sqrt{2\lambda v^2} \tag{1.7}$$

The Higgs boson mass is not determined by theory, but the *vev* is. The free parameter here is λ which is determined once the Higgs boson mass is measured experimentally. The h^3 and h^4 terms are respectively the trilinear and quartic coupling terms, representing the interaction amplitudes of the Higgs boson decaying to two Higgs bosons $H \to HH$ and a four-Higgs-boson interaction $HH \to HH$.

From equation 1.5 the parameter μ can also be expressed in terms of the vev v so that $\mu^2 = -v^2\lambda$, and reinjected in the potential :

$$\begin{aligned} V(\phi) &= C + \lambda v^2 h^2 + \lambda v h^3 + \frac{1}{4}\lambda h^4 \\ &\equiv C + \frac{1}{2}m_h^2 h^2 + \lambda_3 h^3 + \frac{1}{4}\lambda_4 h^4 \end{aligned} \tag{1.8}$$

6. The three fields/degrees of freedom left aside : ϕ_1, ϕ_2 and ϕ_4 result into three Goldstone bosons, absorbed as the longitudinal polarisations of the W^+, W^- and Z^0 bosons.

λ is thereafter called the *quartic coupling* but intervenes also in the Higgs self-coupling term and the Higgs mass term. It appears as a consequence the trilinear Higgs coupling λ_3 and the quartic coupling λ_4 are both entirely determined through the Higgs boson mass measurement $\frac{\lambda_3}{v} = \lambda_4 = \lambda = \frac{m_h^2}{2v^2}$. Any deviation from the expected value of λ means that the Higgs field does not follow a mexican hat potential, which is the motivation for the Higgs self-coupling measurement discussed in section 9.2.

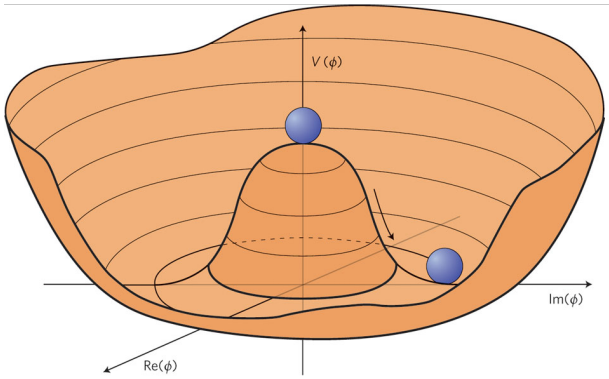

FIGURE 1.4 – Higgs potential in the complex plan.

Kinematic term to the Higgs field : interaction with gauge bosons

When developing the kinematic term from the Higgs lagrangian :

$$(D_\mu\phi)(D^\mu\phi)^\dagger = (\partial_\mu\phi - ig'YB_\mu\phi - i\frac{\sigma_a}{2}gW_\mu^a\phi)(\partial^\mu\phi - ig'qB^\mu\phi - i\frac{\sigma_a}{2}gW^{a,\mu}\phi)^\dagger$$

replacing ϕ by its value $\begin{pmatrix} 0 \\ \frac{v+h}{\sqrt{2}} \end{pmatrix}$, and after simplifications of some arising terms, five types of contributions appear :

- $\frac{1}{2}\partial_\mu\phi\partial^\mu\phi$, that is the propagation term for the Higgs boson h
- $\frac{1}{2}g'^2Y^2B_\mu B^\mu v^2$ ($\frac{1}{8}g^2W_\mu^aW^{a,\mu}v^2$), a mass term for B_μ (W_μ^a). That results in the Higgs field providing a mass to vector bosons and resolving the issue of the electro weak symmetry breaking : $m_B = \sqrt{g'^2Y^2v^2} = g' \mid Y \mid v$
- $\frac{1}{2}g'^2Y^2B_\mu B^\mu hv$, that is a trilinear coupling between h and B_μ, like for instance the decay of the Higgs boson into two B vector bosons with a coupling

$$\lambda_B = g'^2q^2v = \frac{m_B^2}{v} \tag{1.9}$$

  thanks to the expression of m_B stated above.
- $\frac{1}{2}g'^2Y^2B_\mu B^\mu h^2$, that are quartic interactions between two scalars h and two bosons B_μ.

In fact B_μ and W_μ^3 are not the mass eigenstates as they appear to mix through a term $(B_\mu, W_\mu^3)\mathscr{M}^2\begin{pmatrix} B_\mu \\ W_\mu^3 \end{pmatrix}$ where $\mathscr{M}^2$ is a diagonal symmetric matrix. This matrix can be diagonalised

with a rotation by an angle θ_W called the Weak angle. Through this matrice's eigenvalues, physics fields associated to the photon and the Z^0 boson can be introduced as combinations of the B_μ and W^3_μ bosons :

$$\begin{aligned} Z^0 &= cos(\theta_W)W^3 - sin(\theta_W)B \\ A &= sin(\theta_W)W^3 + cos(\theta_W)B \end{aligned} \tag{1.10}$$

θ_W and the g and g' coupling constants are related through :

$$g\ sin(\theta_W) = g' cos(\theta_W) = e \tag{1.11}$$

where e is defined as the coupling constant of field A associated to the photon with charged fermions : namely the electric charge. Similarly $W^\pm$ are a combination of W^1_μ and W^2_μ bosons :

$$W^\pm = \frac{1}{\sqrt{2}}(W^1 \mp iW^2) \tag{1.12}$$

Photons remain massless because the $U(1)_{EM}$ symmetry is preserved, whereas the weak bosons W and Z acquire a mass by the Higgs mechanism :

$$\begin{aligned} m_W &= \tfrac{1}{2}vg \\ m_Z &= \tfrac{1}{2\ cos\ \theta_W}vg = \tfrac{M_W}{cos\ \theta_W} \end{aligned} \tag{1.13}$$

explaining the electro-weak symmetry breaking.

Yukawa coupling to the top quark

The Lagrangian of the Higgs boson coupling to the top quark is [7] :

$$\begin{aligned} \mathscr{L}_{Yukawa,\,top} &= \lambda_t\ \overline{\psi^{t,b}_L}\ \tilde{\phi}\ \psi^t_R = \lambda_t\ (\overline{t_L}; \overline{b_L})\ \tilde{\phi}\ t_R \\ &= \lambda_t\ (\overline{t_L}; \overline{b_L}) \begin{pmatrix} \frac{v+h}{\sqrt{2}} \\ 0 \end{pmatrix} t_R = \lambda_t\ \overline{t_L}\ \frac{v+h}{\sqrt{2}}\ t_R \\ &= \frac{\lambda_t v}{\sqrt{2}}\overline{t_L}t_R + \frac{\lambda_t}{\sqrt{2}}\overline{t_L}t_R h \end{aligned} \tag{1.14}$$

where λ_t is the Higgs boson to top quark Yukawa coupling, $(\overline{t_L}; \overline{b_L})$ is the left doublet and t_R the right top singulet. This results in two terms. The first one is the top quark mass term $m_{top} = \frac{\lambda_t v}{\sqrt{2}}$. The second term represents a top-top-Higgs vertex with a coupling constant $\frac{\lambda_t}{\sqrt{2}}$.

Equation 1.14 can be written similarly for any quark. The Lagrangian for fermions thus includes a mass term and an interaction term with the Higgs boson proportional to $\frac{m_F}{v}$, which is low for most of the fermions except for the top quark. The mass of fermions is defined as :

$$m_F = \frac{v\lambda_F}{\sqrt{2}} \tag{1.15}$$

where λ_F is the Yukawa coupling for fermions with the Higgs boson. Its value is not determined by theory, but all directly measured or estimated for u, d, s, c, b : the fermions mass are therefore free parameters of the Standard Model.

7. Similar Yukawa terms exist for other fermions

It was also found from equation 1.9 the couplings for vector bosons are proportional to the square of their mass. To summarise, the Yukawa couplings of the Higgs boson to fermions are proportional to the fermion's masses and the coupling of the Higgs boson to other bosons proportional to their squared mass :

$$\begin{cases} \lambda_F = \sqrt{2}\frac{m_F}{v} \\ \\ \lambda_V \propto \frac{m_V^2}{v} \end{cases} \tag{1.16}$$

Figure 6.10a illustrates how well current measurements align with theory.

The top mass being measured at $m_{top} = 173\ GeV$, equation 1.14 results in the Yukawa coupling of the Higgs boson to the top quark to be $\lambda_{top} = \sqrt{2}\frac{m_{top}}{v} = \simeq \sqrt{2}\frac{175\ GeV}{246\ GeV} \simeq 1$. The coupling of the Higgs boson to the top quark is therefore its strongest coupling. Part II of this document is devoted to its measurement.

Experimental Higgs boson production

Experimentally, the Higgs boson can be created at the LHC by four production modes illustrated by Feynman diagrams on figure 1.5 : the gluon fusion (ggF), Vector Boson Fusion (VBF), associated production with a Z/W (V [8]) boson WH and ZH (VH) and associated production with a pair of top-anti-top quarks ($t\bar{t}H$) [9]. These production cross sections as a function of the energy in the centre of mass of the collider is shown on figure 4.1 right. Part I relating the discovery mostly relies on the most abundant gluon fusion mode, while parts II and III focus on the rarest, namely associated production with a pair of top-anti-top quarks for the direct top-Higgs coupling measurement.

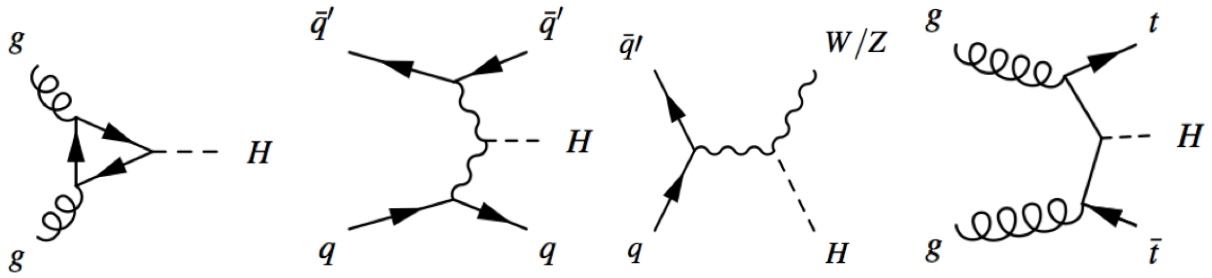

(a) ggF (b) VBF (c) VH (WH, ZH) (d) ttH

FIGURE 1.5 – Higgs production modes : Gluon fusion (ggF), Vector Boson Fusion (VBF), associated production with a Z/W (V) boson WH and ZH (VH) and associated production with a pair of top-anti-top quarks ($t\bar{t}H$)

8. Throughout this text, V refers to production of an electroweak boson (W or Z/γ^*).

9. Other production modes are very rare (e.g. $pp \to tHqb$) or very hard to disentangle from the most prominent ones (e.g. $pp \to b\bar{b}H$)

I

$H \to \gamma\gamma$

2. Standard Model $\gamma\gamma$ measurement and composition

2.1 Photon isolation & identification

Photon reconstruction

In a first step of photon reconstruction, clusters are seeded from energy deposits in the electromagnetic (EM) calorimeter with total transverse energy above 2.5 GeV by using a sliding-window algorithm with a window size of 3×5 in units of 0.025×0.025 in $\eta \times \phi$ (Figure 2.1b). After their reconstruction, clusters are matched to tracks from the inner tracker (Figure 2.1a).

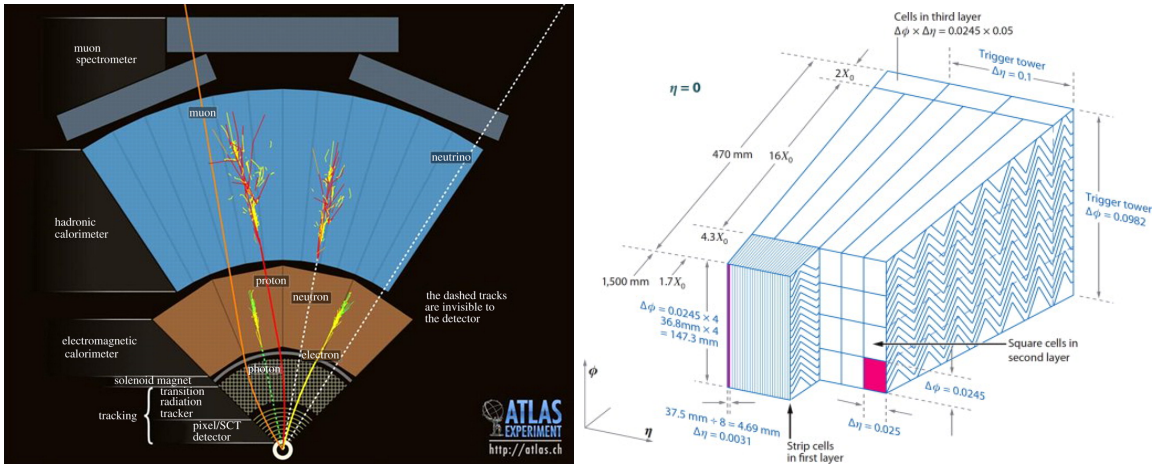

(a) ATLAS detector (b) EM Calo granularity

FIGURE 2.1 – ATLAS sub-detectors and EM calorimeter granularity [21].

Tracks consistent with originating from a photon conversion are used to create conversion vertex candidates. Conversion vertex candidates are matched to seed clusters, and a final algorithm decides whether a seed cluster corresponds to an unconverted photon, a converted photon or a single electron [22]. Clusters without a track are classified as unconverted photons.

The ambiguity between electrons and photons can be partially removed by the fact conversion vertices are triggered by material and therefore happen at a larger radius than prompt electrons. Tracks without hit at low radius are therefore possibly converted photons. To exploit that particularity, prompt electrons are required to present low radius hits in the inner tracker. For each track, the presence of a hit in the first pixel layer during run 1, and the insertable b-layer after

2014, are used in the algorithm as discriminating variable to disentangle electron and converted photon hypotheses. Conversions vertices are also expected to hold two tracks, but very often only one is reconstructed because of an asymmetric conversion into one soft electron/positron and the other one taking away most of the initial transverse energy. Values of the ratio of the energy reconstructed in the calorimeter over the track's momentum measured in the inner tracker E/p, traditionally used to spot electron bremsstrahlung, can also be a hint for such an asymmetric photon conversion. A conversion ambiguity flag using the above information is compiled and used to further reduce the conversions as discussed in section 7.1.

To disentangle photon shower from those produced by hadrons, shower shape information are used in the identification and isolation process described below. Indeed hadronic jets generally produce calorimetric deposits broader and less isolated than electromagnetic showers, with sizeable energy leaking to the hadronic calorimeter.

Photon identification

In the hadronic environment provided by the LHC, a large majority of the reconstructed photons are from hadron decays in processes with much higher cross section than those producing prompt photons. The importance of photon identification (ID) is illustrated on Figure 2.2, showing that a rejection of non-prompt photons of three orders of magnitude per photon is needed to bring γ-jet and jet-jet backgrounds below the prompt $\gamma\gamma$ signal production. With a rejection rate of typically one thousand to five thousands against jets, photon ID is a key element of the di-photon cross section measurement and the search for the Higgs decaying in two photons. This will be discussed in sections 2.3 and 3.1. Non-prompt photons, or so called *fake* photons represent a big part of photon analyses background. They are the contribution to the background arising from hadrons whose deposits in the calorimeter have similar characteristics to those of real photons.

Photon identification is therefore necessary to disentangle photons from jets. It mainly relies on the study of energy distribution of the shower in the calorimeter, through the longitudinal and lateral granularity of the ATLAS EM calorimeter (see Figure 2.1b), which is a subject widely developed in my thesis [1]. Firstly, the transverse shower shape in the second layer of the electromagnetic calorimeter needs to be consistent with that expected for a single electromagnetic shower. The high granularity first layer is used to discriminate single photons from overlapping photon pairs from neutral meson (π^0) decays produced in jet fragmentation, which are the main background source. The photon candidate is also required to deposit only a small fraction of its energy in the hadronic calorimeter. Based on these criteria, a set of identification cuts is applied that are different for converted and unconverted candidates, being in particular looser in ϕ for the former ones due to the opening of electron and positron pairs in the solenoid magnetic field. Depending on the presence and tightness of cuts applied on the above described shower shape variables, one builds two levels of photon identification, *loose* and *tight*, also respectively referred later in this text as L and T.

Photon isolation

Another type of variable, called calorimetric isolation can be build to discriminate jets from photons. Within a cone of size $\Delta R = \sqrt{\Delta\phi^2 + \Delta\eta^2}$ around the object of interest, one defines

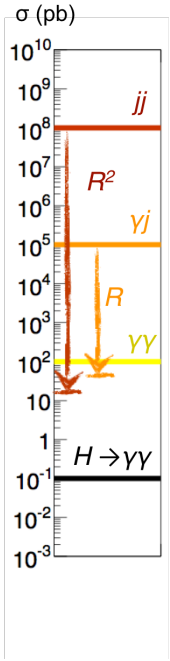

(a)

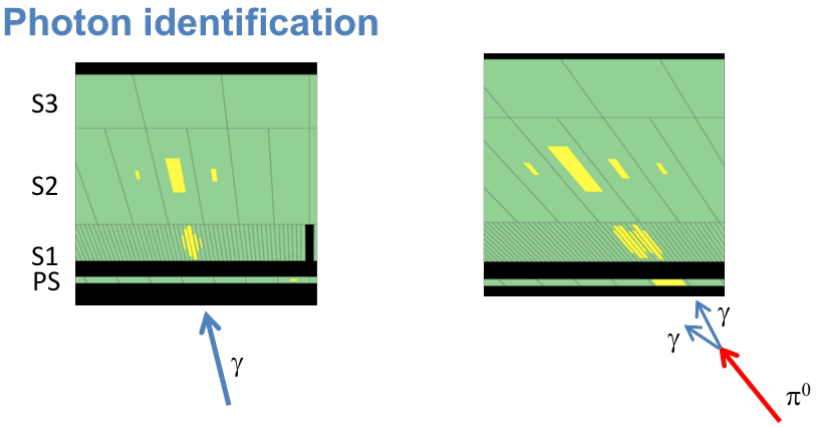

(b) Photon identification

FIGURE 2.2 – Left : comparison of pp→ $\gamma\gamma$, pp→ γ-jet, pp→jet-jet and pp → H → $\gamma\gamma$ production cross sections at the LHC for 8 TeV, and rejection factor R of the photon identification. Right : use of granularity in the first calorimeter sampling for photon identification and neutral pion in jet rejection.

the raw energy

$$E_T^{raw} = \sum_{topo} p_T^{topo}$$

where p_T^{topo} is the transverse momentum of topological clusters. Topological clusters (or *topoclusters*) are built with a *4/2/0* algorithm. The cluster is namely seeded by cells with energy four times above the noise level in that cell, then neighbours with $\mid E \mid$>2×noise are agglomerated, and finally all their neighbouring cells. Corrections are then applied in the following way :

$$E_T^{iso} = E_T^{raw} - E_T^{core} - E_T^{leakage} - E_T^{pile-up} \tag{2.1}$$

where :

- E_T^{core}, is the energy of a rectangular cluster of size 5×7 in the second sampling of the EM calorimeter and roughly assumed to be due to the photon itself, as illustrated on Figure 2.3a.
- $E_T^{leakage}$ is the energy leaking on average from this 5×7 bloc but belonging effectively to the photon core shower. It is an average value parameterised as a function of the transverse momentum p_T and pseudo-rapidity η.
- Finally $E_T^{pile-up} = \rho A$ is the average p_T density ρ multiplied by the area A of the isolation cone : ρ is estimated as being the median of the distribution of the p_T of the jets divided by their area. The area of jets is approximately $\pi \times R^2$ where the radius R is chosen depending on the jet reconstruction algorithm (see explanations below). The area of the cone is corrected by the core area $A = \pi \times R^2 - 5 \times 7 \times 0.025 \times 0.025$.

As seen in equation 2.1, isolation must be corrected from the average contribution of pile-up (see section 1) which is estimated using jets. A jet algorithm is defined by the distance under which two constituents are merged. For a k_T family algorithm, this distance is :

$$min(p_{T,i}^{2p}, p_{T,j}^{2p}) \times \frac{\Delta_{R,ij}^2}{R^2} \tag{2.2}$$

where R is the chosen size parameter, $\Delta_{R,ij}$ the distance between sub-jets (or constituents) i and j, and $p_{T,i}$, $p_{T,i}$ their transverse momentum. If p = 0 : this is the Cambridge-Aachen algorithm where closer objects are merged first regardless of their p_T. p = 1 is the k_T algorithm for which softer constituents are merged first. If p = -1, this is anti-k_T, where harder momentum objects are combined first. For pile-up density determination, a cone of size 0.5 is used with a k_T algorithm, while jets used in the analyses are using anti-k_T and a radius parameter R = 0.4 [23].

Track isolation, sharing the same concept as the calorimetric one, is defined as the sum of p_T of the tracks [1] reconstructed in the inner tracker in a ΔR cone around the direction of the photon. Thanks to the higher granularity of the silicon tracker compared to that of the calorimeter, the track isolation cone size can go below 0.2. A variable cone size track isolation can also be used, although not for photons : $\Delta R = Min(\frac{k_T}{p_T}, R)$ where k_T is a constant fixed at 10 GeV and R is the maximum cone size (from 0.2 to 0.4). In the rest of the document, an isolated photon is labelled *I*. A tightly identified and isolated photon is denominated as *TI*, and when both photons are in the di-photon final states, *TITI*.

1. The tracks associated to conversion vertices are excluded from the sum. Track isolation is also more robust against pile up thanks to the easier association to the chosen primary vertex.

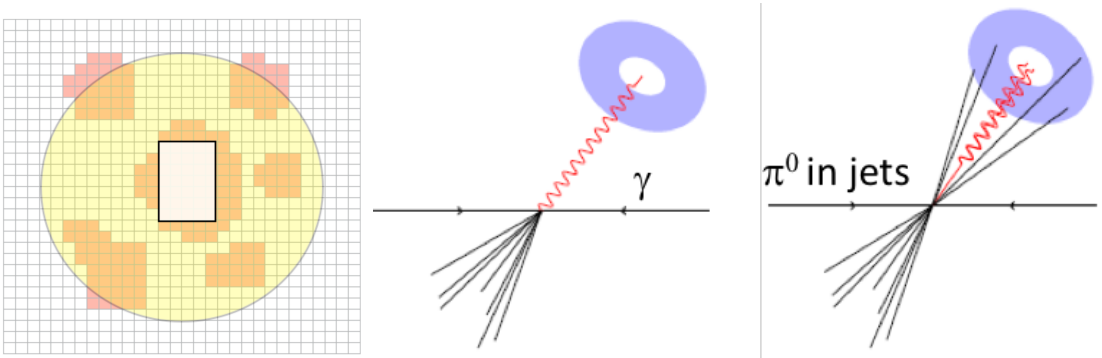

(a) topoclusters (b) photon isolated (c) jet, not isolated

FIGURE 2.3 – Illustration of the isolation reconstruction with topological clusters (left). Sketch of the relative fraction of energy outside the cone for a photon (middle) and for a jet (right).

2.2 Photon efficiency measurement

The main contributions to prompt photons come from non-resonant production of photons in association with jets or of photon pairs, with cross sections respectively of the order of tens of nanobarns or picobarns. The study of such final states, and the measurement of their production cross sections, are of great interest as they probe the perturbative regime of QCD and can provide useful information about the parton distribution functions of the proton. To perform the ATLAS physics program with photons, and in particular the study of the $H \to \gamma\gamma$ process discussed later on, the efficiency of identifying photons must be known at the percent level and on an energy range of a few GeV to several TeV. This precision cannot be achieved by MC only, because of uncertainties arising from limited knowledge of the detector material, from an imperfect description of the shower development and from the detector response. A data-driven estimate is therefore needed and described in this section. The efficiencies are measured for Run 1 data, separately for converted and unconverted photons, in four different pseudo-rapidity regions ($|\eta|<0.6$, $0.6<|\eta|<1.37$, $1.52<|\eta|<1.81$, and $1.81<|\eta|<2.37$), and various transverse momenta between 10 GeV and 1.5 TeV. Since there is not a large data statistics at high p_T, the last bin in p_T is 250 GeV to 1500 GeV.

I participated to the measurement of the photon efficiency measurement by determining a systematic uncertainty for the matrix method [21]. Systematic uncertainties are additional errors to the purely statistical error, considered to take into account any potential bias from the measurement method and instruments that could degrade or modify the central measured value. The matrix method is one of the three data-driven photon ID efficiency measurements. Indeed, in the absence of a single pure control sample of prompt photons over a large range of transverse energy E_T, three different methods measuring the photon identification efficiency in complementary and overlapping E_T regions with varying precision must be combined :

- **The Radiative Z decay Method** selects a clean sample of prompt photons in radiative decays of the Z boson ($Z \to ll\gamma$) in which a photon produced from the final-state radiation of one of the two leptons is selected without imposing any criteria on the photon discriminating variables. Those γ have a relatively low transverse energy, and given the luminosity of data collected in Run 1, the method is only relevant for an E_T range between [10-80] GeV. The main source of uncertainty of this method arises from low statistics.
- **The Electron Extrapolation Method** extrapolates photon properties from a large and pure sample of electrons and positrons from Z boson decays $Z \to e^+e^-$ by exploiting the similarity between the electron and the photon EM showers. The E_T range in which the method can provide precise results follows that of the distribution of electrons from Z boson decays, therefore between [30, 100] GeV at the time, and up to 250 GeV in more recent results. Its main uncertainty is due to the presence of material [2] and the different interaction of photons and electrons in that matter.
- **The Matrix Method** uses the discrimination between prompt and background photons provided by their track isolation to extract the sample purity before and after applying the tight identification requirements. This method provides results for an E_T range of [20 GeV, 1.5 TeV]. Its main source of uncertainty (in 2011) is that of the track isolation efficiency for fake photons failing the tight identification criteria. This document will discuss only this latter method to which I participated.

2. See thesis manuscript [1] where I developed a method to estimate and map material upstream the EM calorimeter.

In the matrix method, photon yield (and purity) before/after photon ID is estimated using track isolation to discriminate between photons and jets faking photons, also called *fakes*, as opposed to prompt photons that do not originate from hadron decays. One needs as an input to this method the track isolation efficiency for photons and for *fakes*. Track isolation was chosen because of its power of discrimination between photons and *fakes*, while being uncorrelated to the tight identification. Similarly to the 2D template fit method and the 2D sideband fit methods developed in section 2.3, the matrix method relies on a discriminating set of cuts that are not correlated to the cut we are trying to determine the efficiency of. The following efficiencies shown on Figure 2.4 are defined as :

- ϵ_p^b (resp. ϵ_f^b, ϵ_{all}^b) is the track isolation efficiency for fake photons passing (resp. failing, failing or passing) tight identification (ϵ_p^b are represented as black triangles on figure 2.4 right. Black triangles on figure 2.4 left are ϵ_{all}^b). It is estimated from a data sample enriched in fake photons by reversing a few cuts on shower shape variables. Di-jet samples are used to derive systematic uncertainties on those efficiencies.
- ϵ_p^s (resp. ϵ_f^s, ϵ_{all}^s) is the track isolation efficiency for prompt photons passing (resp. failing, failing or passing) tight identification (ϵ_p^s are represented as green dots on figure 2.4 right. Green dots on figure 2.4 left are ϵ_{all}^s). It is estimated from prompt photon Monte Carlo (MC) . The systematic uncertainty is the average difference between track isolation efficiencies in data and Monte Carlo for probe electrons from $Z \to e^+e^-$ events, which is the part I was responsible for.
- $\epsilon_p = \frac{N_{pass}^{Iso}}{N_{pass}^T}$ is the fraction of tight photon candidates that pass the track isolation criteria (blue squares on figure 2.4 right).
- $\epsilon_{all} = \frac{N_{all}^{Iso}}{N_{all}^T}$ is the fraction of photon candidates in the inclusive data sample (blue squares on figure 2.4 left).

The resolution of the matrix equations detailed in [21, 24] provides an expression of the efficiency of the tight identification cut :

$$\epsilon^{tight-ID} = \frac{\frac{\epsilon_p - \epsilon_p^b}{\epsilon_p^s - \epsilon_p^b} \times N_{pass}^T}{\frac{\epsilon_{all} - \epsilon_{all}^b}{\epsilon_{all}^s - \epsilon_{all}^b} \times N_{all}^T} \tag{2.3}$$

The result of the photon ID efficiency with the matrix method as well as the electron extrapolation and the radiative decays are provided in Figure 2.5. All three methods are in good agreement.

The results from the combination of these three data-driven techniques are then compared to the predictions from a simulation of the detector response. Data-to-simulation efficiency ratios, also called *Scale Factors* (SF) in ATLAS, are used as correction factors in physics measurements and determined to account for the small residual in efficiency differences. The scale factors for photon efficiencies are obtained by combining results from the three, radiactive Z decay, electron extrapolation and matrix methods assuming uncorrelated systematic uncertainties. These factors are measured with uncertainties between 0.5% and 10% in 7 TeV data and between 0.5% and 5.6% in 8 TeV data, depending on the photon transverse momentum and pseudo-rapidity, as illustrated on Figure 2.6.

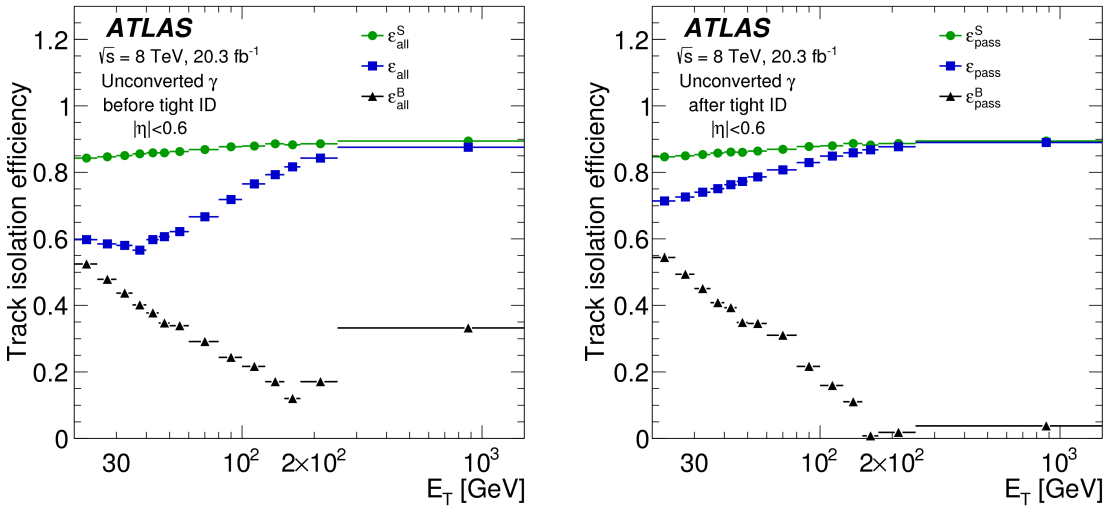

FIGURE 2.4 – Track isolation efficiencies as a function of transverse energy for prompt (green circles) and background (black triangles) unconverted photon candidates within $|\eta|<0.6$ in the inclusive sample (left) or passing tight identification requirements (right). Blue squares show the track isolation efficiency for all candidates selected in data [21].

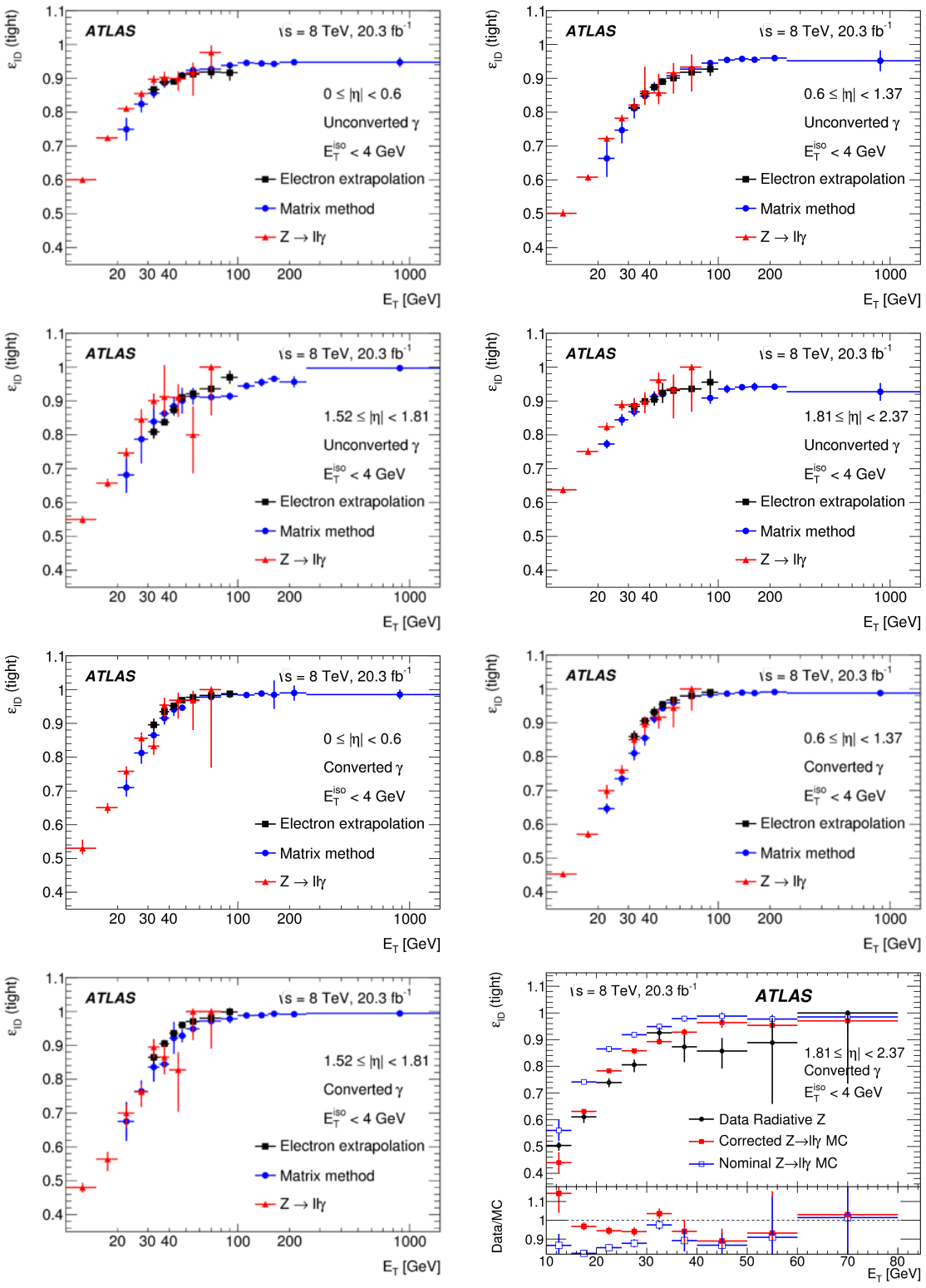

FIGURE 2.5 – Result of the efficiency measurement and comparison of the three methods : matrix method (blue), electron extrapolation (black) and radiative Z decay (red) [21].

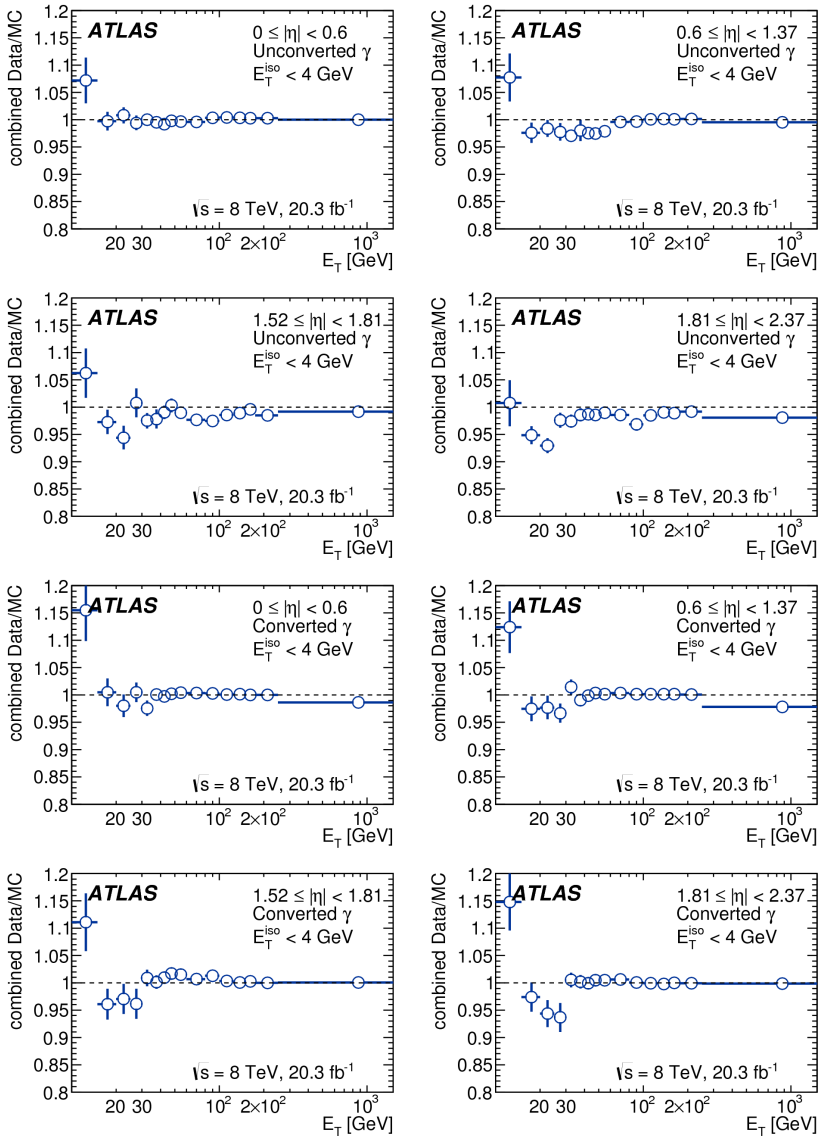

FIGURE 2.6 – Data-to-simulation efficiency ratios (Scale Factors) determined with 20 fb^{-1} of 8 TeV data. Combination of the three sets of scale factors from the radiative Z decay, electron extrapolation and matrix methods [21].

2.3 $\gamma\gamma$ differential cross-section

2.3.1 Motivations

The production of di-photon final states in proton-proton collisions may occur through quark-antiquark t-channel annihilation, $q\bar{q} \rightarrow \gamma\gamma$ also called born diagram, or via gluon-gluon interactions, gg$\rightarrow \gamma\gamma$, mediated by a quark box diagram, as illustrated for leading order processes on figures 2.7a and 2.7b. Despite the higher order of the latter, the two contributions are comparable, due to the large gluon flux at the LHC. First order radiative corrections include real initial state radiation of both born ($q\bar{q} \rightarrow g\gamma\gamma$) and box (qg$\rightarrow$q$\gamma\gamma$) diagrams, respectively Figures 2.7c and 2.7d, as well as virtual corrections as illustrated on figure 2.7e. Radiative corrections from final state radiation can behave in two ways. If the radiated photon is well resolved from the radiating quark, the process is called brem and illustrated on figure 2.7f. If the photon remains collinear to the quark and is taking most of the energy, the process is called fragmentation and symbolised by the blue disk on figure 2.7g. The two configurations are a physical continuum that can be disentangled instrumentally thanks to an isolation requirement. Brem process where the photon is isolated is therefore considered as signal. On the contrary non isolated photons from fragmentation are considered as background.

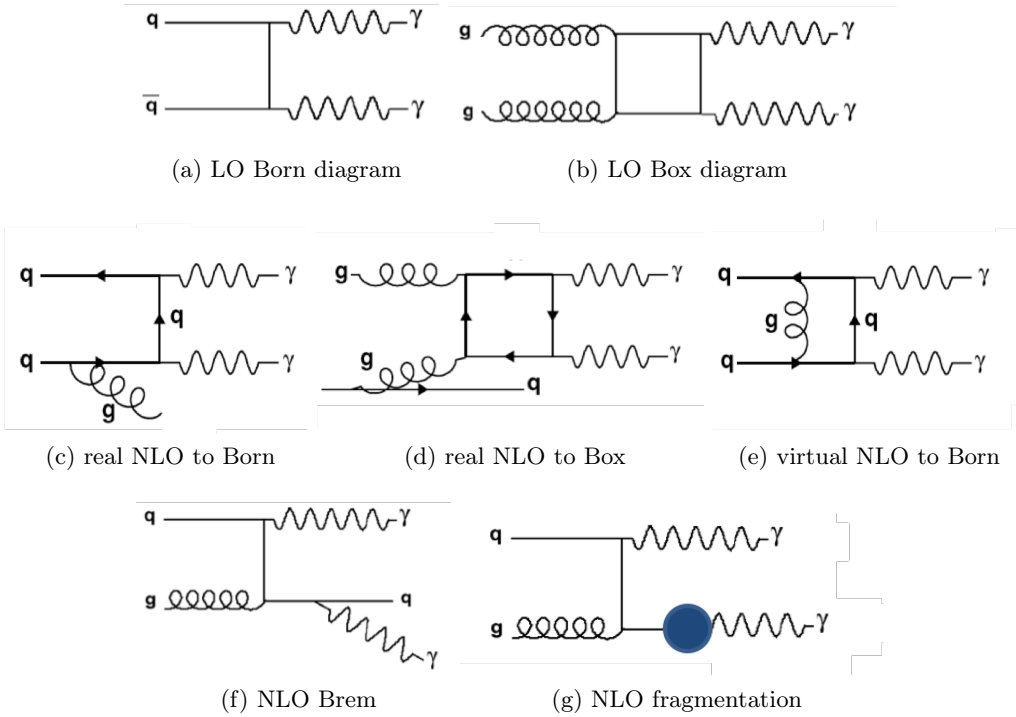

(a) LO Born diagram (b) LO Box diagram

(c) real NLO to Born (d) real NLO to Box (e) virtual NLO to Born

(f) NLO Brem (g) NLO fragmentation

FIGURE 2.7 – Leading (top) and next-to-leading order (middle and bottom) prompt di-photon production modes at the LHC.

This cross-section measurement is a test of Quantum Chromo Dynamics (QCD) [3], more specifically in precise kinematic regions. For instance the low $\Delta\phi_{\gamma\gamma}$ is sensitive to simple and

3. QCD is the quantum field theory with symmetry group SU(3) responsible for strong interactions involving quarks and gluons through the QCD analog of electric charge called color.

double fragmentation processes, whereas $\Delta\phi_{\gamma\gamma}$ close to π and small $p_{T,\gamma\gamma}$ is sensitive to soft gluon emission whose description at fixed order by perturbative QCD computation is not yet accurate. This process is also the background to the searches for di-photon resonances, predicted by some exotic beyond the standard model theories, like for instance the Randall-Sundrum type of extra-dimension models, predicting the existence of massive graviton-like particles. Finally, di-photon is the irreducible background to the search of the Higgs boson decaying in two photons discussed in section 3.1.

The di-photon cross-section measurement exploits differences between the isolation distribution of photons and jets. It uses data-driven methods to estimate backgrounds from hadronic jets and from isolated electrons which are then subtracted. After introducing the data and Monte Carlo used for the analysis in section 2.3.2, section 2.3.3 describes how E_T^{iso} distributions for background and signal are measured from data. Section 2.3.4 details the data-driven methods used to estimate and subtract the γ-jet and jet-jet backgrounds. It focuses particularly on the 2D Fit method to which I participated. Finally, results and interpretation of features of interest with respect to physics processes at work are given in section 2.3.5.

This analysis to which I participated is described with more details in a publication [25] and has been since then updated [26].

2.3.2 Selection and Monte Carlo

The analysis is performed on 37 pb^{-1} of 7 TeV data recorded in 2010. Selected collision data events are required to pass kinematic cuts, also called fiducial acceptance, and isolation cuts, as follows :

- $E_T^{\gamma 1,2} > E_T^{cut} = 16$ GeV
- $|\eta^\gamma| < 1.37$ or $|\eta^\gamma| \in [1.52; 2.47]$ [4].
- The separation between the photons must be $\Delta R > 0.4$.
- The isolation (see 2.1), that is the transverse energy flow of particles within a cone of 0.4 must respect $E_T^{iso} < 3$ GeV for each photon.

The precise location along the beam axis of the primary vertex for di-photon events is determined thanks to an algorithm called photon pointing relying on information from the EM calorimeter first two longitudinal layers. It is obtained by combining the trajectories of each photon, measured using the longitudinal segmentation of the calorimeter and hits in the silicon detector if the photon is converted, with a constraint from the average beam spot position. In most recent versions of this analysis, the best primary vertex is chosen with a Neural Network algorithm (see section 5.2.2) which combines the photon pointing with information on all tracks momenta from the vertex. This procedure provides in particular more accurate invariant mass values, so that the resolution of the di-photon mass reconstructed using this vertex determination is dominated by the photon energy resolution.

Once tightly identified, the selected statistics of *TITI* events where both photons are tightly identified (T) and isolated (I) consists of 2022 candidate events.

The di-photon cross-section measurement is mostly based on data-driven techniques, but for some corrections, systematics or cross checks, a Monte Carlo is used. For these cases, the

4. The EM calorimeter barrel-end-cap transition, also called *crack* ($1.37 < |\eta| < 1.52$), is an instrumentally depleted area in which reconstructed electromagnetic objects are traditionally removed from analyses. This requirement is particularly useful for photons and precision measurements with electron, but if higher statistics is needed electrons reconstructed in the crack can be kept when other objects are present in the event.

characteristics of signal and background photons events are simulated with Pythia 6 [7]. Interaction with the detector being simulated by Geant4 [10], as in all the analyses described in this document. An alternative generator, Sherpa [5] is used to determine signal generator model systematic uncertainties. Monte Carlos with distorted geometries, meaning with different amounts and repartition of the material upstream the calorimeter are used for systematics related to the material estimate uncertainty. More information can be found in my thesis memoire where I describe a material mapping method [1].

2.3.3 Isolation distributions for jets and photons

To perform the 2D fit described in section 2.3.4, the distribution of isolation (relaxed from its final selection cuts) needs to be determined for both jets and photons. The procedure illustrated on MC events on Figure 2.8 is the following :

(a) The E_T^{iso} template for background is obtained from a control sample having failed the *tight* identification and called *Non-Tight* (NT) events. Figure 2.8, top frame show with Monte Carlo simulations that *Non-Tight* distribution (in dashed red) follows closely that of the background (black) selected from truth information of the MC sample.

(b) The *Tight* control sample contains a mixture of signal (true photons) and background (hadrons faking photons). However, as shown on Figure 2.8 middle frame, almost all *Tight* events with E_T^{iso}>7 GeV are backgrounds. The *Non-Tight* distribution normalised in the E_T^{iso}>7 GeV region (blue area), is considered as the background component of the *Tight* sample and is subtracted to the inclusive *Tight* distribution.

(c) The result of that subtraction (in dashed red line) is the E_T^{iso} distribution of a pure photon signal, as illustrated when compared to the MC truth (in black) on Figure 2.8 lower frame.

This procedure is then performed on data separately for the leading and sub-leading photons (ordered by p_T), to obtain a completely data-driven E_T^{iso} distribution of the transverse isolation energy of photons as shown on Figure 2.8 right. The main source of systematics in this method comes from the choice of the *Tight* set of identification cuts. There is also a slight effect of changing the E_T^{iso} normalisation cut value from 7 to 6 and 8 GeV. Several quantities have been varied to successfully demonstrate the robustness of the method on MC : signal leakage into the *Non-Tight* sample, correlations between the E_T^{iso} and the reversed identification cuts, different signal composition in term of relative fraction of photons produced by the hard scattering or by the fragmentation process, and different background composition in term of relative fraction of photon pairs from π^0 decays compared to other hadrons.

The E_T^{iso} distributions were also independently determined from pure electron samples from $Z \to e^+e^-$ and $W \to e^\pm\nu$ events. The difference between the E_T^{iso} distributions for electrons and photons are mainly that electrons have wider bulk of the distribution due to their bremsstrahlung in the material upstream the calorimeter [1], and photons longer tails due to photon fragmentation, especially for sub-leading photons. The electron/photon difference is fitted from Monte Carlo simulations and propagated to the electron based data-driven estimate. The result, which is the blue line on Figure 2.8 right, agrees nicely with the photon derived shape.

Isolation transverse energy E_T^{iso} distribution are then smoothed. Correlation between the isolation of the leading and subleading photon in signal and background events was investigated with a Tag and Probe method, namely studying the E_T^{iso} distributions of a candidate (*Probe*) under different isolation conditions of the other candidate (*Tag*). The result showed little to none correlation for $\gamma\gamma$ signal events, but a clear positive correlation for background events where the

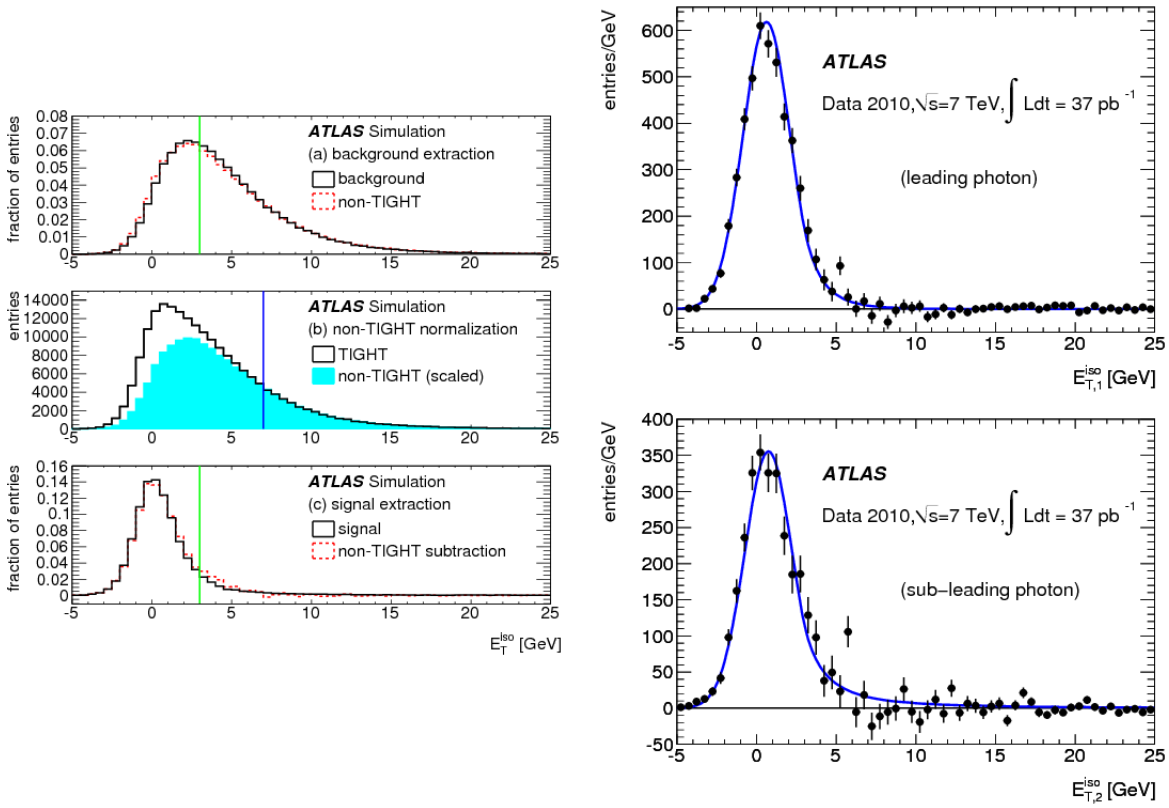

FIGURE 2.8 – Left : Determination of the background and signal isolation E_T^{iso} distributions (aka *templates*). Right : Data-driven E_T^{iso} distributions of the leading (top) and subleading (bottom) photon using photon candidates (solid circles) or extrapolated from electrons (continuous lines) [25].

Probe is more (resp. less) isolated if the *Tag* passes (resp. fails) the isolation criterion. This effect being particularly true for jet-jet events. As a result, while 2D E_T^{iso} distributions for $\gamma\gamma$, γ-jet and jetγ events are the products of one-dimensional PDFs (Probability Density Function), that is respectively 1D $f_{\gamma 1}\times$ 1D $f_{\gamma 2}$, 1D $f_{\gamma 1}\times$ 1D f_{j2}, and 1D $f_{j1}\times$ 1D $f_{\gamma 2}$, the E_T^{iso} distributions for jet-jet events is a 2D f_{jj} distribution taken directly from data with both photon candidates failing the *Tight* identification requirement. Index 1 (resp. 2) stands for the leading (resp. subleading) jet or photon. This is expressed in Equation 2.4.

2.3.4 Background subtraction with the 2D fit

Three different methods were performed and compared for the γ-jet and jet-jet estimate and subtraction. All three rely on the photon vs jet discriminating power of the isolation transverse energy E_T^{iso}, and the absence of correlation of that isolation information with respect to the tight T set of identification variables. Their purpose is to sort events from the signal region (where both objects are *Tight Isolated Tight Isolated* or *TITI*) into four different categories : $N_{\gamma\gamma}^{TITI}$, $N_{\gamma jet}^{TITI}$, $N_{jet\gamma}^{TITI}$ [5] and N_{jetjet}^{TITI}.

- The event weighing, or **matrix method**, consists in an inversion of the matrix of weights giving the probability that a given final state passes or fails isolation. It has the advantage of providing an event-by-event weight.
- The **two-dimensional fit**, or **2D fit** method. Two-dimensional distributions [6] of $\gamma\gamma$, γ-jet, jet-γ and jet-jet events are built. The four yields in the TT sample come from an extended maximum likelihood fit using the isolation templates. This is the method I participated to and that is developed below. Its 2D label, also used for the 2D sideband described below, refers to use of two orthogonal sets of discriminating variables, the identification and the isolation (see section 2.1).
- The isolation vs identification sideband counting, or **2D sideband method** sorts events into A('), B('), C(') and D(') regions depending on whether the (sub-)leading photon candidates passes the identification and isolation requirements. The two dimensions also here refer to isolation and identification. It then determines the number of events in the signal region A with a rule of three assuming the fraction of tightly identified objects passing the isolation is the same as that of non-tight identified objects passing isolation, or in other words relying on identification cuts being uncorrelated to the isolation cuts.

The three methods cannot be combined because they are using the same quantities, E_T^{iso} and identification shower shapes with the use of the *Non-Tight* control regions. They provide comparable results and systematics uncertainties, as shown on Figure 2.10.

In the 2D fit method, the four yields in the TT sample come from an extended maximum likelihood fit of the following model to the data 2D distribution :

$$\begin{aligned} N^{TT} f^{obs}(E_{T,1}^{iso}, E_{T,2}^{iso}) = & N_{\gamma\gamma}^{TT} f_{\gamma 1}(E_{T,1}^{iso}) f_{\gamma 2}(E_{T,2}^{iso}) \\ & + N_{\gamma j}^{TT} f_{\gamma 1}(E_{T,1}^{iso}) f_{j2}(E_{T,2}^{iso}) \\ & + N_{j\gamma}^{TT} f_{j1}(E_{T,1}^{iso}) f_{\gamma 2}(E_{T,2}^{iso}) \\ & + N_{jj}^{TT} f_{jj}(E_{T,1}^{iso}, E_{T,2}^{iso}) \end{aligned} \tag{2.4}$$

5. The γ-jet and jetγ categories, depending on whether respectively the photon or the jet has higher E_T, are distinct because of the methods technical aspects but are often merged for physics considerations

6. Also called *template* which explains the historical name of *Template Fit Method*

where the unknowns to be determined are the normalisations $N^{TT}_{\gamma\gamma}$, $N^{TT}_{\gamma j}$, $N^{TT}_{j\gamma}$ and N^{TT}_{jj}, namely the number of events where both objects pass the tight identification (TT) for the four $\gamma\gamma$, γ-jet, jetγ and jet-jet categories. The isolation PDFs where determined in section 2.3.3, and the 2D shape and normalisation of TT events f^{obs} and N^{TT} are measured from data in the TT region. Figure 2.9 illustrates this two-dimensional fit by projections on the leading (left) and subleading (right) photon candidate total pdf. In order to obtain the $\gamma\gamma$ yields in the $TITI$ region, $N^{TT}_{\gamma\gamma}$

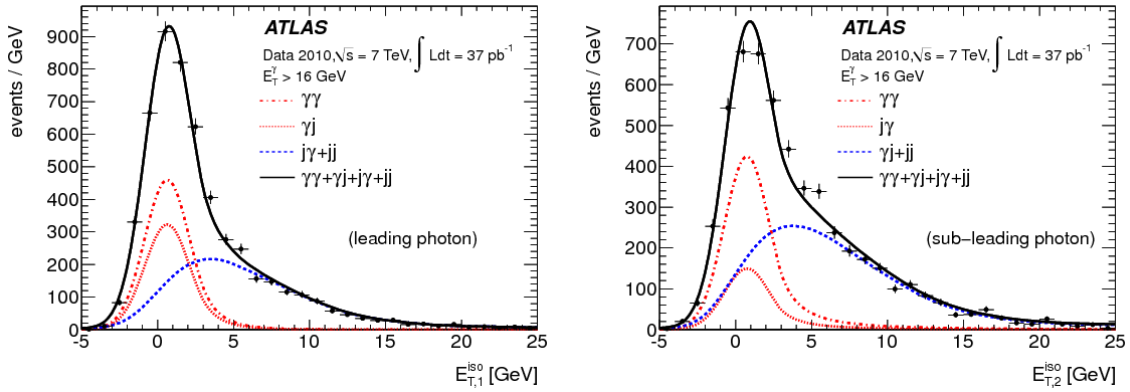

FIGURE 2.9 – Projection of the 2-Dimensional PDF fit on the transverse isolation energies of the two photon candidates : leading (subleading) photon on the left (right). Solid circles represent the observed data. The continuous curve is the fit result, while the dashed-dotted curve shows the $\gamma\gamma$ component. The continuous red and blue dashed line represent respectively the jetγ and γjet+jetjet background components [25].

is multiplied by the integral of the 2-dimensional signal PDF $f_{\gamma 1}(E^{iso}_{T,1})f_{\gamma 2}(E^{iso}_{T,2})$ over the region where $E^{iso}_{T,1}$ <3 GeV and $E^{iso}_{T,2}$ <3 GeV. That procedure is done in each bin of the $m_{\gamma\gamma}$, $\Delta\phi_{\gamma\gamma}$ and $p_{T,\gamma\gamma}$ distributions. The results is shown on Figure 2.10 in blue triangles and compared to the other two method results. My main contribution to that work has been the estimate of this method's systematic uncertainties that are :

(i) Definition of the *Non-Tight* control sample $(^{+13\%}_{-0\%})$ which effect is measured by changing the number of reversed identification cuts.

(ii) Signal composition ±8% which impact is conservatively assessed by setting artificially the fraction of fragmentation photons to 0% or 100% (as photons from fragmentation induce longer tails in the transverse isolation energy especially for the sub-leading photon).

(iii) Effects of the material knowledge on the signal $(^{+1.6\%}_{-0\%})$ which has been quantified by reproducing the electron to photon extrapolation described in section 2.3.3 in Monte Carlos with a distorted geometry [1].

(iv) Signal ±0.7% and jets ±1.2% PDF parameters, estimated by randomly varying the parameters of the smoothing functions within their covariance ellipsoïd and then repeating the two-dimensional fit.

(v) Di-jet PDF parameters ±1% determined by randomly extracting a non negligible amount of points from the smoothed f_{jj} PDF and then re-smoothing to repeat the 2D fit.

(vi) Signal contamination in the *Non-Tight* sample $(^{+1.2\%}_{-0\%})$ estimated by taking the signal contamination from simulation that was neglected to compute the central value.

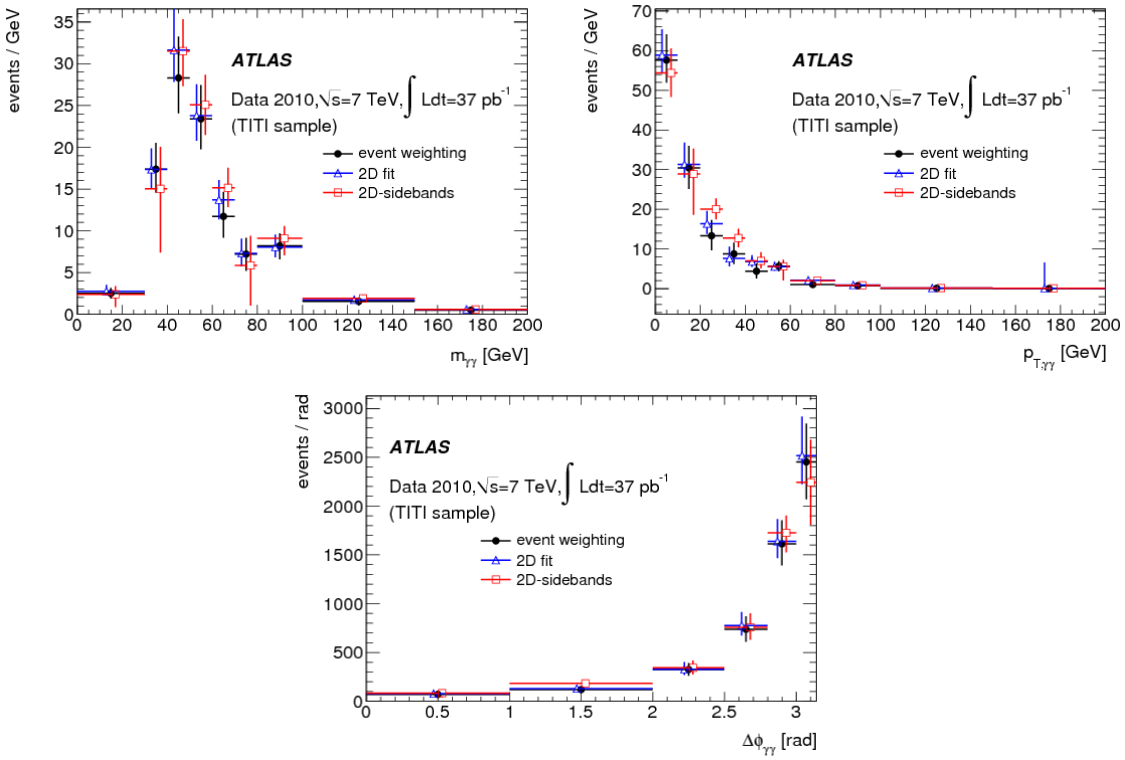

FIGURE 2.10 – Comparison of the three methods : matrix method (event weight), 2D sideband fit and 2D template fit for γ-jet and jet-jet background subtraction for the invariant mass $m_{\gamma\gamma}$, the separation in azimuthal angle $\Delta\phi_{\gamma\gamma}$ and the transverse momentum $p_{T,\gamma\gamma}$ distributions [25].

The electron to photon fake rate is estimated with $Z \to e^+e^-$data events where the number of electrons falsely identified as photons is measured : $f_{e\to\gamma} = 0.112 \pm 0.005$ (stat) $\pm$ 0.003 (syst), and the electron background is estimated in each bin of the variables and accordingly subtracted. The fractional contamination, amounting to $\simeq 5\%$, shows a peak around $m_{\gamma\gamma} \simeq 90$ GeV [7] but is rather uniformly distributed as a function of $\Delta\phi_{\gamma\gamma}$ and $p_{T,\gamma\gamma}$.

2.3.5 $\gamma\gamma$ differential cross-section results and interpretation

The differential cross-sections $\frac{d\sigma_{\gamma\gamma}}{dX}$ for observable X, where X is either the invariant mass of the two photons $m_{\gamma\gamma}$, their separation in azimuthal angle $\Delta\phi_{\gamma\gamma}$ or their transverse momentum $p_{T,\gamma\gamma}$, is given by :

$$\frac{d\sigma_{\gamma\gamma}}{dX} = \frac{N_{\gamma\gamma}}{\epsilon^{RA} \times \epsilon^{trigger} \times \epsilon^{ID} \times \mathcal{L} \times \Delta X} \tag{2.5}$$

where :

- $N_{\gamma\gamma}$ is the number of signal events, determined after γ-jet and jet-jet backgrounds subtraction $N_{\gamma\gamma} = N_{tot,measured} - N_{\gamma-jet} - N_{jet-jet}$, as described in section 2.3.
- ϵ^{RA} accounts for both the reconstruction efficiency and the acceptance of the kinematics and isolation cuts described in section 2.3.2 that go beyond the fiducial acceptance. It amounts to 50% to 60% mainly due to the EM calorimeter readout failures [8] (-18%) and the calorimetric isolation cut (-20%).
- $\epsilon^{trigger}$ the trigger efficiency is computed with respect to the *TITI* identification for an overall value of $98\pm \simeq 2\%$. It is measured from data with three possible methods : bootstrap, tag-and-probe, or electron-to-photon extrapolation.
- ϵ^{ID} the efficiency of applying the TT identification to both photons is here determined in bins of p_T and η on MC where shower shape and isolation distributions are corrected to take into account the data/MC difference. Indeed this di-photon cross-section measurement preceeds the data-driven photon efficiency measurement that was described in section 2.2. The di-photon event efficiency is flat at approximately 60% for $\Delta\phi_{\gamma\gamma}$ and increases with $m_{\gamma\gamma}$ and $p_{T,\gamma\gamma}$ from 55 to 80% with a total systematic error of $\simeq$10% uniform on the three variables considered.
- $\mathcal{L} = \int \mathscr{L} dt$ the integrated luminosity, 37 pb^{-1} of 7 TeV data for this analysis
- ΔX the observable bin width

The unfolding is the determination of the real differential spectrum from the reconstructed one. The treatment of migration of events from one bin of the distribution to its neighbours is performed with an inversion of the migration matrix determined with Pythia MC events, and its systematic uncertainty probed with a large number of toys are found to be negligible.

Figures 2.11 and 2.12 show the result obtained for $m_{\gamma\gamma}$, $\Delta\phi_{\gamma\gamma}$ and $p_{T,\gamma\gamma}$ distributions. In order to interprete results two processes are of particular interest :

7. A peak around m_Z is expected, and can be slightly different given the $e \to \gamma$ candidate is calibrated as a photon instead of an electron.

8. Failures of the optical transmitters (OTx) for front-end of the liquid argon calorimeter electronics readout occurred periodically from 2007 until 2010, up to the rate of one a week. The loss of each optical link meant loosing an entire front end board (FEB), that is 128 channels out of a total of 175000. VCSEL semiconductor laser diode were identified as defective. A replacement was made during the 2010-2011 shutdown and no failure were reported since.

- ⇝ Quark to photon fragmentation is the process $q \to q\gamma$ where the outgoing quark energy is so small that resulting hadrons are trailing and not reconstructed in the detector.
- ⇝ Next-to-Leading-Log (NLL) re-summation, which is the re-summation of divergences arising at low $p_{T,\gamma\gamma}$ due to initial-state soft gluon emission

In the 7 TeV analysis I participated to, the cross-section experimental measurement is compared to two generators : ResBos [27] and Diphox [28]. Both ResBos and Diphox, have Next-to-Leading-Order (NLO) corrections. Only ResBos has the Next-to-Leading-Log re-summation. DiPhox has NLO 1 and 2-photon fragmentation but ResBos only includes LO 1-photon fragmentation. $m_{\gamma\gamma}$ and $p_{T,\gamma\gamma}$ differential cross-section distributions are overall similar for predictions and measurements. A disagreement is observed in the low invariant mass region where $m_{\gamma\gamma} < 2 \times E_T^{cut}$ (16 GeV per photon). As this region is populated by events with small $\Delta\phi_{\gamma\gamma}$ (see equation 2.6), the poor quality of the predictions can be related to the discrepancy observed in the $\Delta\phi_{\gamma\gamma}$ distribution.

$$\begin{aligned} m_{\gamma\gamma} &= \sqrt{2E_{T,1}E_{T,2}(cosh(\eta_1 - \eta_2) - cos(\phi_1 - \phi_2))} \\ &= \sqrt{2E_{T,1}E_{T,2}(cosh(\Delta\eta_{\gamma\gamma}) - cos(\Delta\phi_{\gamma\gamma}))} \end{aligned} \tag{2.6}$$

Results show that the $\Delta\phi_{\gamma\gamma}$ distribution is broader in data than in predictions. The underestimation of the cross-section at small azimuthal separation from prediction versus experimental result, which was also seen in CMS and TeVatron results, can be fixed by using higher order simulation (Next-to-Next-to-Leading Order NNLO). Indeed, for both photons not to be back-to-back, the $\gamma\gamma$ system must recoil to a third object. An initial state radiation (ISR) jet must be present, only described at higher orders of predictions.

The results and conclusions are compatible with those previously obtained at the TeVatron by CDF [29] and D0 [30] experiments, as illustrated on Figure 2.13 and at CMS [31].

This analysis to which I participated is described with more details in a publication [25] and has been since then updated [26]. A more recent implementation of Sherpa, its version 2.2.1 [6] where $\gamma\gamma$ and $\gamma\gamma$+1 parton processes are generated at NLO accuracy, and $\gamma\gamma$+2 or 3 partons processes are generated at LO, provides better agreement.

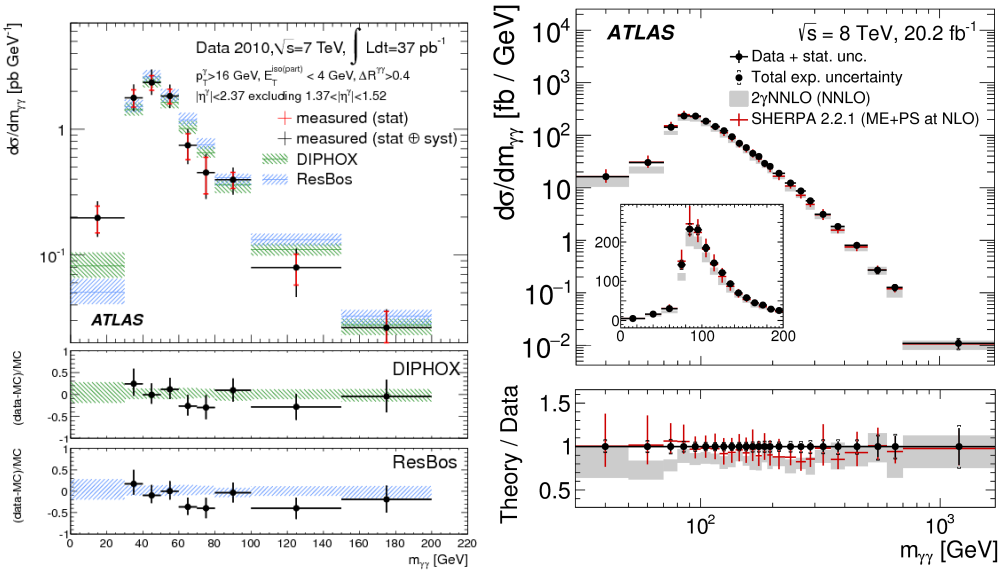

(a) $m_{\gamma\gamma}$@7 TeV (b) $m_{\gamma\gamma}$@8 TeV

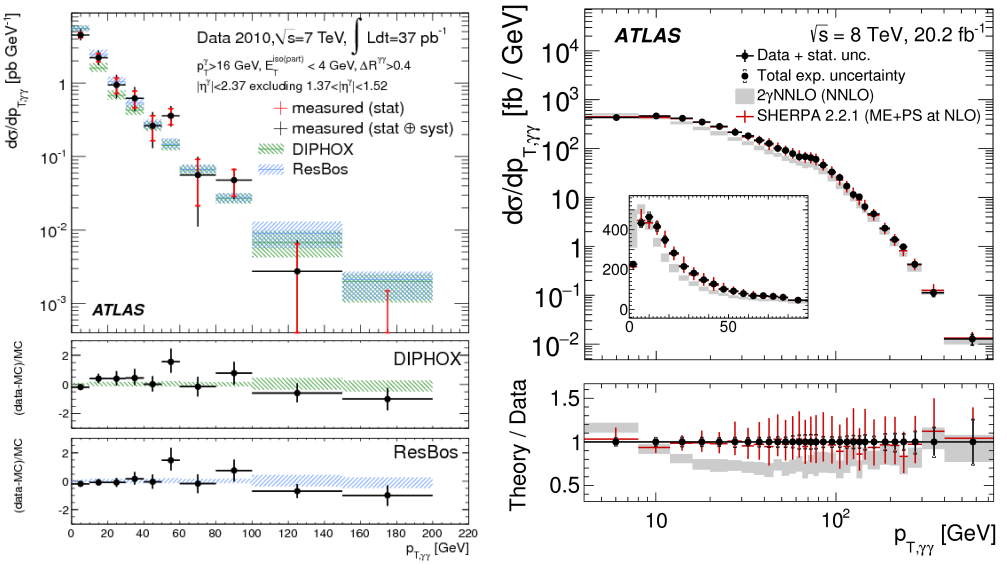

(c) $p_{T,\gamma\gamma}$ @7 TeV (d) $p_{T,\gamma\gamma}$@8 TeV

FIGURE 2.11 – Measured differential cross-sections with 37 pb^{-1} of 7 TeV data [25], and updated analysis with 20.2 fb^{-1} of 8 TeV [26].

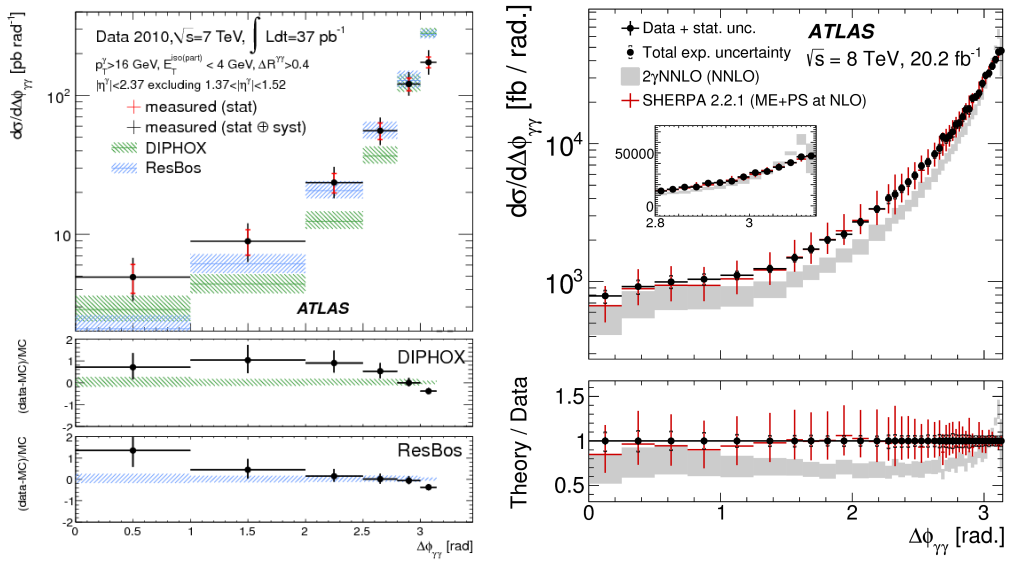

(a) $\Delta\phi_{\gamma\gamma}$@7 TeV (b) $\Delta\phi_{\gamma\gamma}$@8 TeV

FIGURE 2.12 – Measured differential cross-sections with 37 pb^{-1} of 7 TeV data [25], and updated analysis with 20.2 fb^{-1} of 8 TeV [26].

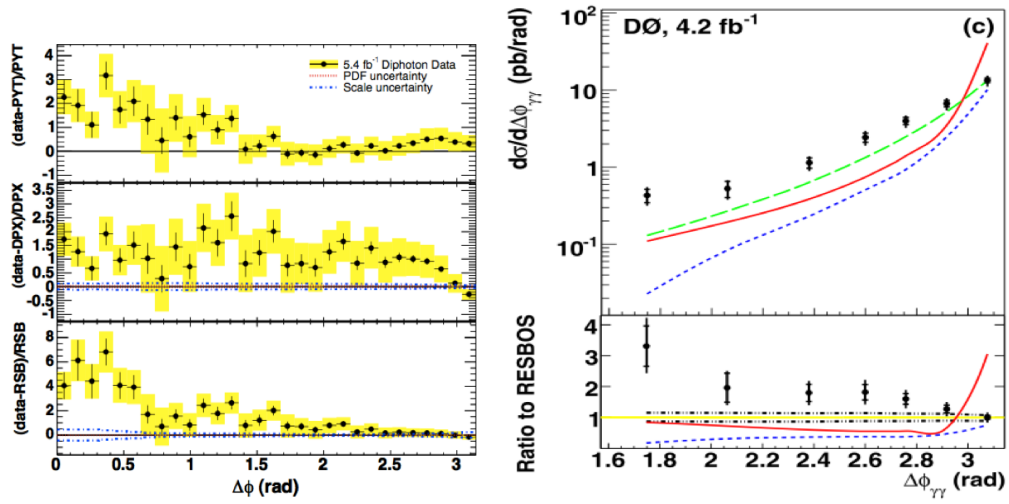

(a) $\Delta\phi_{\gamma\gamma}$@CDF, TeVatron (b) $\Delta\phi_{\gamma\gamma}$@D0, TeVatron

FIGURE 2.13 – Measured differential cross-sections from TeVatron at CDF [29] and D0 [30].

3. Higgs boson discovery and characterisation

3.1 Higgs boson discovery

Ever since ATLAS was built and its innovative accordion calorimeter designed, the search for the Higgs boson decaying in two photons had been prepared for. Indeed, despite a low branching ratio (BR) [1] of $BR_{H\to\gamma\gamma} = 0.2\%$ at 125 GeV, the excellent resolution of the ATLAS EM calorimeter allows for a clear mass peak to be reconstructed, which is also the case for the $H \to ZZ \to 4\ell$. The dominant decay modes at this mass, $H \to WW$ and $H \to b\bar{b}$, suffer respectively from either missing transverse energy due to the presence of neutrinos and a poorer hadron resolution. Hence $H \to \gamma\gamma$ and $H \to 4\ell$ channels have long been known to be golden channels for the Higgs boson discovery, with an additional edge from $H \to 4\ell$ which despite its very low cross section times branching ratio suffers from almost no background.

For the Higgs to be decaying in a photon pair, since the Higgs boson does not couple to photons, processes include W boson or top quark loops as illustrated on figure 3.1. I participated to the $H \to \gamma\gamma$ analysis from 2011 to 2013, where the analysis was repeatedly performed on various sizes of datasets, and internal documentation updated accordingly : 1.08 fb^{-1} [32], 3.43 fb^{-1} [33], 4.8 fb^{-1} [34, 35, 36] of 7 TeV data, and 4.8 fb^{-1} [37] of 8 TeV data. This also corresponds to the period of time over which the "bump" has developed and become significant enough to be claimed a discovery. The results I chose to report in this document are the ones corresponding to the ATLAS public conference note for which I was editor [38], that included 4.8 fb^{-1} of 7 TeV data, and 13.0 fb^{-1} of 8 TeV data. The $H \to \gamma\gamma$ analysis has since been updated many times and its most recent improvements will not be reported here. Its latest developments however include search for deviations in differential measurements split in corners of the phase space which is a subject developed in section 6.1.4 of this document.

3.1.1 Selection

The data sample is collected thanks to an asymmetric diphoton trigger requiring E_T of 35 (25) GeV for the (sub)leading [2] photon, while the final offline selection is chosen to be a 40 and 30 GeV threshold. The fiducial region (η cuts) is the same as for the diphoton cross section measurement. Identification, isolation criteria and primary vertex choice are also applied as explained in 2.3.2. A total of 77430 8 TeV collisions were selected with a diphoton invariant mass between 100 GeV and 160 GeV. Events are split into twelve categories depending on whether :

1. Probability for the particle to decay in a specific final state out of all possibilities.
2. Leading as of highest E_T

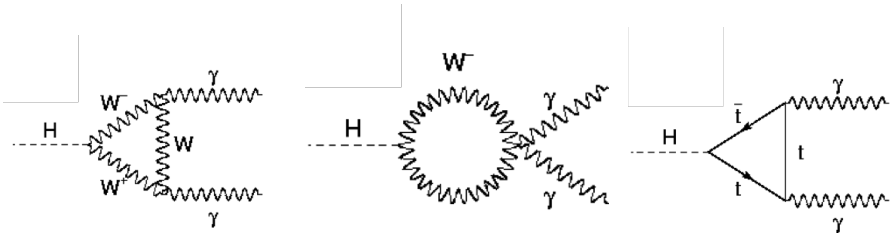

(a) (b) (c)

FIGURE 3.1 – $H \to \gamma\gamma$ decays feynman diagrams.

- At least one of the photons is converted (Conv) or not (Unconv)
- The diphoton system has a p_{Tt} above (High p_{Tt}) or below (Low p_{Tt}) 60 GeV, where the $p_{Tt} = p_T^{\gamma\gamma} \times \hat{t}$ of the diphoton system is defined as the orthogonal component of the diphoton momentum when projected on the thrust axis $\hat{t}$ given by the difference of the photon momenta ($\hat{t} = \frac{p_T^{\gamma 1} - p_T^{\gamma 2}}{|p_T^{\gamma 1} - p_T^{\gamma 2}|}$)
- Both photons pseudo-rapidities are within $|\eta| < 0.75$ (Central), at least one of the photons has $|\eta| > 0.75$ (Rest), or at least one photon is in the transition region between the EM calorimeter barrel and the end-caps $1.3 < |\eta| < 1.37$ or $1.52 < |\eta| < 1.75$ (Transition)
- Two dedicated categories are built for VBF like events (Low mass two-jet category) and (High mass two-jet category)
- Finally a category with at least one lepton is built to collect not gluon fusion events but instead targeting the leptonic VH (ZH or WH) production processes (One lepton category).

The number of categories do not exactly amount to 15 ($2 \times 2 \times 3 + 3$) but to 12 since some low resolution categories are merged because their splitting does not improve significance (for instance Conv Transition High p_{Tt} and Conv Transition Low p_{Tt}). The categories were optimised in terms of gain in sensitivity, which arises from creating categories where events have a very good $m_{\gamma\gamma}$ peak resolution. In terms of analysis optimisation, my personal contribution was about an alternative method developed in section 3.1.3. It is to be noted the number of categories to the $H \to \gamma\gamma$ analysis increased drastically with additional luminosity, reaching 31 in the most recent versions of the analysis [39], 7 of which targeting the $t\bar{t}H$ process [40] developed in part II of this document.

3.1.2 Signal and Background studies

The $H \to \gamma\gamma$ analysis being characterised by the presence of a high resolution mass peak, it consists in searching through a fit for a signal peak over a continuum background. Thanks to the presence of mass sidebands around the peak, the background does not need to be described by Monte Carlo but can simply be fitted inclusively as a decreasing slope. Both signal and background are therefore described by analytical functions.

Signal is parameterised by a crystal ball function whose parameters are different in each category to account for resolution disparities. The crystal ball function is a gaussian core distribution, accounting for the instrumental resolution of the invariant $\gamma\gamma$ mass, with a power law tail on the lower energy side to account for the loss of energy through bremsstrahlung [3], emitted by at least

3. radiation of a photon resulting in a deceleration

one of the electrons in the case of converted photons. Its analytical description is given by :

$$f(t, \alpha_{CB}, n_{CB}) = N_{Signal} \cdot \begin{cases} e^{-t^2/2} & if\ t > -\alpha_{CB} \\ \frac{n_{CB}}{\alpha_{CB}}{}^{n_{CB}} . e^{-\alpha_{CB}^2/2} . (\frac{n_{CB}}{\alpha_{CB}} - \alpha_{CB} - t)^{-n_{CB}} & otherwise \end{cases} \quad (3.1)$$

where $t = (m_{\gamma\gamma} - \mu_{CB})/\sigma_{CB}$. σ_{CB} is the core component of the mass resolution. This was then changed in updated results to a double-sided crystal ball function, consisting of a Gaussian central part and power-law tails on both sides, that was chosen because empirically best fitting the peak from signal simulations.

Signal from gluon fusion is simulated with Powheg interfaced with Pythia while VBF and $t\bar{t}H$ with Pythia. Signal events are generated for Higgs boson masses hypotheses every 5 GeV between 100 and 150 GeV, since the existence and mass of the Higgs boson are still unknown at the time. The parameters of the crystal ball are parameterised as a function of $m_{\gamma\gamma}$ which enables the analysis to be extrapolated in between MC points. The category with the best signal resolution is Unconv Central High p_{Tt} with a resolution in terms of full width at half maximum (FWHM) of 3.22 GeV (σ_E =1.37 GeV). The worst category is Conv Transition with a FWHM resolution of 5.57 GeV (σ_E =2.37 GeV). Figure 3.2 left illustrates MC simulation of the signal fitted by a Crystal Ball function.

The background in the $H \to \gamma\gamma$ analysis is fitted from data sidebands, that are data outside of the window where the Higgs boson mass peak is searched. Despite the analysis not relying on a precise data-driven nor MC based estimate of the irreducible $\gamma\gamma$ and reducible γ-jet and jet-jet backgrounds, its composition is nevertheless studied to make sure the QCD diphoton continuum is understood and corresponds to standard model expectations. The $\gamma\gamma$, γ-jet and jet-jet relative composition is checked thanks to the same three methods that are described in Section 2.3.4 : the 2D sideband, the 4x4 matrix (or event weight) method, and the 2D (template) fit method, with the addition of a fourth method, the 1x2D sideband method which is using a fake rate measured in data to extrapolate background components measured by the 2D sideband method in a control sample to the signal region. I have personally determined the background composition using the 2D Fit method for various datasets. Results show, as illustrated on Figure 3.2 that after all selection cuts the remaining background is 75% irreducible $\gamma\gamma$ or Drell-Yann ($Z \to e^+e^-$ continuum) background, 22% γ-jet and 3% jet-jet.

Monte carlos are used not to describe the background but to allow the choice of analytical function to describe the background in the fit. The $\gamma\gamma$ contribution is simulated with Sherpa, Resbos and Diphox, γ-jet by Sherpa and the jet-jet by Pythia.

The modelling of the background has been carefully studied. Many models, mainly variants of polynomials and decreasing exponential have been tested and chosen to minimise the possibility of a spurious signal arising from it. For each function, a S+B fit (Signal + Background, meaning a sum of the analytical function chosen for the background and the signal crystal ball) is performed to a background only Monte Carlo mixture. The tested model must have a fitted number of signal event either lower than 20% of the background statistical uncertainty, or below 10% of the total number of expected signal events. This fitted number of signal events is used as systematic uncertainty on the background modelling. The chosen background model, depending on the category, is either the exponential of a second-order polynomial, a single exponential, or a fourth-order Bernstein polynomial : $B_n(x) = \sum_{\nu=0}^{n} \beta_\nu b_{\nu,n} = \sum_{\nu=0}^{n} \beta_\nu \binom{\nu}{n} x^\nu (1-x)^{n-\nu}$. The parameters of the analytical functions are determined in the 100 to 160 GeV mass range.

I have been responsible for the internal note dedicated to background studies [37] with the statistics used for the discovery of the Higgs boson in 2012 [41].

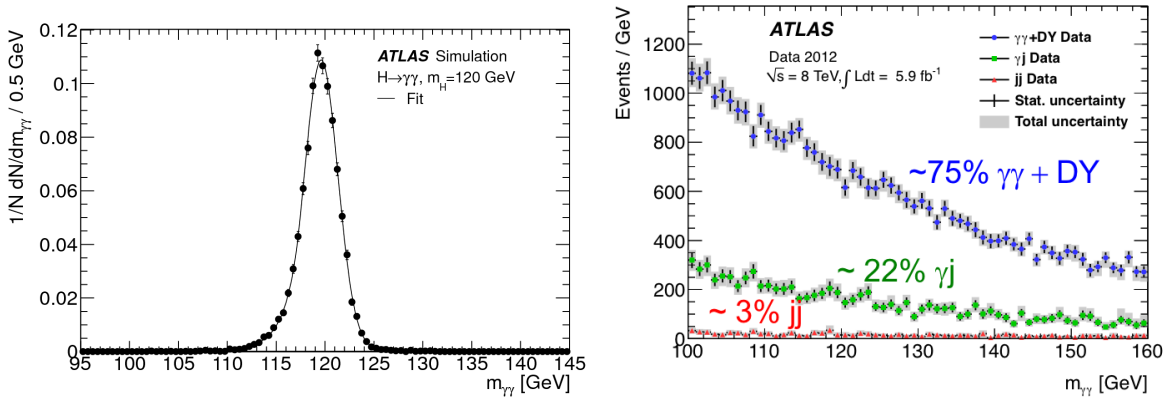

FIGURE 3.2 – Crystall ball signal modelling on simulation (left) [41]. $H \to \gamma\gamma$ background composition (right) [42].

Figure 3.5 shows the result of an signal-plus-background (S+B) fit to data where the background is modelled by a fourth degree Bernstein polynomial.

3.1.3 Analysis optimisation

During the analysis optimisation phase, I investigated the possibility to improve the analysis sensitivity by fitting not only the $m_{\gamma\gamma}$ distribution but also simultaneously the calorimetric isolation of both photons, resulting in a three-dimensional ($m_{\gamma\gamma}$, $E_{T,1}^{iso}$, $E_{T,2}^{iso}$) fit. The isolation of both photon candidates is providing additional information about the probability for an event to be a reducible background γ-jet and jet-jet. This method, reported in an ATLAS internal note [43], was discarded in favour of a quicker simpler categorisation method, that fitted better the limited timescale by which the collaboration was to publish the discovery.

In this method, the traditional Higgs to two photons analysis consisting in a one dimensional maximum likelihood fit of the invariant mass is replaced by a three dimensional fit where the invariant mass and the transverse isolation energy of each photon candidate are used as discriminating variables. The PDF used for the nominal extended profiled likelihood fit for the $H \to \gamma\gamma$ analysis :

$$f_{S+B}(m_{\gamma\gamma}) = n_S f_S(m_{\gamma\gamma}) + n_B f_B(m_{\gamma\gamma}) \tag{3.2}$$

Where n_S and n_B are the numbers of signal and background, $f_S(m_{\gamma\gamma})$ is a Crystal Ball and $f_B(m_{\gamma\gamma})$ is a polynomial. For both f_S and f_B, parameters are determined independently per category, since the background slope and the signal resolution depends highly on the η and conversion status of photons. In the 3D fit instead, the PDF used for the nominal extended profiled likelihood fit for the $H \to \gamma\gamma$ analysis is :

$$\begin{aligned} f_{S+B}(m_{\gamma\gamma}, E_{T,1}^{iso}, E_T^{iso,2}) = {} & n_S f_S(m_{\gamma\gamma}) f_{\gamma,1}(E_{T,1}^{iso}) f_{\gamma,2}(E_{T,2}^{iso}) \\ & + n_{\gamma\gamma} f_B(m_{\gamma\gamma}) f_{\gamma,1}(E_{T,1}^{iso}) f_{\gamma,2}(E_{T,2}^{iso}) \\ & + n_{\gamma j} f_B(m_{\gamma\gamma}) f_{\gamma,1}(E_{T,1}^{iso}) f_{j,2}(E_{T,2}^{iso}) \\ & + n_{j\gamma} f_B(m_{\gamma\gamma}) f_{j,1}(E_{T,1}^{iso}) f_{\gamma,2}(E_{T,2}^{iso}) \\ & + n_{jj} f_B(m_{\gamma\gamma}) f_{j,1}(E_{T,1}^{iso}) f_{j,2}(E_{T,2}^{iso}) \end{aligned} \tag{3.3}$$

The principle of this method is alike the 2D fit method used in the di-photon cross section (Section 2.3), with the exception of the correlations between the leading and subleading jet in di-jet events that are neglected. The calorimetric isolation of the leading and the subleading objects allows an intrinsic separation of the irreducible photon-photon background and its reducible photon-jet and jet-jet backgrounds which results in an improvement of the overall fit sensitivity. Invariant mass and isolation correlations are found to be less than 1% for photons produced in QCD processes, less than 6% for jets while an anti-correlation of 6% (leading) and 11% (subleading) is observed for the photons produced by a Higgs boson decay. Results on $4.91 fb^{-1}$ of 7 TeV data show an improvement of 5% of sensitivity in both the inclusive scenario and the nine category scenario used for the standard Higgs to two photons analysis performed on 2011 data, meaning that the improvement is orthogonal to that brought by categorisation. Systematic uncertainties from background definition and its impact on the sample gamma gamma purity and the isolation probability density functions lower the relative improvement to 3% in the most conservative approach. Results with $5.9 fb^{-1}$ of 8 TeV data and for Higgs searches around a di-photon invariant mass of 125 GeV give an even more optimistic 10% improvement with respect to the baseline Higgs to two photons analysis. The better results achieved with 2012 data could originate from a lower purity of the identification due to higher pile-up.

3.1.4 Systematic uncertainties

In this analysis several kind of systematic uncertainties are taken into account and fall into the following categories :

- Systematic uncertainties on the signal yield : luminosity (±3.9-3.6%@7-8 TeV), trigger (0.5%), identification (5.3%) and isolation (1%) efficiencies, photon energy scale (0.4%), $H \to \gamma\gamma$ branching ratio (decreasing from ±5.9% @ $m_{\gamma\gamma}$= 110 GeV to ±2.1% @ $m_{\gamma\gamma}$= 150 GeV), theoretical uncertainties on the Higgs boson production from the QCD factorisation and renormalisation scales, Parton Distribution Functions (PDFs) and the strong coupling α_S (up to 8% each).
  The QCD scale uncertainty is determined by varying the factorisation and the renormalisation scales μ_F, μ_R of the running coupling of α_s which is a key parameter in making precise perturbative QCD predictions. The PDF+α_s uncertainty account respectively for the uncertainty on the partons Probability Density Functions in the colliding protons, and the uncertainty on the strong coupling constant itself.
- Systematic uncertainties on the signal resolution : calorimeter energy resolution (12%), extrapolation from the electron calibration to photons (6%), pile-up potential mis-modelling (1.5%)
- Systematic uncertainties on the signal migration between categories : jet energy scale and modelling of the underlying events impact mainly the number of events selected in di-jet categories ; Higgs boson kinematics adds uncertainty to the splitting between high and low p_{Tt} categories ; the material mis-modelling uncertainty impacts the split between converted and unconverted photons ; lepton reconstruction, energy scale and identification uncertainties modifies selection of WH, ZH and ttH events in the one-lepton category.
- Systematic uncertainties on the mass measurement : Because of a tension in 2012 between the Higgs boson mass measured in the $H \to \gamma\gamma$ and the $H \to ZZ$ channels, with a lower value for $H \to ZZ$, additional cross checks and systematic uncertainties were investigated to increase the robustness of the $m_{\gamma\gamma}$ result. It included several investigations of the impact of

the following on the peak position : the electron energy scale from $Z \to e^+e^-$ (0.3%), electrons to photon extrapolation (0.3%), pre-sampler scale uncertainty (0.1%) non-linearities of the EM calorimeter electronics (0.15%), uncertainty on the corrections to the cluster lateral energy leakage measured on Z (0.1%), uncertainty on the signal resolution (0.15%), uncertainty on the fraction of converted photons of 10% (0.13%), relative calibration of first and second EM calorimeter samplings (0.2%), uncertainty from the angle measurement evaluated by using various primary vertex selection algorithms on $Z \to e^+e^-$events (0.03%), uncertainty arising from the background modelling, determined by measuring the maximum median deviation of various background models on pseudo-datasets or toys (0.1%). The resulting voluntarily conservative total systematic uncertainty on the mass determination amounts to 0.5% (650 MeV).

For the full run 1 measurement, the electron and photon energy calibration was completely revisited and improved [44].

3.1.5 Statistical method for signal extraction

A profile likelihood ratio based test statistic is used to test different hypothesised values of the signal strength μ, the signal strength for a process i being the product of the measured production cross section and branching ratio over that predicted by the standard model :

$$\mu = \frac{(\sigma \times Br)^{meas}}{(\sigma \times Br)^{SM}} \tag{3.4}$$

In the profiled likelihood ratio fit, the likelihood $\mathscr{L}$ is maximised. The (modified) test statistics q_μ ($\tilde{q_\mu}$), is defined to quantify how well the observed data agrees with the signal plus background hypothesis in the context of a signal strength measurement (upper limit setting) :

$$q_\mu = (\tilde{q_\mu} =) = -2ln(\lambda_\mu) = \begin{cases} -2ln\frac{\mathscr{L}(\mu,\hat{\hat{\theta}})}{\mathscr{L}(\hat{\mu},\hat{\theta})} & 0 < \hat{\mu} < \mu \\ 0 & \hat{\mu} \geq \mu \\ -2ln\frac{\mathscr{L}(\mu,\hat{\hat{\theta}})}{\mathscr{L}(0,\hat{\hat{\theta}}(0))} & \hat{\mu} < 0 \end{cases} \tag{3.5}$$

where μ is the tested value, $\hat{\mu}$ the measured signal strength, $\hat{\hat{\theta}}$ are the values of nuisance parameters that maximises the likelihood for a specified signal strength μ, and $\hat{\theta}$ are the values of the nuisance parameters that maximises the likelihood for the tested $\hat{\mu}$ value. The particular case for which the signal strength $\mu = 0$ is the background-only hypothesis, is tested with $\tilde{q_0} = -2ln(\lambda_0)$. For frequentists, a discovery can be claimed when the compatibility of data with the background-only hypothesis is low enough.

For a Higgs boson mass measurement, μ is treated as a nuisance parameter, and the likelihood ratio function is changed into :

$$\lambda_{m_h} = \frac{\mathscr{L}(m_h, \hat{\hat{\mu}}, \hat{\hat{\theta}})}{\mathscr{L}(\hat{m_h}, \hat{\mu}, \hat{\theta})} \tag{3.6}$$

The Nuisance Parameters (NP) are typically the systematic uncertainties of the analysis that broadens the profile likelihood and degrade the accuracy on $\hat{\mu}$. The value of these parameters are determined from a likelihood fit to data, which is called profiling.

In equation 3.5, higher values of $\tilde{q}_\mu$ correspond to increasing incompatibility between data and the measured signal strength μ. The first condition is the default test statistics definition,

resulting in a χ^2 distribution. The second condition is the capping, which states that if the measured signal strength is higher than the tested value ($\hat{\mu} > \mu$), then $\tilde{q_\mu}$ will be signal-like and not background like. Instead of populating the tail of the $\tilde{q}_\mu$ distributions, events with higher signal strength than the tested value create a Dirac peak at $q_\mu = 0$. Finally the third condition is the one-sided definition, added to tackle with the impossibility of having negative values of a signal strength, which would amount to stating the physical impossibility of measuring a negative number of signal events. Therefore, for negative measured values, $\hat{\mu}$ is set to 0. This modified test statistics is written $\tilde{q}_\mu$. The one-sided test if preferred for discoveries (when measuring the p_0, see below), or for finding an upper-limit, whereas the two-sided definition is used when trying to measure the signal strength. In that last case the number of signal events can be negative up to the point that the total number of events, signal and background, is not negative in which case the function is not defined. That can happen for very pure regions for which no data event is selected, such as for the run 1 version of the four leptons category of the $t\bar{t}H$ analysis (see section 6.1.1.1).

The p-value quantifies the statistical significance of an observed signal :

$$\begin{aligned} p_\mu &= \int_{\tilde{q}_{\mu,obs}}^{+\infty} f(\tilde{q}_\mu \mid \mu) d\tilde{q}_\mu \\ p_0 &= \int_{\tilde{q}_{0,obs}}^{+\infty} f(\tilde{q}_0 \mid 0) d\tilde{q}_0 \end{aligned} \tag{3.7}$$

The p_0 value is the probability of data to be compatible with the background-only hypothesis. P-values can be translated into a Gaussian statistical significance Z or standard deviations through the quantile (inverse of the cumulative distribution) of the standard Gaussian $Z = \phi^{-1}(1-p)$. an observation or discovery is claimed when the probability for data to be compatible with the background-only hypothesis is three chances out of ten million (p=2.87×10^{-7} or Z=5 σ), and an evidence when the probability for data to be compatible with the background-only hypothesis is one out of a thousand (p=1.35×10^{-3} or $Z = 3\sigma$). The commonly used p-value of 0.05 is equivalent to a 95% Confidence Level ($CL = 1 - p$) and amounts to Z=1.96 $\simeq$ 2 σ.

The p_0 at a particular $m_{\gamma\gamma}$ is represented on Figure 3.5 on the right, also called the discovery plot. The result is to be considered in light of the look elsewhere effect (LEE), which accounts for fact that the probability of observing an excess when testing a whole mass range (here 110 GeV to 160 GeV) is higher that checking for an excess at a specific mass point [45].

A frequentist procedure is used to derive exclusion limits on μ using CL_S which is the probability to have data compatible with the signal hypothesis knowing the background.

$$CL_S = 1 - p_S = 1 - \frac{p_{S+B}}{1 - p_B} = 1 - \frac{1 - CL_{S+B}}{CL_B} \tag{3.8}$$

where CL_{S+B} is the test for the signal+background hypothesis and CL_B is the test for background only hypothesis ($\mu = 0$).

A median significance can be defined assuming data is distributed according to a specified signal model, with which one would expect to exclude the background-only hypothesis. This is done by setting μ' in $f(q_0 \mid \mu')$ from equation 3.7 ; in our case the Standard Model signal strength for the Higgs boson signal $\mu' = 1$. The estimate of the median significance by replacing the ensemble of simulated data sets by a single representative one, here referred to as an *Asimov*[4]

4. The name comes from the short novel *Franchise* by science fiction author Isaac Asimov, where an election is held with a single representative voter to replace all.

dataset [46]. In the rest of this document, expected results are obtained by performing a fit on the representative Asimov dataset of a Signal+Background model where the signal strength is that of the Standard Model Higgs boson ($\mu = 1$). Observed values are instead the ones obtained from the fit to the recorded data.

The asymptotic approximation of the likelihood statistical interpretation states that the distribution of the test statistic $\tilde{q}_\mu$ defined in equation 3.5 is $\frac{1}{2}\delta + \frac{1}{2}\chi^2$, that is the sum of half a Dirac and half a χ^2. One consequence from this is the significance can be obtained from the measured test statistics with the formula $Z = \sqrt{q}_{meas}$. Most of ATLAS statistical interpretations rely on this approximation which is valid for sufficiently high statistics analyses. Large numbers of simulated pseudo-experiments, also called Toy Monte Carlos, are used for cross checks or for low statistics channels, such as $t\bar{t}H$ to four leptons (See Section II). Both observed and expected significances are therefore determined by the value of the test statistics measured on data for the observed ($Z = \sqrt{q}_{obs}$) and on an Asimov dataset for the expected ($Z = \sqrt{q}_{Asimov}$).

3.1.6 $H \to \gamma\gamma$ analysis results

Between 2011 and 2013, I was regularly updating the $H \to \gamma\gamma$ statistical results and giving a report in the group meeting. As LHC data was accumulating, there was enough material to update results from Paris every week and compare to those from Wisconsin university whose team was performing the same task with a different framework. These were both stressful and exciting times since we knew a bump could appear anywhere in the 110 to 160 GeV mass range. The most significant bump to be seen was one in the exclusion plot as illustrated on Figure 3.3. At this point measuring the p_0 became more appropriate to check the statistics was sufficient to confirm the excess around 126 GeV (see figure 3.4). On July 2012, a Higgs boson-like particle observation was announced jointly by ATLAS and CMS.

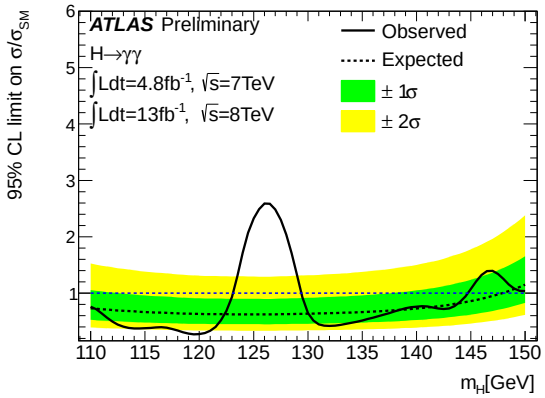

FIGURE 3.3 – The observed 95% CL exclusion of value of μ as a function of $m_{\gamma\gamma}$ and the expected (dashed) corresponding to the background-only hypothesis, from the combination of the 7 and 8 TeV data. This limit can however not be applied to a second boson since the fit assumes only one contribution [38].

The significance of the excess combined over all data years and channels occurs at m_H= 126.5 GeV with an observed significance of 6.0σ (p_0=1.7×10^9) [47], for 4.9σ expected from a Standard Model Higgs ($\mu = 1$). This observation was consistent with the indirect constraints from the global fit to precision electroweak measurements [48] which arises from the Higgs boson

mass being linked to the masses of the W boson and the top quark. This result could be achieved by combining the following final states :

- $H \to \gamma\gamma$ (4.7 fb^{-1} of 7 TeV and 5.8 fb^{-1} of 8 TeV data)
- $H \to WW$, WW $\to l\nu l\nu$, $l\nu qq'$ (7 TeV) ; e$\nu\mu\nu$ (8 TeV)
- $H \to ZZ$, ZZ $\to 4\ell$, ll$\nu\nu$, llq$\bar{q}$ (7 TeV) ; 4ℓ (8 TeV)
- VH, H$\to b\bar{b}$, Z$\to \nu\nu$, W$\to l\nu$, Z$\to$ ll (7 TeV)
- $H \to \tau\tau$, $\tau_{lep}\tau_{lep}$, $\tau_{lep}\tau_{had}$, $\tau_{had}\tau_{had}$ (7 TeV)

The result also included an exclusion at 95% CL of the mass range between 110 and 582 GeV at the exception of the excess around $m_H \simeq 126$ GeV. The mass range beyond 150 GeV is covered in particular by the $H \to WW$ and the $H \to ZZ$ channels since these decay modes are predominant at higher masses of the Higgs boson. For the mass determination, the $H \to \gamma\gamma$ and $H \to ZZ$ high resolution channels are considered. As illustrated on Figure 3.4, $H \to \gamma\gamma$ was at the time of the first combined discovery the leading channel.

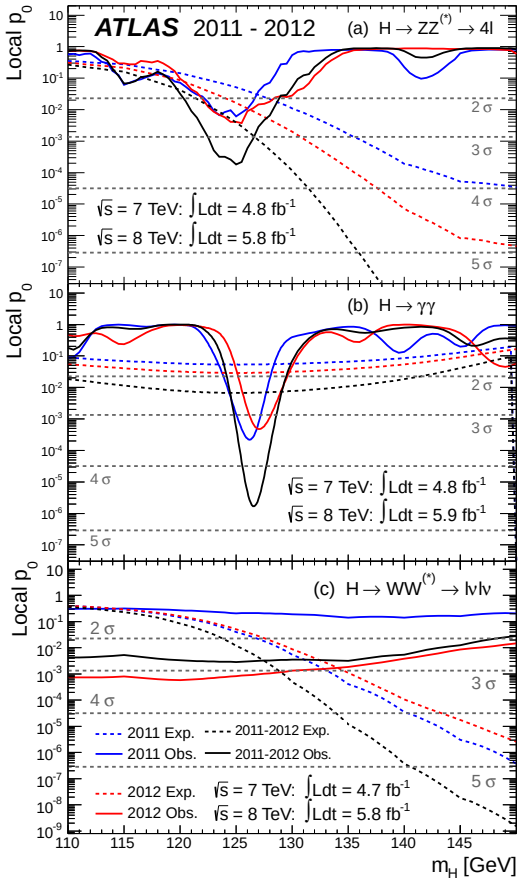

FIGURE 3.4 – $H \to ZZ$, $H \to \gamma\gamma$ and $H \to WW$ p_0 values for ICHEP conference, July 4th, 2012 [47].

The release of the subsequent $H \to \gamma\gamma$ public result with 20 fb^{-1} of 7&8 TeV data in December 2012 as a conference note of which I was editor, confirmed the combined discovery achieved in July 2012, and was the first observation of the Higgs boson with a standalone channel.

The significance of the excess with the almost doubled statistics of 20 fb^{-1} was 6.1σ (5.4σ after LEE correction), corresponding to a p-value of p_0=4.4×10^{10} (p_0=2.8×10^8), as illustrated in Figure 3.5. The expected value for a Standard Model like Higgs boson signal strength of $\mu = 1$ was 3.3σ, which means if the Higgs boson was the standard one, that there was an upward fluctuation of the signal in this dataset which lead to a measured signal strength above the Standard Model expected value : μ= 1.80 ± 0.30 (stat)$^{+0.21}_{-0.15}$(syst)$^{+0.20}_{-0.14}$ (theory).

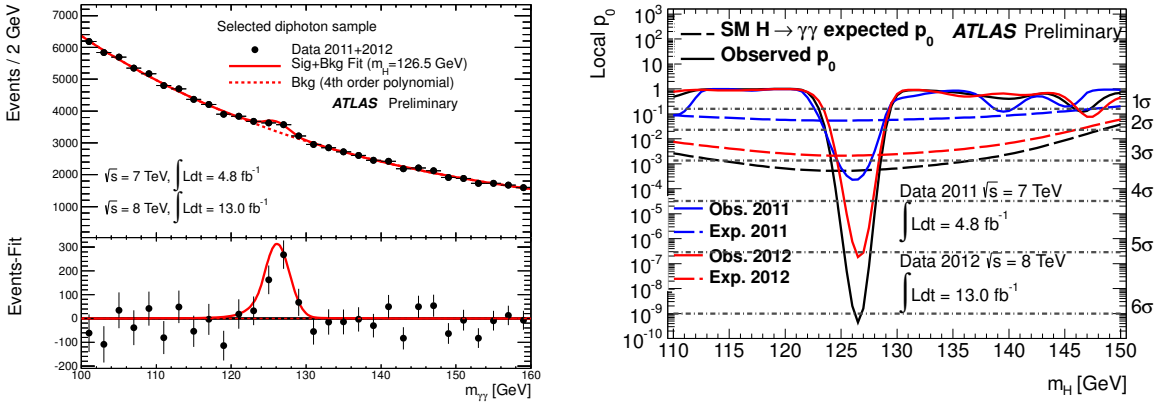

FIGURE 3.5 – $H \to \gamma\gamma$ invariant mass (left) and p_0 as a function of the diphoton mass for CERN council, December 13th, 2012 [38].

For the new particle's mass measurement, the parameter of interest in the test statistic is changed to m_H as explained in equation 3.6, and the signal strength parameter is treated here as a nuisance parameter. The best-fit value is m_H= 126.6 ± 0.3 (stat) ± 0.7 (syst) GeV. In that public result, and to go one step further down the road of Higgs couplings measurements, Higgs production modes signal strength were allowed to float independently to exploit the specific production enriched categories. With 20 fb^{-1} of 8 TeV data, gluon fusion (ggF) was grouped with ttH since they are both result of the coupling of the Higgs boson to the top quark (fermion), as illustrated on Figure 3.1 while VBF and VH strength, coupled together since both depend on its coupling to bosons. The result of this fit is the two-dimensional ellipse shown in Figure 3.6 left. The updated result with 36.1 fb^{-1} of 13 TeV data allowed to split further to each production mode (see figure 3.6 right). This work on the couplings is still an on-going effort in the $H \to \gamma\gamma$ team with the latest published result having nine ttH/tH, seven VH, four VBF and ten gluon fusion dedicated categories [39]. The latest result amounts in particular to a 1σ precision on the signal strength for top μ_t. Part II of this document is devoted to the couplings measurement of the Higgs boson, in particular to the top quark.

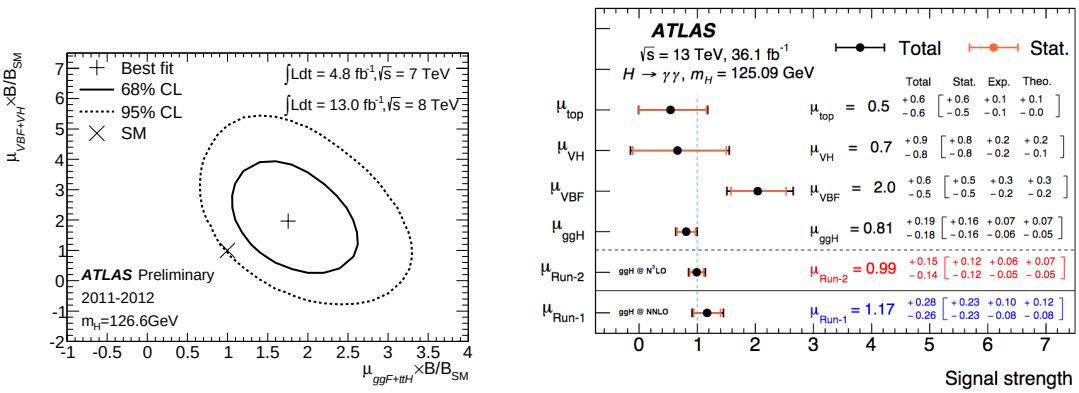

FIGURE 3.6 – Best-fit values of $\mu_{ggF+ttH} \times B/B_{SM}$ and $\mu_{VBF+VH} \times B/B_{SM}$ where B is the Higgs to gamma gamma branching ratio, and their 68 % (solid) and 95 % (dashed) CL contours (left) [38]. $H \to \gamma\gamma$ coupling results with 36.1 fb^{-1} of 13 TeV data (right) [39].

3.2 Spin Tests

Right after its discovery, one important step towards the characterisation of this newly discovered particle and its properties measurement was to check it was indeed a scalar as predicted by the Standard Model (see section 1.2.3). In 2013, I participated to the first study of the spin of the Higgs-boson-like particle in its $H \to \gamma\gamma$ decay [49].

3.2.1 Theoretical motivation

Spin and parity are quantum numbers, *i.e.* intrinsic quantum quantities used to characterise the particle. They are subject to conservation laws. Among quantum numbers one can count angular momentum, spin, parity, and charge parity [5].

Parity P is equal to +1 or -1 and related to the particle properties under a reflection in space, for example to whether the decays of the particle into two mirror-symmetric configurations, have an identical probability or not.

For the Higgs boson, spin and parity are determined by the Standard Model to be $J^P=0^+$, in other words the Higgs boson is a scalar. The observation of the Higgs boson in its $H \to \gamma\gamma$ decay discards the spin-1 hypothesis because of the Landau-Yang theorem that forbids the direct decay of an on-shell spin-1 particle into a pair of massless spin 1 particles. Elements of its conceptual demonstration is the following. The projection of the total angular momentum on the di-photon's direction is the difference in helicity of both photons $\lambda_1 - \lambda_2$. The helicity of one photon being $\lambda=\pm1$, $|\lambda_1 - \lambda_2|$ can either be 0 or 2. Now, by conservation, the angular momentum is that of the initial decaying particle. In case of a spin-1 particle decaying to two photons, $|\lambda_1 - \lambda_2| \leq 1$ and thus $\lambda_1 = \lambda_2$. It can be shown that the di-photon quantum state respecting the Bose symmetry, allowing for which both photons can we swapped, can be written :

$$| \gamma_1, \gamma_2 \rangle = | \lambda_1, \lambda_2 \rangle + (-1)^J | \lambda_2, \lambda_1 \rangle$$

Since the total angular momentum must be conserved, J=1. It results that for a spin-1 particle, the two di-photon state would be null which results in a contradiction.

3.2.2 Instrumental setup

In this result, and in order to reach evidence for a spin-0, the $\gamma\gamma$ final state has been combined with other more sensitive decay channels : the $H \to WW \to e\nu\mu\nu$ and $H \to ZZ \to 4\ell$ channels. Thanks to the several leptons in their final states, they are more sensitive to parity as well as the spin through the numerous angular observable. In particular in this paper, $J^P=0,1^+,1,2^+$ models are excluded at confidence levels above 97.8%. The study provides evidence for the spin-0 nature of the Higgs boson, and a strong preference for positive parity.

In the present document I will nevertheless focus on the description of my contribution on the $H \to \gamma\gamma$ channel which, for a graviton-like spin-2 particle with minimal couplings described in section 3.2.3, is only sensitive to spin and not parity, providing therefore a discrimination against the $J^P=2^+$ hypothesis [6]. Spin studies have been since then updated with additional integrated luminosity [50], but I will focus on the 2013 result that I participated to.

5. Charge conjugation is the operation that changes the sign of all elementary quantum charges effectively transforming a particle to its anti-particle.

6. As opposed to more original spin-2 models for which $H \to \gamma\gamma$ could provide some parity discrimination.

3.2.3 Spin-2 model

The alternative model descriptions is a spin-2 model originating from the most generic couplings model of spin-2 resonances as explained in [51], where the production and decay of a generic boson with various J^P quantum numbers are described. The most general amplitudes are defined, to be consistent with Lorentz invariance, angular-momentum conservation, Bose symmetry and the unbroken symmetry of the SU(3)×SU(2)×U(1) gauge group.

The general interaction of spin-2 particle with gauge bosons pair has ten independent tensor couplings making the exclusion of the generic spin-2 model impossible at this stage for statistics reasons. Among the large number of possible spin-2 models arising from this general description, only one is chosen : the 2^+_m graviton-like tensor with minimal couplings defined as $g_1^{(2)} = g_5^{(2)} \neq 0$ highlighted on figure 3.7, in which the only dependency of the model are the intensities of the spin-2 particle to the standard model fields.

$$
\begin{aligned}
A(X \to VV) = \Lambda^{-1} \Bigg[& 2g_1^{(2)} t_{\mu\nu} f^{*1,\mu\alpha} f^{*2,\nu\alpha} + 2g_2^{(2)} t_{\mu\nu} \frac{q_\alpha q_\beta}{\Lambda^2} f^{*1,\mu\alpha} f^{*2,\nu,\beta} \\
& + g_3^{(2)} \frac{\tilde{q}^\beta \tilde{q}^\alpha}{\Lambda^2} t_{\beta\nu} (f^{*1,\mu\nu} f^{*2}_{\mu\alpha} + f^{*2,\mu\nu} f^{*1}_{\mu\alpha}) + g_4^{(2)} \frac{\tilde{q}^\nu \tilde{q}^\mu}{\Lambda^2} t_{\mu\nu} f^{*1,\alpha\beta} f^{*(2)}_{\alpha\beta} \\
& + m_V^2 \left(2g_5^{(2)} t_{\mu\nu} \epsilon_1^{*\mu} \epsilon_2^{*\nu} + 2g_6^{(2)} \frac{\tilde{q}^\mu q_\alpha}{\Lambda^2} t_{\mu\nu} \left(\epsilon_1^{*\nu} \epsilon_2^{*\alpha} - \epsilon_1^{*\alpha} \epsilon_2^{*\nu}\right) + g_7^{(2)} \frac{\tilde{q}^\mu \tilde{q}^\nu}{\Lambda^2} t_{\mu\nu} \epsilon_1^* \epsilon_2^* \right) \\
& + g_8^{(2)} \frac{\tilde{q}_\mu \tilde{q}_\nu}{\Lambda^2} t_{\mu\nu} f^{*1,\alpha\beta} \tilde{f}^{*(2)}_{\alpha\beta} + g_9^{(2)} t_{\mu\alpha} \tilde{q}^\alpha \epsilon_{\mu\nu\rho\sigma} \epsilon_1^{*\nu} \epsilon_2^{*\rho} q^\sigma + \frac{g_{10}^{(2)} t_{\mu\alpha} \tilde{q}^\alpha}{\Lambda^2} \epsilon_{\mu\nu\rho\sigma} q^\rho \tilde{q}^\sigma \left(\epsilon_1^{*\nu} (q\epsilon_2^*) + \epsilon_2^{*\nu} (q\epsilon_1^*)\right) \Bigg]
\end{aligned}
$$

FIGURE 3.7 – Most general couplings of spin-two resonances to Standard Model matter and gauge fields expression, and graviton-like tensor with minimal couplings ($g_1^{(2)} = g_5^{(2)} \neq 0$) used for this result highlighted in blue [51].

Two production mechanism are considered for this spin-2 model : gluon fusion gg initial state, or the quark-antiquark annihilation process $q\bar{q}$. The gg mechanism is dominant at leading order in Quantum Chromodynamics (QCD), but that ratio can be significantly modified at higher order QCD corrections, so that the analysis was performed for various proportions [7] of quark-anti-quark annihilation $f_{q\bar{q}} = 1 - \epsilon_{2gg}$ between 0 and 100 % by steps of 25%.

The SM $H \to \gamma\gamma$ production and decay is generated by Powheg+Pythia, while the spin-2 alternative model 2^+ is modelled by the leading order QCD generator described in [51] and denominated *JHU* in reference to Johns Hopkins University where it has been developed. They are then both interfaced with Pythia8 for parton showering and hadronisation. I developed a tool to reweigh p_T distributions for the gluon fusion signals from JHU to reproduce the Powheg+Pythia8 spectrum of the SM spin-0 hypothesis. No reweighing was applied to the $q\bar{q}$ production process, but it was checked that the distributions of all kinematic variables used for the spin analysis are compatible between the two MC after that reweighing is applied.

The $H \to \gamma\gamma$ decay mode is sensitive to the spin of the Higgs boson through the measurement of the polar angular distribution of the photons in the resonance rest frame. The discriminating variable is $|cos(\theta^*)|$, the polar angle of photons with respect to the z axis in the Collins-Soper

7. So here $f_{q\bar{q}}$ is not a pdf but a fraction of production mode

frame :

$$cos(\theta^*) = \frac{sinh(\eta_{\gamma_1} - \eta_{\gamma_2})}{\sqrt{1 + (p_T^{\gamma\gamma}/m_{\gamma\gamma})^2}} . \frac{2p_T^{\gamma_1} p_T^{\gamma_2}}{m_{\gamma\gamma}^2} \tag{3.9}$$

In this frame, as illustrated on figure 3.8 the x-axis is chosen to bisects the angle between the momenta of incoming hadrons p_A and p_B, the z-axis defined as bisectrix of p_A and $-p_B$ and finally a y-axis to complete a right handed coordinate system. This referential was chosen as it is in principle least sensitive to ISR and has also shown to be the most discriminant between spin-0 and spin-2.

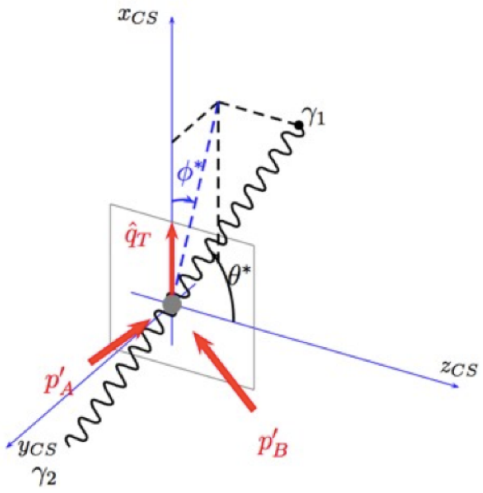

FIGURE 3.8 – Illustration of Collins-Soper referential.

The $|cos(\theta^*)|$ discrimination comes from the different profiles of each process determined from the helicity formalism with Wigner's coefficients :

- ⇝ The SM Higgs with spin-0 has a flat behaviour because of an isotropic decay → it is a uniform distribution before acceptance cuts.
- ⇝ Spin-2 production via gluon fusion : $\frac{dN}{dcos(\theta^*)} \propto 1 + 6cos^2(\theta^*) + cos^4(\theta^*)$
- ⇝ Spin-2 production via quark-anti-quark : $\frac{dN}{dcos(\theta^*)} \propto 1 - cos^4(\theta^*)$

These truth level distribution are then convoluted by instrumental acceptance cuts, and in particular the usual photon kinematic cuts $p_T > 25$ GeV and $|\eta|$ <2.5 cuts that remove events in the high-end of the $|cos(\theta^*)|$ distribution. $|cos(\theta^*)|$ distributions for all of these processes is given on Figure 3.9 left, showing there is a good discrimination for gg initiated final states but low for the $q\bar{q}$. The discrimination is therefore better for low $q\bar{q}$ production fraction as illustrated on the exclusion Figure 3.9 right.

3.2.4 Fit model

As explained in the previous section, $cos(\theta^*)$ is the variable used to discriminate between the SM Higgs and the spin-2 hypothesis. To discriminate against the non-resonant $\gamma\gamma$ background, $m_{\gamma\gamma}$ is also used as a discriminating variable. The fit is a one-dimensional $m_{\gamma\gamma}$ fit in the mass

sideband regions ($m_{\gamma\gamma} \in [105;122]$ & $[130;160]$ GeV), and two-dimensional $m_{\gamma\gamma} \times cos(\theta^*)$ in the signal (peak) region between 122 and 130 GeV. The 2D fit in the signal region required a thorough check of the correlations between $m_{\gamma\gamma}$ and $cos(\theta^*)$ which revealed not to be significant compared to the statistical uncertainties. The residual correlation at the level of 0.6% for $cos(\theta^*) < 0.8$ and 2% elsewhere is treated as a systematic uncertainty.

Background and signal are respectively modelled as a fifth order polynomial and a crystal ball function as in the $H \to \gamma\gamma$ analysis described in section 3.1, but all categories are merged into an inclusive category. The fit to data is therefore carried out simultaneously in the signal region (2D-fit) and the two sideband (1D fit) regions. The use of either one ($m_{\gamma\gamma}$) or two ($m_{\gamma\gamma} \times cos(\theta^*)$) discriminating variables as a function of the invariant mass of the two photons in a single fit turned out to be an original and relevant idea, but prone to many technical difficulties. My participation to this analysis has been mainly to help in the technical elaboration of those unusual statistical workspaces and their production. In the signal region where the fit is performed on the product of the $m_{\gamma\gamma}$ and $cos(\theta^*)$ distributions, the likelihood is of the form :

$$\mathscr{L} = (n_S + n_B) - \sum_{events} ln[n_S.f_S(|cos(\theta^*)|).f_S(m_{\gamma\gamma}) + n_B.f_B(|cos(\theta^*)|).f_B(m_{\gamma\gamma})] \tag{3.10}$$

The $m_{\gamma\gamma}$ dependent part of the background PDF, $f_B(m_{\gamma\gamma})$, is determined from sidebands in the same fashion as is done for the $H \to \gamma\gamma$ signal strength measurement, following the rules of the spurious signal as described in section 3.1.2. The $f_B(|cos(\theta^*)|)$ PDF used in the signal region is also determined from data in the $m_{\gamma\gamma}$ sidebands. The 1D×1D treatment is justified by the fact that $m_{\gamma\gamma}$ and $cos(\theta^*)$ are assumed to be uncorrelated, which is insured by applying photon acceptance cuts on $p_T / m_{\gamma\gamma}$ instead of p_T. A bin-by-bin uncertainty in the $f_B(|cos(\theta^*)|)$ distribution is allowed to float, introduced as degreed of freedom to absorb potential remaining correlation between $cos(\theta^*)$ and $m_{\gamma\gamma}$. Most of technical difficulties came from the use of this 1D(binned)×1D(analytical) PDF.

The signal PDF, for reasons developed in section 3.2.3 is parameterised as a function of the gluon-gluon and quark-quark initiated spin-2 components :

$$f_S(cos(\theta^*)|\epsilon_0, \epsilon_2) = \epsilon_0 f_0 + (1-\epsilon_0)(\epsilon_{2gg} f_{2gg} + (1-\epsilon_{2gg}) f_{2q\bar{q}})$$

where ϵ_0 (resp ϵ_2) is the probability for the Higgs boson to be a scalar (resp. a spin 2 particle), namely if the spin is 0 (2), $\epsilon_0 = 1(0)$. f_S, f_0, f_{2gg} and $f_{2q\bar{q}}$ are here the pdfs for signal, spin-0, spin-2 initiated by gluon fusion and quark-anti-quark. The exclusion is decreasing with the increasing fraction of $q\bar{q}$ produced signal as shown on Figure 3.9 right. The test statistics to discriminate between the spin-0 (H_{0^+}) and the spin-2 (H_{2^+}) hypotheses consists in the ratio of the two likelihoods :

$$q = -ln\frac{\mathscr{L}(H_{0^+})}{\mathscr{L}(H_{2^+})} = -ln\frac{\mathscr{L}(\epsilon_0 = 1, \hat{\hat{\mu}}_{\epsilon=1}, \hat{\hat{\theta}}_{\epsilon_0=1})}{\mathscr{L}(\epsilon = 0, \hat{\hat{\mu}}_{\epsilon=0}, \hat{\hat{\theta}}_{\epsilon=0})} \tag{3.11}$$

where $\hat{\hat{\mu}}$ is the signal strength and $\hat{\hat{\theta}}$ the nuisance parameters fitted under the spin-0 and spin-2 hypotheses. The distribution for both test statistics is obtained with pseudo-experiments or toys. The p-values are determined by integrating the q distributions of each hypothesis as illustrated on figure 3.10 left. The exclusion of the alternative 2^+ hypothesis in favour of the Standard Model 0^+ hypothesis is evaluated in terms of the corresponding CL_S, defined as $CL_S(2^+) = \frac{p(2^+)}{1-p(0^+)}$.

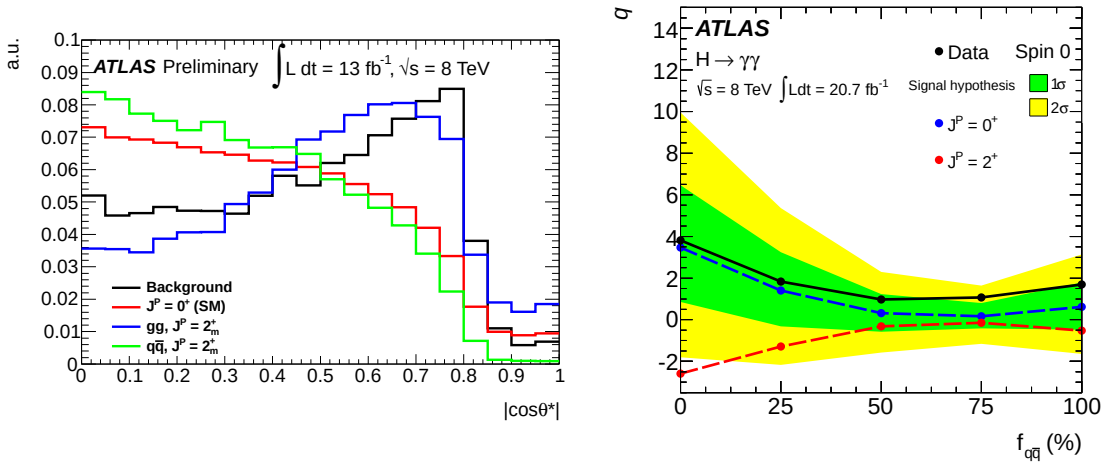

FIGURE 3.9 – Left : Discriminating variable $cos(\theta^*)$ distribution for diphoton background (black) a SM Higgs boson (0^+) (blue), a graviton-like spin-2 tensor with minimal couplings signal (2^+_m) produced from gluon fusion (red), and a graviton-like spin-2 tensor with minimal couplings signal (2^+_m) produced from $q\bar{q}$ (green) after the analysis selection cuts [38]. Right : Observed values of the test statistic q described in equation 3.11 (black solid line) as a function of the fraction of the $q\bar{q}$ production of the spin-2 state $f_{q\bar{q}}$. The blue and red dashed lines indicate the positions of the median expected values of the sampling distributions for the spin-0 and spin-2 signals, respectively, obtained from pseudo-experiments. The green and yellow bands correspond, respectively, to one and two standard deviations around the spin-0 median curve [49].

When the measured data are in agreement with the tested J^P hypothesis, the observed value of q is expected to be close to the median, corresponding to a p-value around 50%. Very small values of the integral of the J^P distribution, corresponding to large values of q, are interpreted as the data being in disagreement with the tested hypothesis. On figure 3.10 left, the result of the fit for the gluon fusion only case is shown. It corresponds to the test statistics q distribution of the first set of points at $f_{q\bar{q}} = 0$ in figure 3.9 right, where the blue (resp. red) distribution is the expected distribution of the test statistics for the 0^+ (resp 2^+) hypothesis, with a central values of $q \simeq 4$ ($q \simeq -2.5$) and the black dot for the observed value around $q \simeq 4$ becomes the black Dirac. It shows the observed fitted value (black Dirac) is poorly consistent with the spin-2 hypothesis in red (because of a low p-value) but highly consistent with the spin-0 SM hypothesis in blue, with a p-value close to 50%.

3.2.5 Results

Figure 3.10 right displays the data distribution for $cos(\theta^*)$ in the signal region, overlaid with the signal and background components, fitted under the $J^P = 0^+$ hypothesis. Figure 3.11 shows the $cos(\theta^*)$ distributions in the signal region obtained after subtracting the estimated background, and compared with the expected distributions for spin-0 and spin-2 signals. Data points are slightly different under the spin-0 and the spin-2 hypotheses because of the profiling of its bin-by-bin systematic uncertainties or nuisance parameters. The spin analysis naturally inherits all systematics related to the $m_{\gamma\gamma}$ fit as they were described in the discovery section. Specific systematics are taken into account for the modelling of $cos(\theta^*)$.

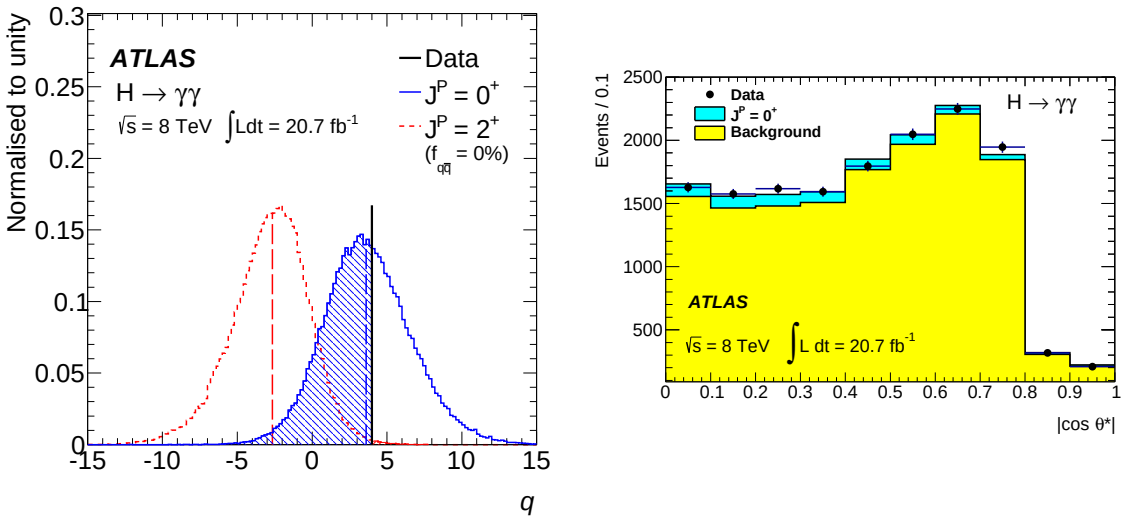

FIGURE 3.10 – Left : Expected distributions of the test statistics q for the spin-0 and spin-2 (produced by gluon fusion) hypotheses. The observed value is indicated by a vertical line. The coloured areas correspond to the integrals of the expected distributions used to compute the p-values for the rejection of each hypothesis. The red dashed area on the right-hand tail is barely visible as the p-value for data to be compatible with spin-2 is very small [49]. Right : Distribution of $cos(\theta^*)$ for events in the $122 < m_{\gamma\gamma}$ GeV < 130 signal region. The data (dots) are overlaid with the projection of the signal (blue) and background (yellow) components obtained from the inclusive fit of the data under the spin-0 hypothesis [49].

- ⇝ Systematics on the SM spin-0 $cos(\theta^*)$ signal modelling (from MC) include the interference between the signal $gg \to H \to \gamma\gamma$ and the non-resonant background $gg \to \gamma\gamma$ [52] and NNLL+NLO corrections to the transverse momentum. The photon identification efficiencies in different pseudo-rapidity and the systematic uncertainty on the photon energy scale are negligible.
- ⇝ Systematics on the spin-2 signal $cos(\theta^*)$ is conservatively taken as the full magnitude of the MC p_T reweighing correction (see section 3.2.3). No interference is considered because there are no theoretical models that describe it.
- ⇝ The uncertainty on the $cos(\theta^*)$ background modelling is lead by the limited statistics in the sidebands and small remaining correlations between $m_{\gamma\gamma}$ and $cos(\theta^*)$, observed in high statistics MC samples (see section 3.2.4) which are summed in quadrature and uncorrelated between bins.

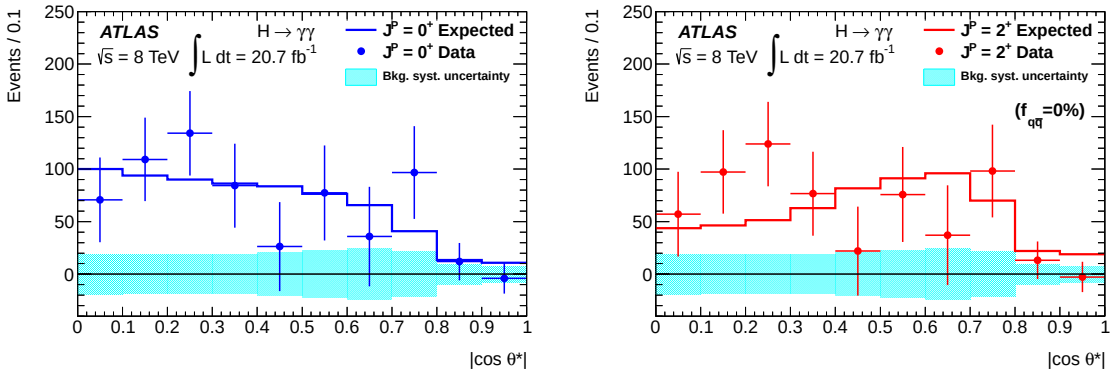

FIGURE 3.11 – $cos(\theta^*)$ distributions of background-subtracted data in the signal region after a fit to data for the spin-0 (left) and spin-2 (right) gluon fusion produced hypotheses. The light blue bands around the horizontal lines at zero show the systematic uncertainties on the background modelling before the fits, which include the statistical uncertainties on the data sidebands [49].

The graviton-like with minimal couplings model hypothesis is excluded by the $H \to \gamma\gamma$ analysis at 99.3% Confidence Level assuming the production mode is 100% gluon fusion ($f_{q\bar{q}} = 0$) which is the scenario ensuring the maximum sensitivity. When combined with the other two bosonic channels $H \to ZZ$ and $H \to WW$ that are less dependent on the quark-anti-quark annihilation fraction, the $J^P = 2^+$ model is rejected at more than 99.9% CL over the whole $f_{q\bar{q}}$ range.

II

$t\bar{t}H$

4. Motivations for $t\bar{t}H$ and couplings measurements

Ever since the Higgs boson was discovered in 2012 (see Section 3.1), interests from the ATLAS and CMS experiments shifted towards the measurement of its properties. The intentions of the community has been to verify whether its spin (see Section 3.2), parity and coupling to other particles correspond to those predicted by the Standard Model (SM) (see Section 1.2.3). Higgs boson couplings are completely determined by the SM and consequently a very good handle for new physics to be spotted. Some couplings, among which the couplings to the top quark, are also challenging measurements.

After the discovery and spin measurement of the Higgs boson in its $H \to \gamma\gamma$ final state in 2013, I decided to continue getting involved in the study of the properties of the newly discovered Higgs boson, and more specifically in its couplings to other particles. The Higgs boson having been initially discovered through its bosonic decays (W, γ, Z), its coupling to bosons did not need to be demonstrated, although still to be measured with improved accuracy. On the contrary some more work was needed at the time to observe its fermionic decays to τ and b-jets. As of today, the Yukawa coupling of the Higgs boson to tau leptons has been observed [53, 54] and observation for the coupling to b-quarks has been found through direct searches [55, 56, 57]. The four dominant Higgs boson production modes and major decays have now been observed. The Yukawa coupling of the Higgs boson to the top quark has however been one of the most challenging couplings to measure and among the last ones to be observed.

In the SM, the fermion couplings to the Higgs boson are proportional to their mass ; the top quark is hence the fermion with the strongest coupling which has been verified by experimental measurements (see Figure 6.10). It is at work in the dominant gluon fusion production mode, but hidden in a loop. The Higgs boson production in association with a top quark pair ($t\bar{t}H$) allows however a direct measurement of this coupling, since the tops are part of the reconstructed final state, as illustrated in Figure 1.5. This measurement is challenging since apart from tH, $t\bar{t}H$ is the rarest production mode, representing only 0.6% of produced Higgs bosons at 8 TeV and 0.9% at 13 TeV, compared to respectively 87% and 88% of production rate for gluon fusion. On the other hand, $t\bar{t}H$ is the Higgs boson production mode that benefited the most from the LHC increase of the centre of mass energy $\sqrt{s}$ from 8 TeV to 13 TeV. The increase of the collisions energy is particularly beneficial to this heavy final state that counts two top quarks of 173 GeV each and a Higgs boson of 125 GeV : $M_{t\bar{t}H} = 2M_{top} + M_{Higgs} \simeq 2 \times 173 + 125 \simeq 471$ GeV. Furthermore, the increase of energy changes the PDF of protons, and gluon initiated processes are the ones that got the most enhanced as illustrated on figure 4.1a. As a result, the $t\bar{t}H$ cross section increased by a factor 3.9 compared to less than a factor 2.3 for other processes as shown on Figure 4.1b (2.0 for WH, 2.1 for ZH, 2.4 for VBF and 2.3 for gluon fusion). The $t\bar{t}H$ production

cross section for a Higgs boson of m_H= 125.0 GeV, computed at next-to-leading order (NLO) in quantum chromodynamics (QCD) with NLO electroweak corrections [58], is 129.3 fb at 8 TeV and 507 fb at 13 TeV.

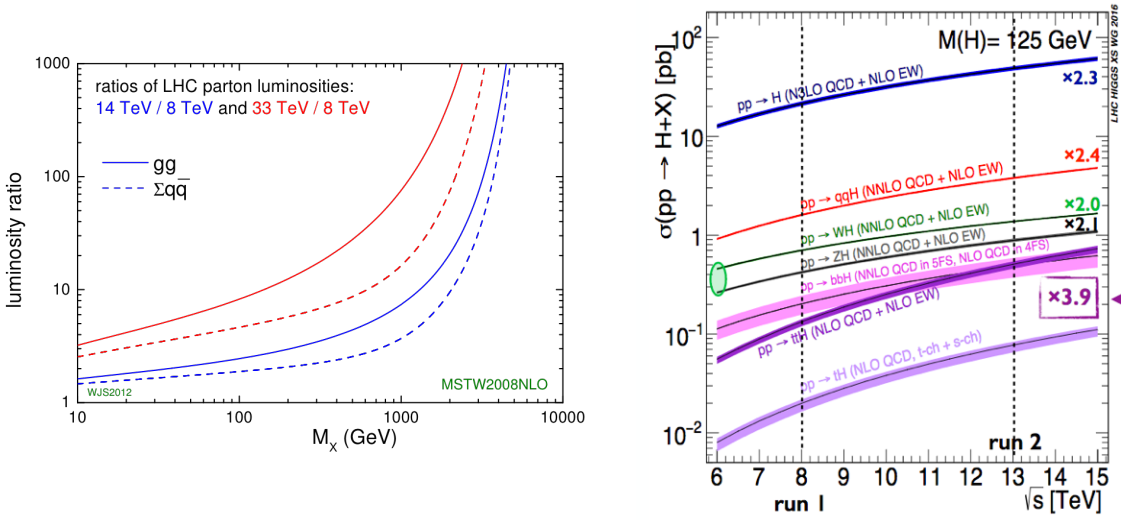

(a) (b)

FIGURE 4.1 – Relative increase of gg and $q\bar{q}$ luminosities with LHC energy increase [59] (left) and Higgs production mode cross sections as a function of the energy in the center of mass for proton-proton collisions.

Despite a cross section at the LHC two orders of magnitude smaller than the total Higgs boson production cross section ($\simeq$55 pb vs 0.5 pb), the distinctive signature from the top quarks in the final state gives access to many Higgs boson decay mode. Three types of final states are relevant to be experimentally studied.

- $t\bar{t}H$, $H \to b\bar{b}$. Its clear advantage is the high decay rate of the Higgs boson into $b\bar{b}$ compensating for the low production cross section of $t\bar{t}H$. Its drawback is an overwhelming systematic uncertainty from the very difficult and poor theoretical modelling of its irreducible $t\bar{t}b\bar{b}$ background. $t\bar{t}H \to b\bar{b}$ was the leading channel in sensitivity for run 1 integrated luminosities (up to $20 fb^{-1}$).
- $t\bar{t}H$, H $\to$ Multi-Leptons are $t\bar{t}H$ final states presenting two, three or four leptons (electrons, muons or taus). This includes contributions from the following Higgs decay : $H \to WW$, $H \to \tau\tau$ and $H \to ZZ$. Its main irreducible backgrounds, the $t\bar{t}V$ ($t\bar{t}W$ and $t\bar{t}Z$) processes being much better theoretically handled than $t\bar{t}b\bar{b}$. This array of final states has been the leading channel for the $t\bar{t}H$ 3σ evidence (36.1 fb^{-1} of 13 TeV data).
- $t\bar{t}H$, $H \to \gamma\gamma$. The $\gamma\gamma$ final state allows a high background rejection rate thanks to the high resolution of the invariant mass of the two photons. This channel has very low systematics but also a very low branching ratio. It has therefore become the dominant channel when more integrated luminosity has been recorded ($\geq 80 fb^{-1}$).

I decided to change final states with respect to my past involvement in $\gamma\gamma$ and get involved in the multilepton final state that sounded the most promising for Run 1 and Run 2 statistics of 20 to 140 fb^{-1}. Indeed for those integrated luminosities, $b\bar{b}$ would become too systematically

limited and $\gamma\gamma$ would not have yet quite enough statistics. But above all, multilepton channels are very rich and interesting final state to study and learn from, presenting all objects that can be reconstructed by the ATLAS detector. It has a high jet multiplicity (≥ 3), two b-tags, electrons, muons and taus, and even some missing transverse energy due to neutrinos from W leptonic decays, although not explicitly exploited in selection cuts.

My contribution was to develop and prove the $2\ell_{SS}+\tau_{\text{had}}$ channel was relevant. I optimised this analysis for Run 1 (20.3 fb^{-1} of 8 TeV data) [60], and Run 2 with ICHEP 2016 dataset : 13.2 fb^{-1} of 13 TeV data [61] and 36.1 fb^{-1} of 13 TeV data [62]. I now supervise a PhD student working on this channel development. The optimisation process of this channel will be described in section 5.

During Run 1 analysis, I was responsible for the combination of all multilepton final states, and the inclusion and correlation treatment of systematic uncertainties. I reshaped those results for $t\bar{t}H \rightarrow$ ML to contribute to the ATLAS Higgs boson global couplings combined measurement [63] and combination with CMS [64]. I re-interpreted $t\bar{t}H \rightarrow$ ML in the perspective of the search for the beyond standard model flavour-changing neutral currents analysis ($t \rightarrow qH$) [65]. As $t\bar{t}H \rightarrow$ ML coordinator and then HTop convenor during Run 2, I closely supervised a student and then a team of people responsible for this combination. The statistical combination of all multilepton channels, its interpretation in the overall Higgs couplings measurement combination, and its re-interpretations as a search are developed in sections 6.1 and 6.2.

During my mandate as HTop convener, in about a year, the $t\bar{t}H \rightarrow$ ML analysis has been drastically improved at every level. During run 1 [60] (20.3 fb^{-1} of 8 TeV data), and the first 13.2 fb^{-1} of 13 TeV data from run 2 [61], analyses were simple cut-and-counts using common objects selection working points described in section 5.1.4. Yet, in the process of being optimised in order to reach an evidence, every step of the process have been carefully scrutinised and upgraded. Additional final states with hadronic taus were considered, rising the number of independently optimised channels to seven, described in Section 5.1. Section 5.1.5 relates how the reducible backgrounds rejection factor has been boosted. Section 5.1.6 explains how multivariate analyses have been used to enhance the signal purity, and irreducible background control regions defined in the fit. Finally, data-driven reducible background estimates have moved from inclusive fake factor to Matrix Method or extended fake factor with event-by-event weight and been parameterised as a function of the variables they are most sensitive to. The data-driven estimates for the $2\ell 1\tau_{\text{had}}$ channel is described in section 5.3, and results shown in section 5.4.

5. $t\bar{t}H\rightarrow$ ML and $2\ell_{SS}+\tau_{\text{had}}$ channel

5.1 Map of the $t\bar{t}H \rightarrow$ ML final states

The analysis described here is its most recent public version, based on 36.1 fb^{-1} of 13 TeV data. Multilepton (ML) channels or final states are regions built as a function of the number of reconstructed and identified leptons. In this analysis, a distinction is made between electrons and muons, more easily identified in the detector and denominated as light leptons or just leptons, as opposed to hadronically decaying taus τ_{had}. $t\bar{t}H \rightarrow$ ML channels are defined by their **number of light leptons** ℓ and **hadronically decaying taus** τ_{had} as illustrated on Figure 5.1a. Channels are orthogonal by construction because exclusive in leptons multiplicity. Events with a given number of leptons and taus selected in one analysis are vetoed in the others. This absence of overlap is important for their statistical combination described in section 6.1.1. Multilepton channels pre-selection cuts are also designed to avoid any overlap with the other ATLAS Higgs searches in order to avoid all double counting of events which would cause statistical interpretations errors in the final combination couplings measurement. Depending on the version of public results, up to seven channels have been studied, sorted here by sensitivity. $2\ell_{SS}$: two tightly identified same-charge light leptons and no hadronic τ ; 3ℓ : three light leptons and no hadronic τ ; $2\ell_{SS}+\tau_{\text{had}}$: two same-charge light leptons and one hadronic τ ; $3\ell+1\tau_{\text{had}}$: three light leptons and one hadronic τ ; 4ℓ : four light leptons ; $1\ell+2\tau_{\text{had}}$: one light lepton and two opposite-charge hadronic τ ; and $2\ell_{\text{OS}}+1\tau_{\text{had}}$: two opposite-charge light leptons and one hadronic τ. The total number of expected signal events selected by all $t\bar{t}H \rightarrow$ ML channels in 36.1 fb^{-1} of 13 TeV data is 91 which corresponds to 0.50% of all produced $t\bar{t}H$ events.

In all channels, the multiple leptons requirement is useful to reject the otherwise overwhelming $t\bar{t}$ background. For a top quark mass of $m_t = 172.5$ GeV, $\sigma_{XS}(t\bar{t}) \simeq 832^{+20}_{-29}(\text{scale})\pm35(\text{pdf}+\alpha_s)\pm23(\text{if unfixed mass})$ pb, to be compared to σ_{XS} $(t\bar{t}H) \simeq 0.5$ pb at 13 TeV. Some channels like 3ℓ or 4ℓ present a lepton multiplicity superior to that of $t\bar{t}$. Channels requiring two light leptons, $2\ell_{SS}$ and $2\ell_{SS}+\tau_{\text{had}}$ request for the two leptons to be of same sign ($\ell^{\pm}\ell^{\pm}$) to reject the $\ell^{\pm}\ell^{\mp}$ signature from $t\bar{t}$. That induces a type of background called charge mis-identification, described in section 5.1.2, which arises from the wrong identification of lepton signs.

Final states with only light leptons accept signal in majority from the $H \rightarrow WW$ decay, while channels with hadronic taus also include a significant $H \rightarrow \tau\tau$ signal component, as illustrated on Figure 5.1b. In particular the $2\ell_{SS}+\tau_{\text{had}}$ channel has approximately 40% of Higgs bosons from $H \rightarrow WW$ decays and 60% of $H \rightarrow \tau\tau$. The $2\ell_{SS}$ signature for a signal event is formed by one light lepton coming from the Higgs boson decay ($H \rightarrow WW, W \rightarrow l\nu$ or $H \rightarrow \tau\tau, \tau \rightarrow l\nu_l\bar{\nu}_\tau$), and because of the same sign requirement, the other light lepton must come from the leptonic decay of one of the tops ($t \rightarrow Wb, W \rightarrow l\nu$), as illustrated on Figure 5.2a. To have a $2\ell_{SS}+\tau_{\text{had}}$ signature, a hadronic tau, essentially opposite sign to the lepton pair can arise either from one

of the remaining W from the top ($W \rightarrow \tau_h \nu$), or from the remaining tau or W from the Higgs boson decay as illustrated on Figure 5.2b.

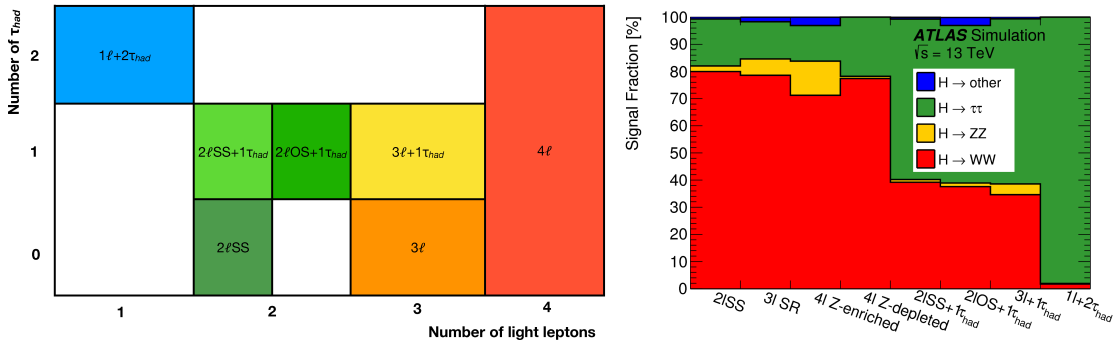

(a) (b)

FIGURE 5.1 – Multilepton channels map and Higgs decay composition [62].

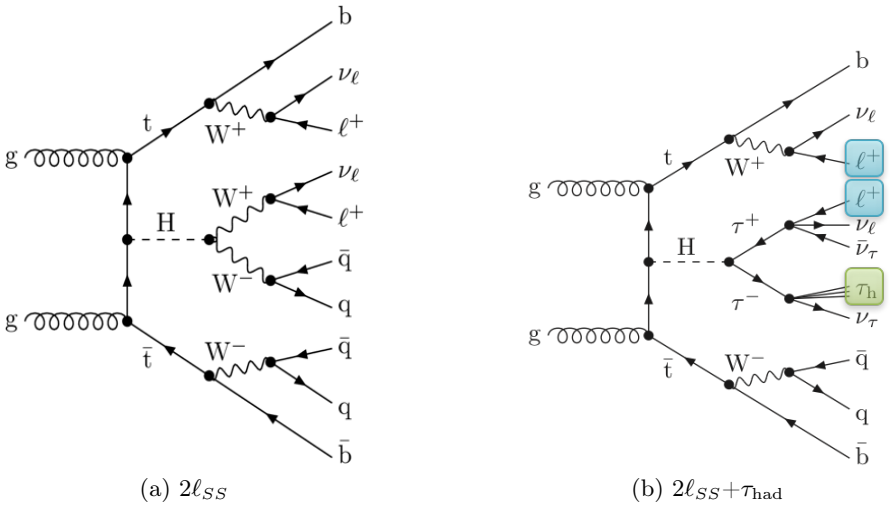

(a) $2\ell_{SS}$ (b) $2\ell_{SS}+\tau_{\text{had}}$

FIGURE 5.2 – $2\ell_{SS}+\tau_{\text{had}}$ and $2\ell_{SS}$ final states in $t\bar{t}H$ events.

5.1.1 Signal and background

5.1.2 Backgrounds

The main backgrounds for the search of $t\bar{t}H \rightarrow$ ML can arise from :

- $t\bar{t}V$ ($t\bar{t}W$, $t\bar{t}Z$). $t\bar{t}W$ or $t\bar{t}Z$ can present the same final state as the signal, modulo a lower jet multiplicity at tree level, as illustrated on Figure 5.3. $t\bar{t}V$ cross sections cross sections at NLO QCD+EW for 13 TeV collisions $\sigma_{t\bar{t}W} = 0.6$ pb $^{+12.9\%}_{-11.5\%}$(scale) $\pm 2.0\%$(pdf) $\pm 2.7\%(\alpha_s)$, $\sigma_{t\bar{t}Z} = 0.8$ pb $^{+9.6\%}_{-11.3\%}$(scale) $\pm 2.8\%$(pdf) $\pm 2.8\%(\alpha_s)$ namely the same level of magnitude as $\sigma_{t\bar{t}H} = 0.51$ pb $^{+5.8\%}_{-9.2\%}$(scale) $\pm 3\%$(pdf) $\pm 2\%(\alpha_s)$
- Non-prompt lepton reducible backgrounds. They arise mainly from the high cross section of the $t\bar{t}$ process ($\sigma_{t\bar{t}} = 832$ pb) where a lepton from a B-hadron decay is wrongly identified

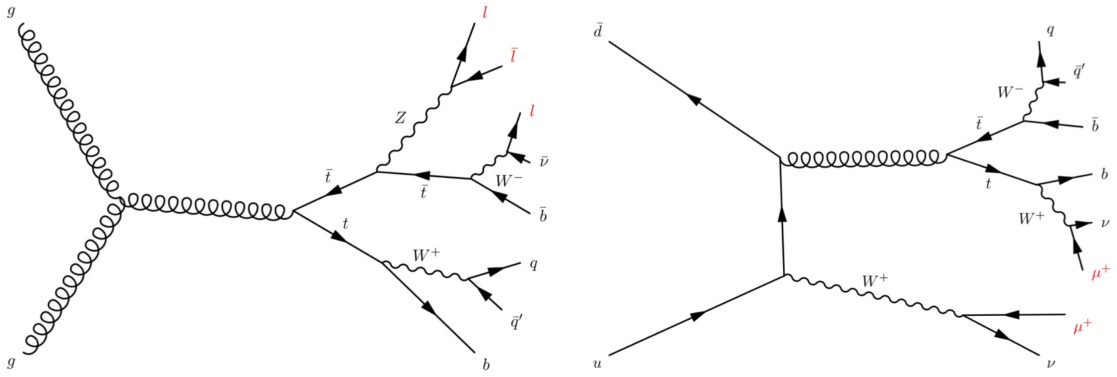

FIGURE 5.3 – $t\bar{t}Z$ (left) and $t\bar{t}W$ (right) processes with multileptonic final states.

as a prompt lepton. This type of background is often colloquially called *fake leptons*, or *heavy flavour fakes*.

↝ Fake taus reducible backgrounds that arise mainly from light jets mimicking the signature of a hadronic tau.

↝ Q-MisID, standing for charge mis-identification of a lepton. It is a reducible backgrounds resulting from a instrumental mis-interpretation of the final state where one of the lepton's charge sign is reconstructed as opposite to its truth sign. There are two main sources of electron charge mis-identification (Q Mis-ID) :

- ◇ Hard bremsstrahlung (γ taking most of the initial electron's energy and electron-positron pair production) producing trident electrons ($e^{\pm} \rightarrow e^{\pm} + \gamma^* \rightarrow e^{\pm}e^+e^-$), where the electron/positron's track from the conversion with opposite charge to the initial one is reconstructed, leading to a mis-identification of the charge. This source represents the main contribution to the Q Mis-ID background. The fraction of trident electrons and associated mis-identification rates depends on the amount of material that the electrons traverse and is therefore strongly $|\eta|$ dependent.
- ◇ A slightly curved track that induces a measurement error. Since the sign of charged particles is measured thanks to the bending of electron's trajectory in the magnetic field produced by the solenoid, this effect is more important for higher transverse momentum electrons that have straighter trajectories. Thus, a small dependence on electron p_T is also expected in the mis-identification rates.

For muons this background is negligible because as minimum ionising particles, hard bremsstrahlung are extremely rare, and secondly because muons tracks curvature sign can be reconstructed not only in the inner tracker, but also in the muons chambers.

The frequency of occurrence of this fake component is measured from data in $Z \rightarrow e^+e^-$ samples in bins of p_T and η. Charge mis-assignment rate varies from 5×10^{-5} for low-p_T electrons ($p_T \simeq 10$ GeV) at small $|\eta|$ to 10^{-2} for high-p_T electrons ($p_T \geq 100$ GeV) with $|\eta|>2$.

↝ Other backgrounds determined from MC include final states that are more easily discarded thanks to respectively the two jets and one b-tagged jet requirements (dibosons, VV→llXX) and a same-flavour opposite-sign leptons Z mass veto (Z→ l^+l^-+jets) ; or processes with

lower production cross section : tZ, tWZ, Wt, qqVV, VVV, three-tops and four-tops ($t\bar{t}t$, $t\bar{t}t\bar{t}$), $t\bar{t}W^+W^-$, single tops s-channel and t-channel.

5.1.3 Monte Carlo Setup

For this analysis, the Higgs boson mass is assumed to be 125 GeV, following the Run 1 combined ATLAS and CMS measurements [66]. The top quark mass is taken to be 172.5 GeV. The $t\bar{t}H$ signal, and irreducible $t\bar{t}W$ and $t\bar{t}Z$ are generated using the NLO generator MadGraph5 aMC@NLO [3] with Pythia 8 [67] for showering. The Parton Distribution Functions (PDFs) used are NNPDF 3.0 NLO [68] with the A14 [69] (ATLAS 2014) tune. MadGraph5 aMC@NLO [3] is a generator that computes the tree-level and next-to-leading order processes cross sections and their matching to parton shower simulations. Pythia [67] is a showering tool to model the evolution from a few-body hard generated process to the complex multi-hadronic final state. The MC generator tune refers to the chosen set of free parameters used in the optimisation process towards a reasonable description of measured observables in models that approximate high-multiplicity perturbative QCD calculations, or non-perturbative physics. Uncertainties on the $t\bar{t}H$ production cross section include QCD factorisation and renormalisation scales $(^{+5.8\%}_{-9.2\%})$ and PDFs and the strong coupling α_S ($\pm 3.6\%$), both described earlier in section 3.1.4.

The cross section for $t\bar{t}\ell^+\ell^-$, with $m(\ell^+\ell^-) > 5$ GeV, is 124 fb, and 601 fb for $t\bar{t}W$ [70]. The QCD scale uncertainties are $\pm 12\%$ and uncertainties from PDF and α_S variations are $\pm 4\%$. Events in the $t\bar{t}$ sample with radiated photons of high transverse momentum are vetoed to avoid overlap with those from the $t\bar{t}\gamma$ sample. Dedicated samples are included to account for backgrounds from $t\bar{t}Z/\gamma^*$where the Z/γ^* has low invariant mass but the leptons enter the analysis phase space via asymmetric internal conversions, or rare $t \rightarrow Wb\ell\ell$ radiative decays also called rare top decays.

5.1.4 Objects selection

Multilepton final states include all possible objects to be reconstructed in ATLAS. Their selection is detailed below.

↝ **Trigger**

All multilepton channels share the same trigger, based on the presence of a single or two light leptons, and a common set of of loose jet, lepton and event pre-selection. The trigger requirement for single lepton triggers is $p_T > 24$ (20) GeV for electron (muon) in 2015 and raised to 26 GeV for 2016 data. The di-electron threshold is 12+12 (17+17) GeV and the di-muon 8+8 (22+8) GeV in 2015 (2016). Electron+muon triggers p_T thresholds are 17+14 GeV for both datasets. The trigger efficiency ranges from 82% to 99% depending on the final state and dataset. The reconstructed light leptons are required to be trigger-matched. The primary vertex of an event is chosen as the vertex with the highest sum of squared transverse momenta of the associated tracks with $p_T > 400$ MeV.

↝ **Muon** candidates are reconstructed by combining inner detector tracks with track segments or full tracks in the muon spectrometer. They are requested to have $p_T > 10$ GeV and $|\eta| < 2.5$ and pass loose identification requirements [71]. To reduce the non-prompt muon contribution (see section 5.1.5), the track is required to originate from the pri-

mary vertex thanks to requirements on the track impact parameters [1] : $|d_0|/\sigma_{d_0} < 3$ and $|z_0|sin\theta$ <0.5 mm. To discard muons from hadron decays, muon candidates are also required to be separated by a variable distance of $\Delta R > min(0.4, 0.04 + (10GeV)/p_T, \mu)$ from any selected jets in order to optimise non-prompt rejection and prompt muons efficiency.

↝ **Electrons** are reconstructed from an electromagnetic cluster matched to a track in the inner detector. It is similar to that of converted photons detailed in section 2.1, at the exception of the requirement of one hit in the innermost pixel layer (called the insertable b-layer or IBL). The usual acceptance cuts are applied : $p_T > 10$ GeV, $|\eta_{cluster}|$<2.47 and crack removal (see section 2.3.2). The electron identification in ATLAS relies on a multivariate likelihood discriminant combining shower shape and track information. It is used to distinguish real prompt electrons from fake and non-prompt electron candidates from hadronic jets, photon conversions and heavy flavour (HF) from c and b hadron decays. Similarly as for the photon identification two working points are defined, *Loose* and *Tight*, depending on the prompt electron purity required [72, 73]. The preselection common to all multilepton final states and on which the channel categorisation is done relies on the Loose working point. The same longitudinal impact parameter cuts as for muons is applied, and the transverse cut is $|d_0|/\sigma_{d_0} < 5$. A selected electron is removed if within ΔR <0.1 of a selected muon.

↝ **Hadronically decaying tau leptons** τ_{had} are reconstructed from clusters in the calorimeters and associated tracks in the inner detector [74]. Candidates are required to have either one or three tracks, following the possible tau decay modes with one charge particle (≃85% of the time) or three charged particles (≃15%), and are subsequently called *one-prong* and *three-prong* tau candidates. The total charge of the tracks must be ±1. Kinematic cuts include $p_T > 25$ GeV and $|\eta| < 2.5$, and the calorimeter crack region removed.

A boosted decision tree (BDT) (see section 5.2) discriminant using calorimeter and tracking based variables is used to identify τ_{had} candidates and reject jet backgrounds. Three types of τ_{had} candidates are defined depending on the tightness on the BDT output, referred to as *loose*, *medium* and *tight* : the latter two are defined by working points with a combined reconstruction and identification efficiency of 55% and 45% (40% and 30%) for one (three)-prong τ_{had} decays, while the first one has a more relaxed selection and is only used for background estimates. The corresponding expected rejection factors against light quark and gluon jets vary from 30 for loose candidates to 300 for tight candidates. Tau reconstruction, identification and their performance are respectively described more thoroughly in References [74, 75]. Electrons that are reconstructed as one-prong τ_{had} candidates are removed via a BDT trained to reject electrons called the *electron veto*. Additionally, τ_{had} candidates are required to be separated by $\Delta R > 0.2$ from any selected electrons and muons to discard all tau leptonic decays $\tau \rightarrow \ell\nu_\ell\nu_\tau$. The contribution of fake τ_{had} from b-jets is removed by vetoing the candidates that are also b-tagged, which rejects a large fraction of the $t\bar{t}$ background. The contribution of fake τ_{had} from muons is removed by vetoing the candidates that overlap with low-p_T reconstructed muons. Finally, the vertex matched to the tracks of the τ_{had} candidate is required to be the primary vertex of the event, in order

1. The transverse impact parameter d_0 is the distance between the point of closest approach of a track and the primary vertex in the x,y plane (transverse to the beam direction). The longitudinal impact parameter z_0 is the z-coordinate of this point.

to reject fake candidates arising from pileup collisions.

⇝ **Jets** are reconstructed from three-dimensional topological clusters built from energy deposits in the calorimeters [76, 77], using the anti-k_T algorithm with a radius parameter R=0.4 [23] (see section 2.1). Their calibration is based on simulation with additional corrections obtained using in situ techniques [78] to account for differences between simulation and data, and result in the Jet Energy Scale set of systematic uncertainties.

⇝ **B-tagged jets**, simplified as *b-tags* or *b-jets* are jets that were tagged as being more likely to contain b-hadrons. B-hadrons decay through the weak interaction, they have therefore a sufficient lifetime to travel typically a few millimeters before their disintegration. They are identified, or b-tagged, via a multivariate discriminant combining information from algorithms using track impact parameters and secondary vertices reconstructed within the jet [79, 80].

The b-tagging weight is a relevant information to be used in multivariate analyses (see Section 5.2) but the whole discriminant shape cannot be properly calibrated, hence the scale factors are determined for only five working points : $\epsilon_{b-jet} > 85\%$, $77\% < \epsilon_{b-jet} < 85\%$, $70\% < \epsilon_{b-jet} < 77\%$ and $\epsilon_{b-jet} < 60\%$, determined as the b-jet average efficiency for jets containing b-hadrons with $p_T > 20$ GeV and $|\eta| < 2.5$ in $t\bar{t}$ events. The tighter the working point (WP), the purer the region and the smaller the efficiency. The use of several working points is called the pseudo-continuous b-tagging (PCB).

The working point used for this search corresponds to the 70% average b-jet efficiency for which the expected rejection factors against light-quark/gluon jets, c-quark jets and hadronically decaying τ leptons are respectively 380, 12 and 55 [79]. Scale factors are applied to the simulated samples to compensate for differences between data and simulation in the b-tagging efficiencies and mis-tagging rates [80].

⇝ **The missing transverse energy** E_T^{miss} is the norm of the negative vector sum of the transverse momenta of all identified and calibrated leptons and jets plus remaining unclustered energy estimated from low-p_T tracks associated with the primary vertex but not assigned to any lepton or jet candidate [81, 82].

5.1.5 Non-prompt and charge mis-identification reduction

Non-prompt leptons are all leptons that are not coming from the direct decay of W, Z, H and tau ; they are leptons coming from a hadron decay or from a photon conversion. Their reduction, and consequently the reduction of reducible backgrounds in the signal region of multilepton channels (see Section 5.1.2) is a key aspect of the analysis.

On top of the electron and muon selection described above, non-prompt leptons are further reduced thanks to a tool that was specifically developed and calibrated within the HTop group and called *Prompt Lepton Iso* (PLI). It consists in a Boosted Decision Tree (BDT) (see section 5.2) multivariate analysis. PLI was named in reference to the traditional ATLAS isolation (see Section 2.1), since the inputs variables include energy deposits and charged particle tracks in a cone around the lepton direction.

Since most non-prompt leptons are often originating from jets initiated by bottom or charm quarks, the most discriminating variables in the PLI are b-tagging algorithm outputs, together

with the angular distance between the lepton and the reconstructed jet, the calorimetric and track isolation variables of the lepton, the number of tracks within the jets and the ratio of the lepton and jet p_T. The training is performed separately for electrons and muons on prompt and non-prompt leptons from $t\bar{t}$ simulation. A working point was chosen with an efficiency of 70% for muons and 60% for electrons for p_T 10 GeV and reaches a plateau of 98% (96%) at p_T 45 GeV, as shown in Figure 5.4. The rejection factor against leptons from the decay of b-hadrons is about 20. Data-to-simulation efficiency ratios (Scale Factors) for PLI as well as trigger, reconstruction and identification are determined with a tag-and-probe method.

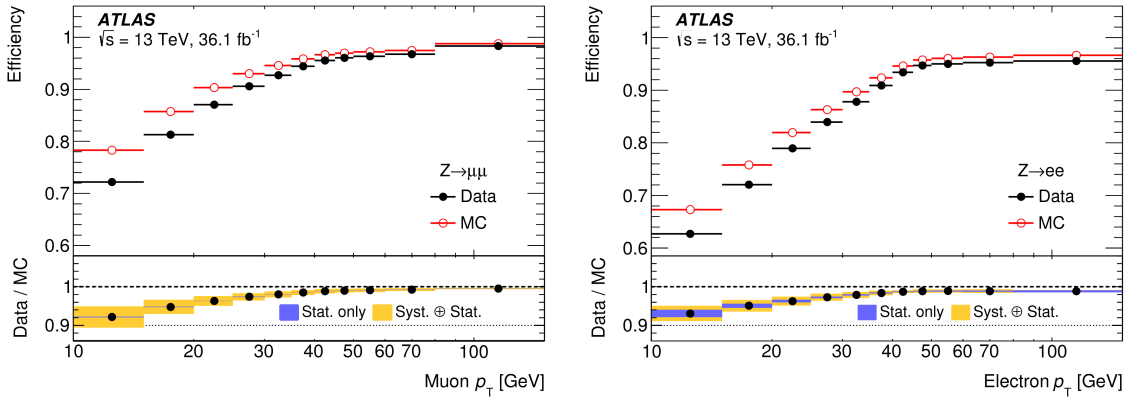

FIGURE 5.4 – Prompt Lepton Isolation (PLI) BDT chosen working point efficiency on identified prompt muons (left) and electrons (right) as a function of the lepton p_T. Muons are required to pass the loose identification requirements, while electrons are required to pass the tight identification requirements. The measurements in data (simulation) are shown as full black (open red) circles. The bottom panel displays the ratio of data to simulation results, with the blue (yellow) band representing the statistical (total) uncertainty. This ratio is the scale factor that is applied to correct the simulation [62].

In order to reduce the amount of wrongly identified charge for the selected electrons, a BDT discriminant called Charge Flip Killer is built using electron cluster and track properties as input : the electron's transverse momentum and pseudo-rapidity, the track curvature significance (defined as the ratio of the electric charge to the track momentum divided by the estimated uncertainty in the measurement) and its transverse impact parameter times the electric charge, the cluster width along the azimuthal direction, and the quality of the matching between the track and the cluster, in terms of both energy/momentum and azimuthal position. The chosen working point achieves a rejection factor of $\simeq$17 for tightly identified electrons with wrong charge assignment and provides an efficiency of 95% for electrons with correct charge reconstruction.

5.1.6 Multilepton channels definitions

The event selection and signal extraction for each of the multilepton channels is :

- $2\ell_{SS}$ requires two tightly identified same-charge light leptons with $p_T > 20$ GeV and no hadronic τ. Four jets are required to reduce $t\bar{t}$ and $t\bar{t}W$ backgrounds, and at least one or two of them must be b-tagged.

$\rightsquigarrow$ 3ℓ requires three light leptons and no hadronic τ. The sum of charge of the three leptons must be ± 1. The lepton with opposite charge to the other two is almost always prompt in $t\bar{t}$ events (97% of cases) which allows to increase acceptance by requiring only a loose selection described in section 5.1.4. The other two are tight with $p_T > 15$ GeV. Same-flavour opposite-charge lepton pair with an invariant mass below 12 GeV are removed to suppress background from resonances that decay to light lepton pair. Events containing a same-flavour opposite-charge (OSSF) lepton pair with an invariant mass within 10 GeV of the Z boson mass are removed (Z-veto) to suppress the $t\bar{t}Z$ background. Finally, to eliminate potential backgrounds with Z decays to $\gamma^{(*)} \rightarrow \ell\ell\gamma^* \rightarrow \ell\ell\ell'\ell'$, where one lepton has very low momentum and is not reconstructed, the three-lepton invariant mass must satisfy |m(3ℓ)-91.2 GeV| >10 GeV.

$\rightsquigarrow$ $2\ell_{SS}+\tau_{\text{had}}$ two same-charge light leptons and one hadronic τ. This is the channel I have been involved in : why and how is described in section 5.2.

$\rightsquigarrow$ $3\ell+1\tau_{\text{had}}$ three light leptons and one hadronic τ. The requirements on the three light leptons follow that of the 3ℓ channel, except that the two same-charge leptons must be tight with $p_T>$ 10 GeV and the opposite charge lepton must be loosely identified and isolated. The reconstructed hadronic tau must be of opposite charge to the total charge of the light leptons.

$\rightsquigarrow$ 4ℓ four light leptons. This channel is very pure but has very low statistics.

Exactly four leptons with a null total charge are required. Only the third and fourth leptons ordered by decreasing p_T are tightly identified to reject the non-prompt contribution. No requirement is made on the number of selected hadronic taus. The same Z-veto as for the 3ℓ channel is applied to suppress the $t\bar{t}Z$ contribution. Same-flavour opposite-charge lepton pairs with invariant mass below 12 GeV are removed to suppress background due to resonance decaying to light leptons. To ensure orthogonality with the $H \rightarrow ZZ$ dedicated channel [83] towards general Higgs couplings combination, a Higgs to four leptons mass veto is applied |m(4ℓ)-125GeV|>5 GeV.

$\rightsquigarrow$ $1\ell+2\tau_{\text{had}}$ one light lepton and two opposite-charge hadronic τ. Selected events are required to present at least one tight lepton and exactly two medium identified tau candidates of opposite charge, with at least one of them tight. In order to suppress the $t\bar{t}$ background, events must have at least three jets.

$\rightsquigarrow$ $2\ell_{\text{OS}}+1\tau_{\text{had}}$ two opposite-charge light leptons and one hadronic τ. Selected events have exactly two loose and isolated leptons of opposite charge and exactly one medium identified hadronic tau candidate. A minimum of three jets requirements is used to reject $t\bar{t}$, Z+jets and $t\bar{t}V$ backgrounds. A Z-veto applied to same-flavour leptons pairs rejects the Z+jets background with a fake tau. To suppress background from resonances that decay to light leptons, events containing a same-flavour lepton pair with an invariant mass below 12 GeV are also removed.

The background composition and signal purity for all considered regions are shown on Figure 5.5.

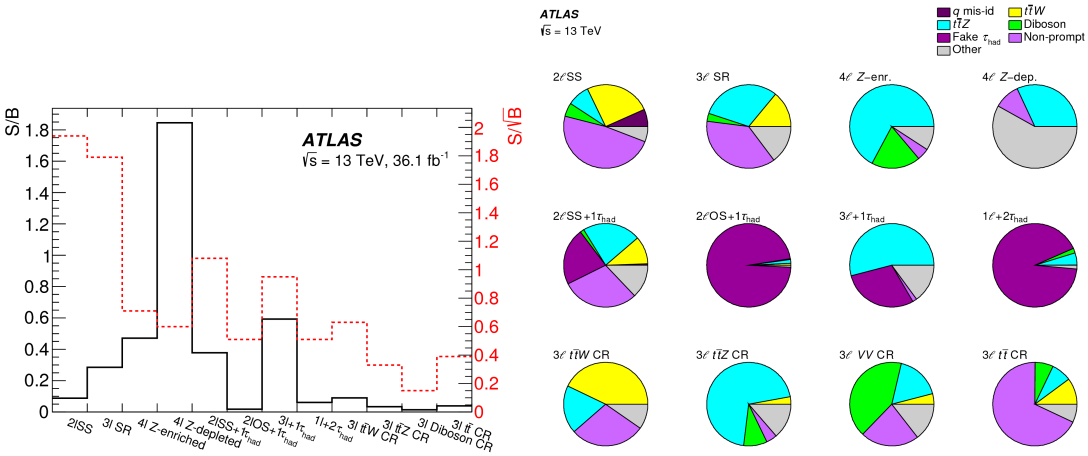

FIGURE 5.5 – Multilepton channels purity, $S/\sqrt{B}$ significance (left) and background composition (right) [62].

5.2 Optimisation of the $2\ell_{SS}+\tau_{\text{had}}$ channel

5.2.1 Signal region selection

I joined the $t\bar{t}H \rightarrow$ ML team right after the run 1 analysis kick-off meeting in June 2013. At that time, only the $2\ell_{SS}$, 3ℓ and 4ℓ final states with electrons and muons were considered. As a first step into the team, I checked whether optimising categories with hadronically decaying taus was relevant, starting with the $2\ell_{SS}$ final state, that would later on be followed by many other channels involving hadronic taus ($1\ell 2\tau_{\text{had}}$, $2\ell_{OS}\tau_{\text{had}}$, $3\ell 1\tau_{\text{had}}$, maybe even $2\ell 2\tau_{\text{had}}$ has proven to be worth considering in the future). The combined significance of $2\ell 1\tau_{\text{had}}$ and $2\ell_{SS}0\tau_{\text{had}}$, since τ_{had} had to be vetoed in the latter category, was surpassing the significance of an inclusive 2lSS channel. That was the start of my involvement in the $t\bar{t}H \rightarrow$ ML team that was then followed by working on combining all final states as described in section 6.

I participated to three different published versions of the $2\ell_{SS}+\tau_{\text{had}}$ channel. The first draft of the analysis was important to define its main cut-and-count features, that were found later on to remain optimal for run 2 update. These features include :

- ⇝ Two same sign leptons, to reduce the otherwise overwhelming opposite sign leptons from the $t\bar{t}$ background. Same sign leptons can arise from one lepton coming from the top decay and another one from the Higgs boson decay (see Figure 5.2b). These leptons are additionally prefered to be identified with the tighest working point to reject background arising from b-jets faking leptons.
- ⇝ One hadronic tau is required, with a medium identification, which optimises the $2\ell_{SS}+\tau_{\text{had}}$ channel sensitivity. In order to ensure channels orthogonality for the $t\bar{t}H \rightarrow$ ML combination, the $2\ell_{SS}$ channel vetoes events with a medium tau but accept events with looser taus, that are not considered as taus in the ML analysis. Any event with two tight light lepton is therefore either entering the $2\ell_{SS}$ or the $2\ell_{SS}+\tau_{\text{had}}$ channel. In order to optimise the tau identification working point, the sensitivity estimate was checked jointly on $2\ell_{SS}$ and $2\ell_{SS}+\tau_{\text{had}}$ channels, which still concluded to an optimal medium hadronic tau selection.
- ⇝ $N_{jets} \geq 4$. The signal purity in the signal region was found to be optimal for selected events

with at least 4 jets.

↝ Tau opposite sign to the leptons In signal events, the tau can come from the top that did not generate one of the leptons or from the Higgs (see Figure 5.2b). Its sign has to be opposite to that of the lepton pair. It is therefore required for the tau to be opposite sign to the lepton pair, which is cutting background arising from light jets faking taus with no favoured sign.

↝ A Z-mass veto $|m(ee)-91.2GeV| > 10GeV$ is applied on di-electron events to reject Z+jets background where one of the electron's charge is wrongly reconstructed.

These features used for the run 1 analysis [60] were regularly tested for each analysis update, found to remain optimal and kept, for the run 2 analysis made with 13.2 fb^{-1} of 13 TeV data [61], and the run 2 paper with 36.1 fb^{-1} of 13 TeV data.

5.2.2 Multi-variate analysis

In this last analysis, also used for the evidence and observation of the ttH production mode, the analysis with an inclusive region (so called *1-bin* analysis) was however improved thanks to a Multi-Variate Analysis (MVA), also known as machine learning techniques. For structured data analysis, the optimisation consists in making use of supervised learning, where the algorithm is trained to recognise features, knowing the truth (typically from Monte Carlo simulation where the truth is stored), then tested on another independent set of MC (typically the other half of the previously split-in-two MC sample), and finally applied on data to derive results.

An important part of MVA analyses validation is to avoid over-training, the interpretation by the algorithm as real physics processes features of effects that are actually due to the limited available Monte Carlo statistics. To do so, an additional method called n-fold cross validation is done by splitting the available MC statistics into n folds, training on one of them and testing on all the remaining folds. In the $2\ell_{SS}+\tau_{\text{had}}$ analysis, a 2-fold cross validation was performed : the MVA was trained on even-numbered events and tested on odd-numbered MC events.

While Neural Networks are widely used for pictures analysis, one of the most efficient supervised machine learning algorithm for structured data are decision trees. The analysis purpose being to separate signal from background, classification [2] trees sorting events into those two labelled classes are used.

The decision tree algorithm is a is a recursive partitioning which separates events into two nodes : one passing the criteria and one failing it. At each node, the criteria is a cut on the discriminating variable that achieves the best separation, based on a quantification of the probability to obtain misclassified events. The default criteria is the Gini index defined as $p(1-p) = \frac{sb}{(s+b)^2}$ where p is the purity of signal (and therefore 1-p the purity of background). The worst possible separation comes with a purity of $\frac{1}{2}$ and Gini of 0.25, and gets better as it approaches 0. As a consequence, out of the two resulting nodes, one contains mostly signal events and the other mostly background events. The process is repeated on each resulting node and ends when there is insufficient improvement from further splitting [3], at which point events end up in leaves. The individual decision tree output is a weight of ± 1. Events in leaves where the purity ($\frac{s}{s+b}$) is above 50% are given the weight $+1$ and events in background enriched leaves are given a -1 weight.

2. Other trees exist, called regression trees, where the outcome is the estimate of a target numeric value (reconstructed energy for instance).

3. or the minimal minimum leaf size is reached, or perfect classification is achieved (not likely for our analyses) or the maximal tree depth is reached

A boosting procedure is then applied, which consists in applying a function giving a higher weight to mis-classified events and rebuilding a decision tree. This effectively results in a forest of decision trees. Depending on the function applied the boosting procedure is called adaptive or gradient, the latter being used for our case. Boosting stabilises the response of the decision trees with respect to fluctuations in the training sample and is able to considerably enhance the performance with respect to a single tree. The final Boosted Decision Tree (BDT) is the weighted average of individual decision trees outputs. In effect, the BDT attributes a real number between 0 and 1 to each event, signal-like (background-like) events having a BDT close to 1 (0).

Decision trees can be sensitive to a number of parameters that are carefully chosen and optimised by the user such as the number of input variables, the number of trees in the forest, the depth of the tree, etc. The choice of variables to use prioritarily in the decision trees rely on the ranking of their discriminating power as measured in terms of separation :

$$\langle S^2 \rangle = \frac{1}{2} \int \frac{(f_S(x) - f_B(x))^2}{f_S(x) + f_B(x)} dx \tag{5.1}$$

where f_S and f_B are respectively the signal and background PDFs of x. The separation is therefore zero for identical signal and background shapes, and it is one for shapes with no overlap and quantifies the discriminating power of reconstructed variables. The set of variables is optimised by choosing subsets of the most highly ranked according to their separation or discriminating power. The BDT algorithm used is coded by TMVA package [84], with the benefit of a simple interface, and is demonstrated by machine learning experts from the collaboration as having similar performance as the new and trendier XGBoost package, otherwise used in the ML analyses.

The final $2\ell_{SS}+\tau_{\text{had}}$ BDT is using 13 variables and trained in a region with loose leptons and lower jet multiplicity ($N_{jets} \geq 2$) to reject $t\bar{t}$ background enriched in reducible $t\bar{t}$ events. The variables used in the BDT are related to :

- **lepton properties** : second leading lepton p_T, second leading lepton track isolation, the maximum $|\eta|$ of both leptons
- **jet properties** : number of jets, number of b-tagged jets, second leading jet p_T, scalar sum H_T of all jets p_T, b-tagging weight of second and third leading jets, pseudo-rapidity of fourth leading jet
- **tau properties** : invariant mass between the hadronic tau and the furthest lepton
- **angular variables** : ΔR between the leading lepton and the leading jet and ΔR between the two leading jets

After being trained on the relaxed region to enhance statistics, the BDT is only applied to events in the SR described in section 5.2.1.

Considering $2\ell_{SS}+\tau_{\text{had}}$ is still a rather low statistics channel, the BDT shape used as input to the fit was chosen to have only two bins, as illustrated on Figure 5.8a. Consequently to what was explained above on the construction of the BDT output, events with a BDT score close to 1 are signal-like events while the left-most category is enriched in background.

In the analysis leading to the evidence, a simpler cut-and-count categorisation was developed for $2\ell_{SS}+\tau_{\text{had}}$ as well as for the other two most sensitive channels $2\ell_{SS}$ and 3ℓ. This provided an independent cross-check of the multi-variate analysis, with comparable sensitivity. In the $2\ell_{SS}+\tau_{\text{had}}$ analysis, three categories are built relying on the maximum $|\eta|$ of the two light leptons, and the p_T of the subleading jet.

5.3 Non-prompt leptons estimate $2\ell_{SS}+\tau_{\text{had}}$ channel

The most abundant source of reducible background arising from jets wrongly identified as leptons is the $t\bar{t}$ process. The $2\ell_{SS}+\tau_{\text{had}}$ channel is the only ML channel that has significant contributions from both non-prompt light leptons (fake electrons and muons), and non-prompt hadronic taus. Data-driven methods are used to estimate backgrounds arising from both.

Non-prompt tau events are majoritarily arising from light jets as shown on Figure 5.7. Non-prompt leptons come however mostly from heavy flavour jets, and data-driven fake estimates methods are built to estimate that source of fakes, even if photon conversion's importance is growing as will be developed in the section dedicated to the future plans in $t\bar{t}H$ 7.1.

There are two ways a $t\bar{t}$ event can enter the $2\ell_{SS}+\tau_{\text{had}}$ signal region. In all of the cases, $t\bar{t}$ provides at least one prompt lepton, and in all cases one b-jet from one of the top decays fakes the same sign light lepton, which is the only way a $t\bar{t}$ event can enter the same sign lepton signal region. If there is no true τ_{had}, as illustrated in Figure 5.6a, and a light jet fakes a hadronic tau. That happens in 70% of the cases. In the other 30% of events, the hadronic tau is prompt from one of the W decays as shown on Figure 5.6b.

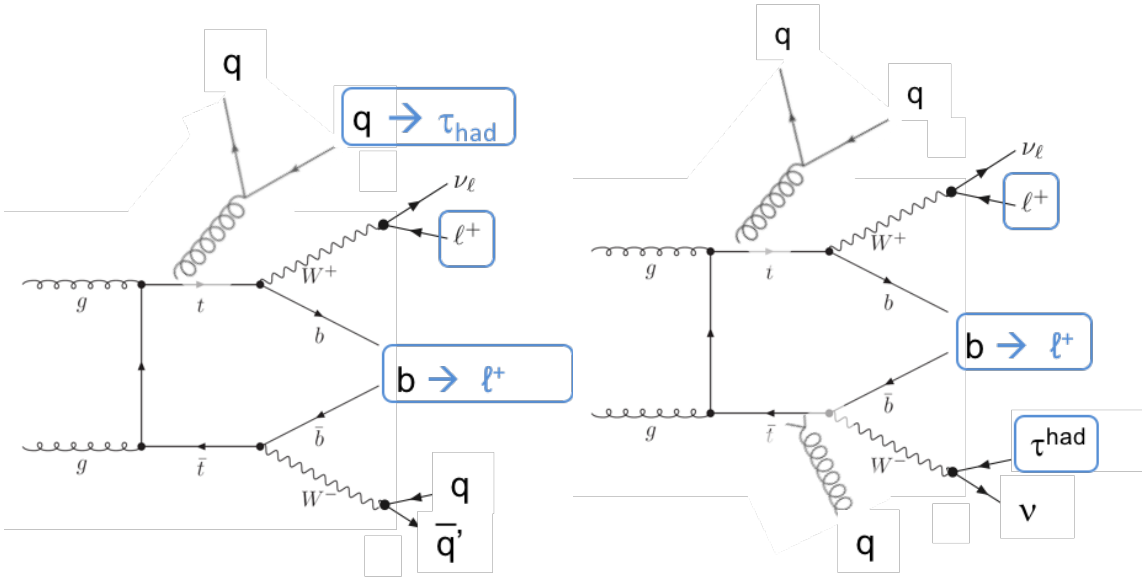

(a) $t\bar{t}$ with fake τ and fake lepton (70%) (b) $t\bar{t}$ with true τ and fake lepton (30%)

FIGURE 5.6 – Illustration of how a $t\bar{t}$ event can enter the $2\ell_{SS}+\tau_{\text{had}}$ signal region with both a light jet faking a τ_{had} and a b-jet faking a light lepton (70% of the $t\bar{t}$ selected events) or with a true hadronic tau and a fake light lepton (30%).

Non prompt tau events scale factors are derived in a $2\ell_{\text{OS}}+1\tau_{\text{had}}$ control region, enriched in fake τ_{had}. They are defined as the ratio of the number of fake τ_{had} data over those predicted by simulation. This scale factor is then applied in the $2\ell_{SS}+\tau_{\text{had}}$ and $3\ell+1\tau_{\text{had}}$ signal regions, which is made possible from the fact the origin of the fake τ_{had} is similar across all of these regions (Figure 5.7). Its dependence on p_T was found to be negligible. Uncertainties in this scale factor are derived by comparing the value in the nominal control region to those obtained in control regions enriched in $t\bar{t}$ and Z boson events, varying the relative abundance of each source of fakes.

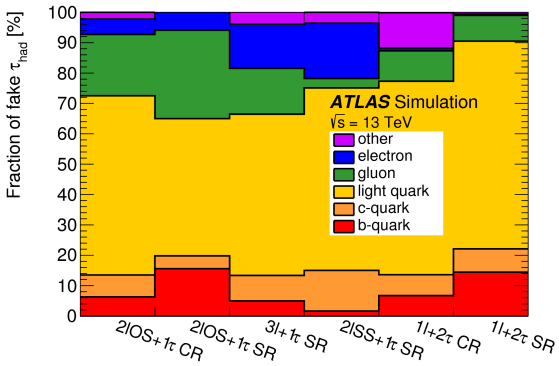

FIGURE 5.7 – Origin of non-prompt hadronic taus in various signal and control regions [62].

The final scale factor is 1.36 ± 0.16 including statistical and systematic uncertainties.

In the $2\ell_{SS}+\tau_{\text{had}}$ channel, the scale factor is applied only to backgrounds containing prompt leptons and MC-truth-identified fake τ_{had} candidates. An additional fake factor method is used to estimate the background from events containing non-prompt light leptons.

The **non-prompt leptons** background estimate is using a fake factor method, also called ABCD method, where A is the signal region, B a region where one of the leptons has relaxed ID, C, a region where the jet multiplicity is lowered to 2 and 3, and D has both relaxed criteria. This method, simpler but very similar to the Matrix Method used in $2\ell_{SS}$ and 3ℓ, relies on the assumption that lepton ID is uncorrelated with the jet multiplicity. The data-driven fake estimate in the SR A is taken from the number of data events in regions B, C, and D : $N_A = \frac{N_B \times N_C}{N_D}$. The signal $t\bar{t}H$ and prompt backgrounds contribution, in particular $t\bar{t}V$, is subtracted from all the regions and their normalisation and uncertainty are fully correlated with the rest of the analysis for combination. When the analysis was a simple cut-and-count, the inclusive number quoted above was enough. A p_T parameterisation was then included to account for shape effects when the BDT was introduced. As in the $2\ell_{SS}$ and 3ℓ non-prompt lepton estimates, the change in the fraction of conversions from the control to the signal region is taken into account, with the same associated uncertainties. The total systematic uncertainty in the non-prompt lepton estimate in this channel is 55%, dominated by the statistical uncertainty in the closure test of the method found in simulation.

Overall across various channels, data-driven methods estimate a factor two more non-prompt background than MC predicts.

5.4 Results for the $2\ell_{SS}+\tau_{\text{had}}$ channel

Results for the successive versions of the analysis are given in figure 5.8. Top plots show results for the Run 1 analysis with 20.3 fb^{-1} of 8 TeV data [60]. One data event was observed for an expected number of background events of 1.4±0.6 and signal event of 0.47±0.08. An event display for this single Run 1 event is available in Appendix A. The fitted signal strength back then was therefore negative $\mu = -0.9^{+3.1}_{-2.0}$.

Middle plots from figure 5.8 show the results for Run 2 with 13.2 fb^{-1} of 13 TeV data [61]. Due to a combined effect of the increase of energy in the center of mass, and an observed excess, this time 14 data events were observed for 4.8 ± 1.4 background and 1.43 ± 0.31 signal events

expected, resulting in a best value of $\mu = 6.2^{+3.6}_{-2.7}$. The event display from one of these events is available in Figure A.2 in Appendix A.

Finally, bottom plots from figure 5.8 provide the update with 36.1 fb^{-1} of 13 TeV data, where the simple cut-and-count was turned into a BDT analysis (Figure 5.8a) with a categorisation backup (Figure 5.8c) [62]. The observed number of data events is 18 for 8.2±1.6 expected background and 3.09±0.46 signal events. The best fit value for the standalone channel is the highest of all $t\bar{t}H \rightarrow$ ML results with a $\mu = 3.5^{+1.7}_{-1.3}$, that translates into an observed significance of 3.4σ (1.1σ expected).

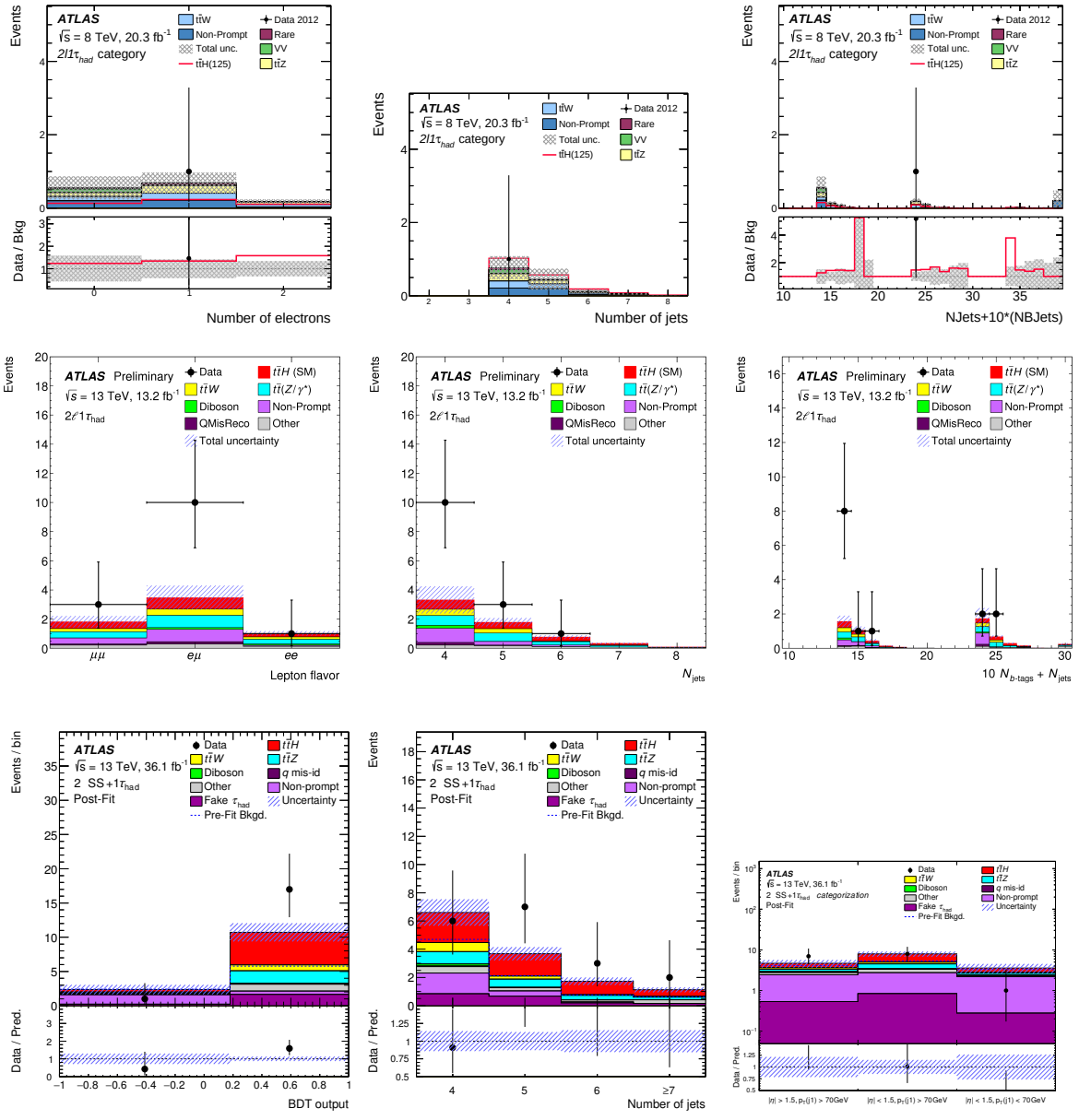

(a) BDT Output (b) N_{jets} (c) Cross check categorisation

FIGURE 5.8 – Successive published results of $2\ell_{SS}+\tau_{\text{had}}$ channel for 20.3 fb^{-1} of 8 TeV data on top (Run 1) [60], 13.2 fb^{-1} of 13 TeV data for middle plots [61], and 36.1 fb^{-1} of 13 TeV data for bottom plots (Run 2) [62].

6. $t\bar{t}H$ → ML combination, couplings and re-interpretation

This chapter relates my involvement in statistical interpretations of the $t\bar{t}H \rightarrow$ ML analyses. I pursued statistical combination of all multilepton final states, its adaptation for the overall ATLAS and ATLAS-CMS Higgs boson couplings measurement, and re-interpretation into the beyond standard model search for flavour changing neutral currents. Across the years my responsibility in statistical interpretations evolved from being the main developer, to student close supervisor, to finally coordinate a whole combination team. For pertinence sake, only the most recent run 2 results at the time of the redaction of this manuscript will be detailed (see the datasets description in Table 1.1).

The layout of this chapter is the following. Section 6.1 is devoted to the measurement of the Higgs boson's couplings to other particles. Section 6.1.1 is a description of the $t\bar{t}H \rightarrow$ ML combination method and results, section 6.1.3 focuses on the physics related to the Higgs produced in association with a single top. Section 6.1.2 and section 6.1.4 respectively describe statistical combination with all the other $t\bar{t}H$ decay modes, and with all the other Higgs boson production and decays. Finally, my participation to the re-interpretation of the $t\bar{t}H \rightarrow$ ML result into the search for flavour changing neutral currents will be reported in section 6.2.

6.1 Measurement of the Higgs boson's couplings

6.1.1 $t\bar{t}H \rightarrow$ ML combination

6.1.1.1 $t\bar{t}H \rightarrow$ ML fit regions

During run 1 analysis, the $t\bar{t}H \rightarrow$ ML combination included five final states, as illustrated on Figure 6.1 [60]. Each of these channels were optimised as cut-and-count analyses with only one bin contributing to the simultaneous maximum likelihood fit, at the exception of the 4ℓ channel further split into an ultra-pure and a "rest" category. This first multilepton analysis resulted into an intriguing signal strength measurement of twice the expected standard model value, although very compatible with the SM hypothesis : $\mu = 2.1^{+1.4}_{-1.2}$, as shown on Figure 6.1 left [60]. Interestingly enough, $t\bar{t}H \rightarrow \gamma\gamma$ ($\mu = 1.3^{+2.62}_{-1.75}$) and $t\bar{t}H \rightarrow b\bar{b}$ ($\mu = 1.5^{+1.1}_{-1.1}$) also fitted higher than standard model values [63]. Even more interestingly, CMS was getting $\mu_{ttH} = 2.9 \pm 1.0$ for their corresponding dataset, resulting in a combined LHC measurement of $\mu_{ttH} = 2.3^{+0.7}_{-0.6}$ as shown on Figure 6.1 right [64].

Run 2 analyses have been greatly optimised with respect to the first run 1 measurement. For starters, the number of investigated final states went from five to seven. Most of the channels

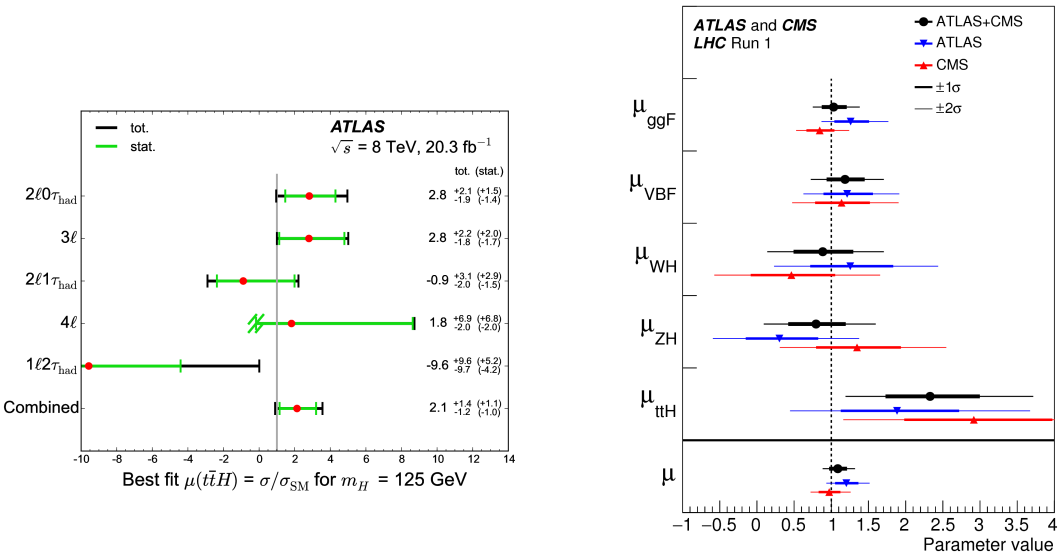

FIGURE 6.1 – Left : Run 1 $t\bar{t}H \rightarrow$ ML best fitted signal strength for the five considered channels and their combination [60]. For the 4ℓ Z-depleted category, $\mu <$ -0.17 results in a negative expected total yield and therefore the lower uncertainty is truncated at this point. Right : Best fit results for the production signal strengths for the combination of ATLAS and CMS Run 1 data [64].

now resort to the usage of BDT output as final discriminant instead of a simple event counting. Some final states also include control regions and/or several categories. While the analyses pre-selections were described in section 5.1.6, the analyses strategies, sensitivity optimisation and the choice of the number of simultaneously fitted categories is as follows :

- $2\ell_{SS}$: its discriminating variable, shown in Figure 6.2a, is the average of two boosted decision trees, targeting respectively at rejecting reducible ($t\bar{t}H$-vs-$t\bar{t}$, actually $t\bar{t}H$-vs-data-driven-non-prompt-leptons) and irreducible ($t\bar{t}H$-vs-$t\bar{t}V$) backgrounds.
- 3ℓ : the analysis strategy results from the optimisation of a five-dimensional multinomial BDT, also called multi-class BDT which simultaneously defines a signal enriched region and four control regions enriched in $t\bar{t}W$, $t\bar{t}Z$, $t\bar{t}$ and diboson. All of five of them, the signal region and four control regions, are used in the fit to exploit the background normalisation constrain they provide. The BDT is trained using the input from 28 topological variables. The $t\bar{t}H$ output provides the final discriminant used in the signal region, as showed on Figure 6.2b.
- $2\ell_{SS}+\tau_{had}$: the channel optimisation, which final BDT discriminant is shown on Figure 5.8a, is described in details in section 5.2.
- $3\ell+1\tau_{had}$: due to the relatively high purity and low statistics of this channel, a simple event yield illustrated on Figure 6.2c is used in the fit, following the selection described in section 5.1.6.
- 4ℓ : the signal region described in section 5.1.6 is further split into two categories : Z-enriched and Z-depleted, respectively defined as the regions where events have at least one same-flavour opposite charge lepton pair, or none at all. While the Z-depleted category is very

pure (S/B $\simeq$ 1.8), a BDT is used in the Z-enriched category (S/B $\simeq$ 0.5) to discriminate against the dominant $t\bar{t}Z$ background. The BDT uses kinematic variables as well as a pseudo-matrix element discriminator to partially reconstruct top quarks, Higgs boson and Z boson resonances. A cut is then applied on the BDT discriminant to define the Z-enriched signal region. In the end, the Z-depleted (Figure 6.2d) and Z-enriched (Figure 6.2e) regions are counting categories.

- 1ℓ+$2\tau_{\text{had}}$: a BDT is trained to reject $t\bar{t}$ events which represent a large majority of the background when having one or two fake taus. Seven variables are used in the training to build the final discriminant (Figure 6.2f) and in particular the invariant mass of the visible decay product of the $\tau_{had}\tau_{had}$ system.
- $2\ell_{\text{OS}}$+$1\tau_{\text{had}}$: previously a channel with rather low sensitivity, the $2\ell_{\text{OS}}$+$1\tau_{\text{had}}$ channel became a control region dedicated to the measurement of the scale factor between data and MC efficiency for non prompt tau (tau fakes). A BDT (Figure 6.2g) is trained with six discriminating variables to reduce $t\bar{t}$ events with a fake hadronic tau candidate.

The twelve categories, of which eight signal regions and four background-enriched control regions are fitted simultaneously, setting the parameter of interest as the signal strength $\mu_{t\bar{t}H}$ defined as in equation 3.4, which is a free parameter fully correlated across all channels. The post-fit numbers of expected signal and background in each category are presented on Figure 6.3.

6.1.1.2 $t\bar{t}H \rightarrow$ ML systematics correlation scheme

One key point to combining channels is the choice of the correlation scheme of all nuisance parameters, or systematic uncertainties, detailed in Table 6.1. More details about the definition and treatment of them in the likelihood fit are provided in Section 3.1.5. The sources of uncertainty sorted by their importance as a function of their impact on the error on the fitted signal strength μ is shown on Figure 6.4. There are three main sources of systematics in the analysis.

- One is the theory modelling of the $t\bar{t}H$ signal and irreducible backgrounds, mainly $t\bar{t}V$. They include the uncertainties on cross sections, Higgs boson branching fraction for $t\bar{t}H$, as well as the usual renormalisation and factorisation scale, also called QCD scale uncertainties, parton shower and hadronisation model, or PDF+α_s , both described earlier in section 3.1.4. Finally an uncertainty is applied to the shower tune used to model the parton shower, hadronisation and underlying events. As illustrated on Figure 6.4, theory related systematics entering the top fifteen systematics are all related to $t\bar{t}H$, $t\bar{t}W$ and $t\bar{t}Z$ processes.

  All theory systematics are fully correlated across channels.
- A second type of systematic uncertainties arises from instrumental effects. They include the LHC luminosity measurement ($\pm$ 2.1% for 2015 and 2016 combined, see section 1.2.2) and the pile-up reweighing applied to MC in order to make the distribution of number of interactions per bunch crossing μ match the one from data, presented in figure 1.3 of section 1.2.2. Experimental uncertainties are related to the reconstruction and the identification of electrons, muons, taus, jets and b-tagged jets which are all part of the $t\bar{t}H \rightarrow$ ML final state. Sources of uncertainty contributing to the jet energy scale and b-jet tagging are decomposed into uncorrelated components and treated as independent sources [78, 79, 80]. The jet energy scale (JES) overall uncertainty varies from 1% to 5.5% depending on the jet p_T. The three largest JES contribution to the analysis systematics are its component

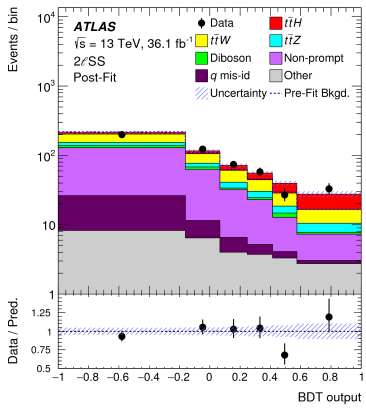

(a) $2\ell_{SS}$ discriminant

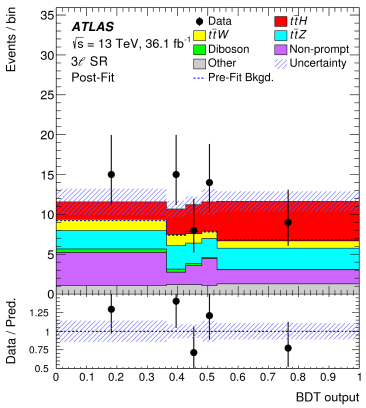

(b) 3ℓ discriminant

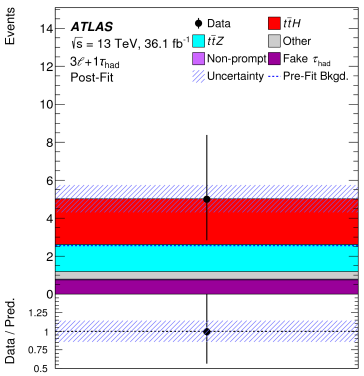

(c) Yields in the 3ℓ+$1\tau_{\text{had}}$ region

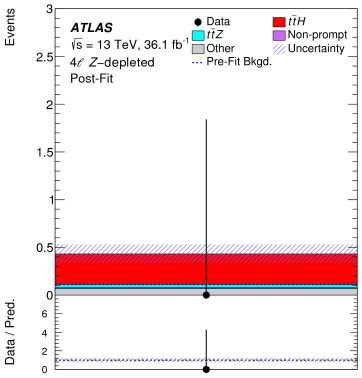

(d) 4ℓ Yields in the Z-depleted region

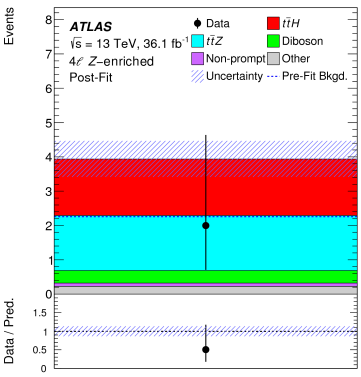

(e) 4ℓ Yields in the Z-enriched region

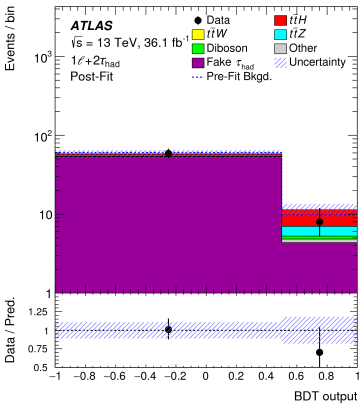

(f) 1ℓ+$2\tau_{\text{had}}$ discriminant

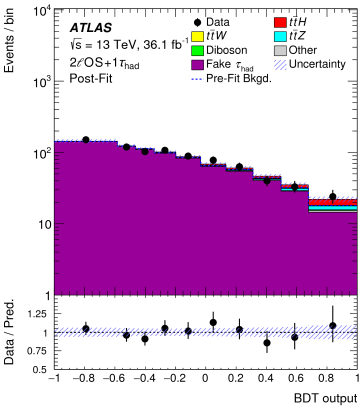

(g) $2\ell_{\text{OS}}$+$1\tau_{\text{had}}$ discriminant

FIGURE 6.2 – Final discriminants used in the fit for $2\ell_{SS}$, 3ℓ, 3ℓ+$1\tau_{\text{had}}$, 4ℓ, 1ℓ+$2\tau_{\text{had}}$ and $2\ell_{\text{OS}}$+$1\tau_{\text{had}}$ [62].

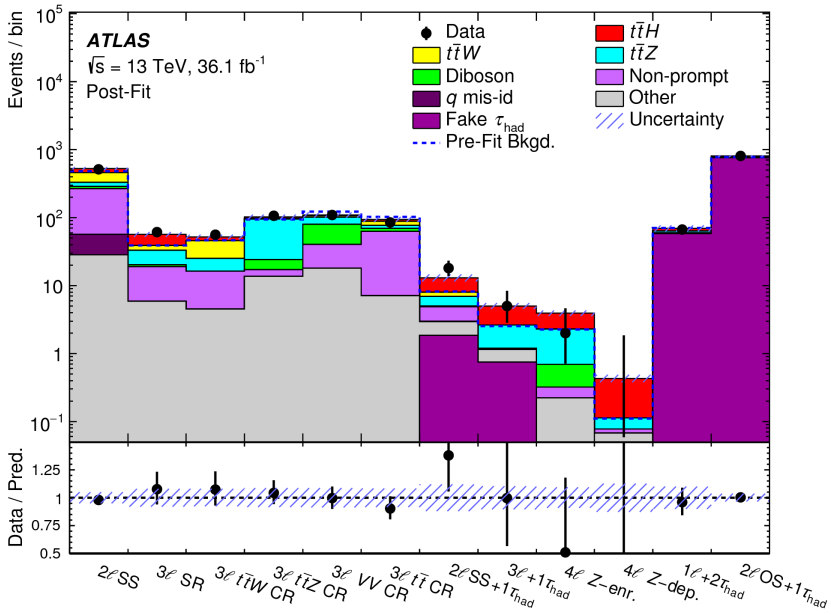

FIGURE 6.3 – Left : Comparison of prediction to data after the fit in the eight signal and four control regions of the $t\bar{t}H \rightarrow$ ML fit [62].

related to the pile-up uncertainty subtraction, the different responses to quark and gluon jets (flavour composition), and in situ calibration in data. The multilepton analysis combination is particularly sensitive to JES because of a consistently high jet multiplicity of all of its final states, and the fact JES component are fully correlated across channels. In comparison, the lepton types and multiplicity vary across channels which mitigates the global impact.

The approximate relative size of the b-tagging efficiency uncertainty is 2% for b-jets, 10% for c-jets and τs, and 30% for light jets. The impact of the tagging uncertainty for jets containing either c-hadrons or τ_{had} is significant and, due to the calibration procedure applied, is taken as fully correlated between the two jet flavours.

Uncertainties in electron and muon reconstruction, identification, isolation and trigger efficiencies have negligible impact. The uncertainty in the identification efficiency for τ_{had} is 6% [75].

All individual experimental systematic uncertainties are fully correlated across channels with the exception of those related to the quark/gluon jet composition, that composition varying depending on the channel considered.

↝ The last type of systematic uncertainties is related to the fake light leptons and taus estimates.

The uncertainty on data-driven non-prompt light leptons have large effects on individual channels since they cover a large proportion of the background, but their correlation across channels is not possible due to the difference of the methods, except for the Matrix Method used both for $2\ell_{SS}$ and 3ℓ and for which all parameters are correlated. The biggest source of uncertainty for data-driven methods generally are the non-closure, which is defined as the difference between the number of MC events in the signal region and the number found

by applying the fake estimate method to MC control regions (as if it were data). If the statistical uncertainty from applying the data-driven estimate method to MC is bigger than the observed deviation, then it is taken as the non-closure number.

Additional systematics are added to account for prompt leptons backgrounds subtraction from the control regions where the methods are applied. Finally, the total uncertainty in the non-prompt lepton estimate varies from 20% to 30% for $2\ell_{SS}$ and 3ℓ. Due to lower $t\bar{t}$ MC statistics it is instead 55% for $2\ell_{SS}$+τ_{had} (see 5.3).

For jets faking taus, a semi data-driven method is used, where a scale factor is defined as the ratio of data and MC in a tau fakes enriched region $2\ell_{\text{OS}}$+$1\tau_{\text{had}}$ (see Figure 6.2g). Indeed in $2\ell_{\text{OS}}$+$1\tau_{\text{had}}$ all light leptons are true because of the widely dominant $t\bar{t}$ contribution to the opposite sign final state. This normalisation is measured to be $\tau_{SF} = 1.36 \pm 0.16$, including statistical and systematic uncertainties. The size of the systematic uncertainty is estimated by measuring the different scale factors in $t\bar{t}$ enriched and Z-enriched control regions, to take into account the variation of composition of the source of tau fakes. It is applied to other channels, 3ℓ+$1\tau_{\text{had}}$ and $2\ell_{SS}$+τ_{had} by scaling MC predicted fake taus simultaneously in the fit.

The dominant background in the 1ℓ+$2\tau_{\text{had}}$ channel is $t\bar{t}$ where one or two of the tau is faked by a jet. As there is equal probability for a jet to be reconstructed as a positively or negatively charged τ_{had}, the fakes are estimated from a control region identical to the signal region except that the two τ_{had} in the event are required to have the same charge. The estimate is extrapolated to the signal region after using simulation to subtract the contribution from real τ_{had} in the control region. Using simulation, the non-closure of this method was found to be below 30%, which is included as a systematic uncertainty.

In total 315 nuisance parameters (NP) are considered, most having experimental origin. A pruning procedure is applied, meaning that systematic uncertainties that have a negligible impact on the final results are removed to improve the speed of the fit : a normalization or a shape uncertainty is not applied if the associated variation is below 1% in all bins. This reduces the number of nuisance parameters to 230. Most of the neglected nuisance parameters are those related to flavour tagging.

6.1.1.3 $t\bar{t}H \rightarrow$ ML combination results

A maximum-likelihood fit is performed on all these twelve categories simultaneously to extract the $t\bar{t}H$ signal cross section normalised to the SM prediction (μ). The statistical analysis of the data uses a binned likelihood function $\mathcal{L}(\mu, \theta)$, which is constructed from a product of Poisson probability terms to estimate μ. The Higgs boson branching fractions and the cross section for associated production of a Higgs boson and a single top quark, which is treated as background, are set to their SM expectations with appropriate theoretical uncertainties (see section 6.1.3). As explained in section 6.1.1.1, five signal regions use a BDT as discriminant and four others are a single bins. The total number of bins used in the fit is 32.

The impact of systematic uncertainties on the signal and background expectations is described by nuisance parameters (NPs), θ, which are constrained by Gaussian or log-normal probability density functions. The latter are used for normalisation factors to ensure that they are always positive. The expected numbers of signal and background events are functions of θ.

The test statistic, q_μ, is constructed from the profile log-likelihood ratio from Equation 3.5.

The contribution from given systematic uncertainties to the uncertainty on the signal strength

Systematic uncertainty	Type	Components
Luminosity	N	1
Pileup reweighting	SN	1
Physics Objects		
Electron	SN	6
Muon	SN	15
τ_{had}	SN	10
Jet energy scale and resolution	SN	28
Jet vertex fraction	SN	1
Jet flavor tagging	SN	126
$E_{\text{T}}^{\text{miss}}$	SN	3
Total (Experimental)	–	191
Data-driven non-prompt/fake leptons and charge misassignment		
Control region statistics	SN	38
Light-lepton efficiencies	SN	22
Non-prompt light-lepton estimates: non-closure	N	5
γ-conversion fraction	N	5
Fake τ_{had} estimates	N/SN	12
Electron charge misassignment	SN	1
Total (Data-driven reducible background)	–	83
$t\bar{t}H$ **modeling**		
Cross section	N	2
Renormalization and factorization scales	S	3
Parton shower and hadronization model	SN	1
Higgs boson branching fraction	N	4
Shower tune	SN	1
$t\bar{t}W$ **modeling**		
Cross section	N	2
Renormalization and factorization scales	S	3
Matrix-element MC event generator	SN	1
Shower tune	SN	1
$t\bar{t}Z$ **modeling**		
Cross section	N	2
Renormalization and factorization scales	S	3
Matrix-element MC event generator	SN	1
Shower tune	SN	1
Other background modeling		
Cross section	N	15
Shower tune	SN	1
Total (Signal and background modeling)	–	41
Total (Overall)	–	315

TABLE 6.1 – $t\bar{t}H \rightarrow$ ML sources of systematic uncertainties, type of treatment (SN = shape and normalisation ; N = normalisation only) and number of nuisance parameters attached (components) [62].

are found by subtracting in quadrature the statistical uncertainty, determined by fixing all NPs to their best-fit values, from the total uncertainty.

The expected results are obtained in the same way as the observed results by replacing the data in each input bin by an asimov dataset of the prediction from simulation and non-prompt estimates. Even for expected results, all NPs are profiled, namely set to their best-fit values obtained from the fit to data. The significance is obtained from the test statistic in the asymptotic limit [46]. As the 4ℓ channel has few events, the validity of this assumption was verified using pseudo-experiments.

The behaviour of the global fit is studied by performing a number of checks including evaluating how much each NP is pulled from its nominal value (pulls), how much its uncertainty decreases from the nominal uncertainty (constraints) and which correlations develop between initially uncorrelated systematic uncertainties. The stability of the results was tested by performing fits for each channel independently and in combination.

The impact of each systematic uncertainty on the final result is assessed by performing a fit with the parameter of interest fixed to its fitted value varied up or down by its fitted 1σ uncertainty, whereas all the other parameters are allowed to vary, and calculating the $\Delta\mu$ with respect to the baseline fit. The result on Figure 6.4 right is called a ranking plot. The impact of nuisance parameters grouped by type of systematic uncertainty source is shown on figure 6.4 left. The most highly ranked source of systematic uncertainties on the measurement are the ones related to the theoretical modelling of $t\bar{t}H$, followed closely by jet related uncertainties and uncertainties arising from non-prompt light lepton estimates.

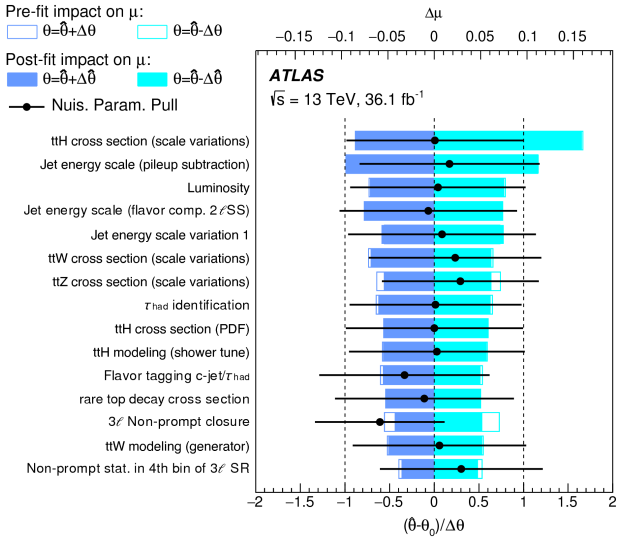

Uncertainty Source	$\Delta\mu$	
$t\bar{t}H$ modeling (cross section)	+0.20	−0.09
Jet energy scale and resolution	+0.18	−0.15
Non-prompt light-lepton estimates	+0.15	−0.13
Jet flavor tagging and τ_{had} identification	+0.11	−0.09
$t\bar{t}W$ modeling	+0.10	−0.09
$t\bar{t}Z$ modeling	+0.08	−0.07
Other background modeling	+0.08	−0.07
Luminosity	+0.08	−0.06
$t\bar{t}H$ modeling (acceptance)	+0.08	−0.04
Fake τ_{had} estimates	+0.07	−0.07
Other experimental uncertainties	+0.05	−0.04
Simulation sample size	+0.04	−0.04
Charge misassignment	+0.01	−0.01
Total systematic uncertainty	+0.39	−0.30

FIGURE 6.4 – $t\bar{t}H \rightarrow$ ML dominant systematics and impact on signal strength measurement uncertainty [62].

The measured values standalone sensitivities and fitted signal strength of all channel are given in Figure 6.5a.

Figure 6.5b shows the combined event yields in all analyses categories as a function of the log of their purity log(S/B), where S is the expected signal yield and B the background yield extracted from the fit with freely floating signal. A clear $t\bar{t}H$ signal-like excess over the background is visible for high purity. On Figure 6.5a, the relative size of the statistical and systematic related

uncertainty component shows that the 4ℓ, $3\ell{+}1\tau_{\text{had}}$ and $2\ell_{SS}{+}\tau_{\text{had}}$ channels are still statistically limited, whereas $2\ell_{SS}$, 3ℓ and $1\ell{+}2\tau_{\text{had}}$ are systematics limited.

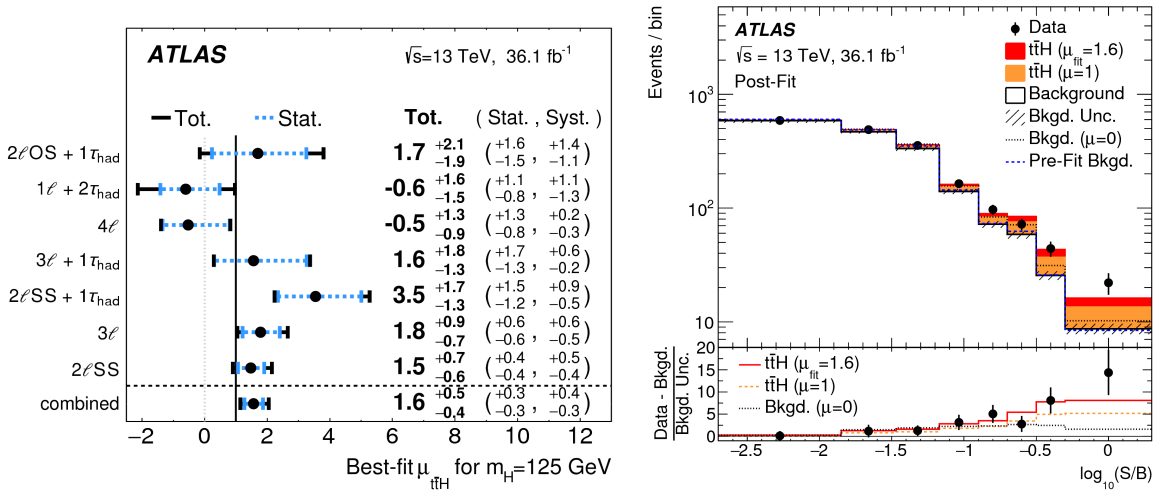

(a) Best fit values

(b) Purity-weighted events distribution

FIGURE 6.5 – Results from the $t\bar{t}H \to$ ML statistical combination [62]. Left : Observed best-fit values of the $t\bar{t}H$ signal strength μ and their uncertainties, by final state category, and combined. The individual μ values for the channels are obtained from a simultaneous fit with the signal strength parameter for each channel floating independently. Right : Event yields as a function of log10(S/B) : each event is weighted by his category purity [62].

Once corrected by the fiducial acceptance, the signal strength result $\mu_{t\bar{t}H}$ can be translated into a $t\bar{t}H$ production cross section measurement of $\sigma_{t\bar{t}H} = 590^{+160}_{-150}$ fb, which is in good agreement with the SM prediction $\sigma_{t\bar{t}H} = 507^{+35}_{-50}$ fb.

6.1.2 $t\bar{t}H$ final states combination

The $t\bar{t}H \to$ ML result described in section 6.1.1 is then combined with all studied $t\bar{t}H$ final states :

- $H \to b\bar{b}$ final states [55], split into two channels depending on the type of $t\bar{t}$ decay :
  - $t\bar{t} \to$ lepton+jet, also called 1-lepton
  - dileptonic $t\bar{t}$, also called 2-lepton
- $H \to \gamma\gamma$ decay channels [85], analysis also optimised separately according to the type of $t\bar{t}$pair decay :
  - lepton+jets/dileptonic $t\bar{t}$
  - all-hadronic $t\bar{t}$
- $H \to ZZ \to 4\ell$ is a single category including all $t\bar{t}$ decay channels [83].

In addition, specialised categories sensitive to $tHqb/WtH$ production also have significant $t\bar{t}H$ acceptance and are included [85], [40].

The overlap between the signal and control regions of all the analyses was checked and found to be negligible. All analyses use the same Monte Carlo event generators for $t\bar{t}H$ production, and use nominal Higgs boson decay branching fractions from reference [70] assuming $m_H = 125$ GeV.

The single top quark and Higgs boson associated production processes $tHqb$ and WtH (see figure 6.7), described in section 6.1.3, are considered backgrounds and fixed to their SM predictions with appropriate theoretical uncertainties. All Higgs boson production mechanisms other than tH and $t\bar{t}H$ contribute negligibly to the multilepton and $H \rightarrow b\bar{b}$ analyses and are ignored. The $H \rightarrow \gamma\gamma$ and $H \rightarrow ZZ$ events considered in this combination are $t\bar{t}H$-enhanced dedicated categories in the global analysis including all production modes. These categories have non-negligible contamination from other production mechanisms. The $t\bar{t}H$ signal strength $\mu_{t\bar{t}H}$ is the free parameter of the fit. Signal strength from other Higgs boson production modes are all set to their SM expectations with theoretical errors considered as systematic uncertainties.

The combined likelihood function $\mathcal{L}(\mu, \theta)$ is obtained from the product of likelihood functions of the individual analyses, where the nuisance parameters are fully correlated whenever possible. In particular, all Higgs boson production and decays theoretical uncertainties are linked. That is also the case for cross-sections and modelling uncertainty of MC-predicted $t\bar{t}Z$, $t\bar{t}W$, tZ, di-boson, Wt, $t\bar{t}t\bar{t}$, $t\bar{t}WW$ backgrounds used for both $H \rightarrow b\bar{b}$ and ML analyses. This is not the case for the dominant $t\bar{t}$ ($t\bar{t}b\bar{b}$) background from $H \rightarrow b\bar{b}$ that is estimated in different phase space and with data-driven methods in the ML channels. The dominant jet energy scale, jet energy resolution and flavour tagging uncertainties are fully correlated across analyses at the exception of the jet flavour composition that is channel dependent, and the b-tagging uncertainty which working point (see 5.1.4) is different for ML+$H \rightarrow b\bar{b}$ and $H \rightarrow \gamma\gamma$ + $H \rightarrow ZZ$. The flavour-tagging uncertainty are strongly constrained by the $H \rightarrow b\bar{b}$ analysis due to its large samples of c and b jets. Other experimental systematic uncertainties such as luminosity, pile-up effects, lepton identification, isolation, and trigger efficiencies are treated as correlated. When updating to 80 fb^{-1}, the $H \rightarrow \gamma\gamma$ and $H \rightarrow ZZ$ analyses used updated and improved reconstruction software, hence their experimental systematic uncertainties are de-correlated from the ML and $b\bar{b}$ ones. For the same reason, most of instrumental systematics are not correlated between run 1 and run 2. $H \rightarrow b\bar{b}$ and H$\rightarrow$ML analyses use the same 36.1 fb^{-1} of 13 TeV data, whereas $H \rightarrow \gamma\gamma$ and $H \rightarrow ZZ$ were updated to 80 fb^{-1} of 13 TeV data.

In the 36 fb^{-1} analysis [62], the ML final state is the most sensitive final state with a significance of 4.1 σ (2.8 σ) observed (expected). The combination of all final states allows to claim for an evidence for the $t\bar{t}H$ production mode with 4.2 σ observed and 3.8 σ expected. The signal strength of each $t\bar{t}H$ final state and their combination is shown on figure 6.8a. The $b\bar{b}$ and ZZ final states are slightly below standard model value while ML and $\gamma\gamma$ are above, although all results are compatible within a little more than 1 sigma uncertainty. Another important message from this plot is the fact that $b\bar{b}$ and ML are from now on limited by their systematic uncertainties, meaning that an important amount of work is needed to improve results, not only on the analysis strategy, but also on reconstructed objects and theory modelling. On the contrary, the $\gamma\gamma$ and four leptons final states will benefit fully from additional integrated luminosity.

The extension of the $H \rightarrow \gamma\gamma$ and $H \rightarrow ZZ$ analyses with 2017 data [47] [40] (see table 6.6) then allowed to claim for an observation, with 5.8 standard deviations for 4.9 σ expected. By combining with Run 1 results, in particular the Run 1 multilepton analysis, the observed (expected) sensitivity goes up to 6.3 (5.1) σ. The statistics of data used for the combined observation of the $t\bar{t}H$ process are summarised in table 6.6.

Assuming standard model branching fractions, the total $t\bar{t}H$ production cross section at

Analysis	Integrated luminosity [fb^{-1}]	Expected significance	Observed significance
$H \to \gamma\gamma$	79.8	3.7 σ	4.1 σ
$H \to$ multilepton	36.1	2.8 σ	4.1 σ
$H \to b\bar{b}$	36.1	1.6 σ	1.4 σ
$H \to ZZ^* \to 4\ell$	79.8	1.2 σ	0 σ
Combined (13 TeV)	36.1−79.8	4.9 σ	5.8 σ
Combined (7, 8, 13 TeV)	4.5, 20.3, 36.1−79.8	5.1 σ	6.3 σ

FIGURE 6.6 – Analyses and datasets used for the $t\bar{t}H$ observation [40].

13 TeV is measured to be 670 ± 90 (stat.) $^{+110}_{-100}$ (syst.) fb which is compatible with the SM expected value (507 fb). Thanks to the variety of final states studied, the $t\bar{t}H$ combination is sensitive to several Higgs boson decay modes, multilepton channels contributing to WW, $\tau\tau$ and ZZ decays. The combination of $t\bar{t}H$ channels is also able to resolve the relative sign of the two couplings excluding the possibility that $\kappa_F < 0$ at 95%. Figure 6.9a shows a likelihood scan performed in the $\kappa_V - \kappa_F$ plane obtained by a combination with others Higgs boson production and decay modes. The κ-framework is introduced in section 6.1.3.

6.1.3 Single top + Higgs boson production (tH) and the κ-framework

In the nominal $t\bar{t}H$ analysis, tH is considered as a SM background that scales with the Higgs boson production signal strength as fitted in the data from $t\bar{t}H$. But for couplings measurement purposes, a dedicated signal strength parameterisation for tH and $t\bar{t}H$ signals can be used as handle to measure and constraint the relative sign of the Higgs boson coupling to bosons and fermions.

Let Γ_{tot} be the total width of the Higgs boson and Γ_f the partial width for Higgs boson decay to the final state f. A set of coupling modifiers, κ, is introduced to parameterise possible deviations from the SM predictions of the Higgs boson couplings to SM bosons and fermions. For a given production process or decay mode, denoted j, a coupling modifier κ_j is defined such that :

$$\kappa_j^2 = \frac{\sigma_j}{\sigma_j^{SM}} = \frac{\Gamma_j}{\Gamma_j^{SM}} \tag{6.1}$$

By construction, κ are equal to unity in the SM case. Kappas ease spotting of beyond SM physics when they deviate significantly from one. In a first parameterisation, one can assume that all processes involving fermion couplings are scaled by $\kappa_F = \kappa_t = \kappa_b = \kappa_\tau$ and all weak vector boson couplings by $\kappa_V = \kappa_W = \kappa_Z$.

In the case of the tH process, the interference of production modes involving κ_t and production modes involving κ_W illustrated on Figure 6.7 can be parameterised as :

$$\sigma(tH) = a\kappa_t^2 - b\kappa_t * \kappa_W + c\kappa_W^2 \tag{6.2}$$

where a, b, c >0. In the Standard Model case $\kappa_t = \kappa_W = 1$, $\sigma(tH) \simeq 19.9$ fb at $\sqrt{s}$=8 TeV and for m_H =125 GeV (18.7 fb for t-channel 6.7 and 1.2 fb for s-channel [86]), and 76.9 fb at $\sqrt{s}$=13 TeV (74 fb for t-channel 6.7 and 2.9 fb for s-channel [86]).

In the case where κ_t=-κ_W, then the tH cross section is increased by a factor ten due to constructive interference. Analyses sensitive to the tH process are therefore sensitive to the

relative sign of the Higgs boson's coupling to fermions and bosons, and used to spot a potential deviation from SM.

The final state of tH is very close to that of $t\bar{t}H$, with a lower jet multiplicity. It can also be searched for in $b\bar{b}$, $\gamma\gamma$ and multilepton final states.

CMS has performed tH-targeting specific analysis whereas ATLAS has so far built tH-specific categories in the $\gamma\gamma$ final state only.

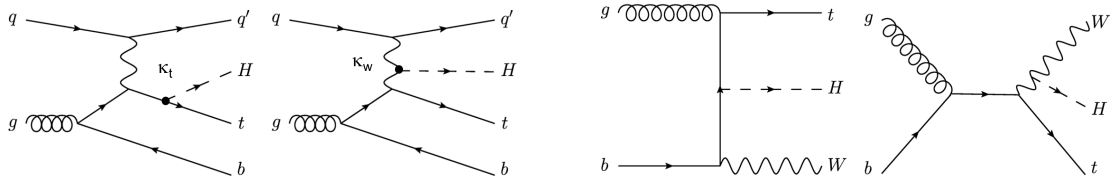

(a) tHq (b) tHW

FIGURE 6.7 – Feynman diagrams for tH production (dominant t-channels).

The κ_F/κ_V measurement can be done in two scenarios. In the first scenario, the $H \rightarrow \gamma\gamma$ (3.1) and gluon fusion (1.5) loops are resolved, meaning we assume the processes are result of the respective interaction of the Higgs boson with the W boson and top quark. In that case the ggF and $H \rightarrow \gamma\gamma$ analyses apply a strong but indirect constraint on κ_F/κ_V that is evoked in section 6.1.4 which is dedicated to the overall Higgs boson couplings measurement. In a second scenario where we do not make such assumption on the loops and allow for them to host new physics, the sensitivity to κ_F/κ_V is provided by the presence of tH events in the $t\bar{t}H$ analyses. As only the relative sign of the κ factors is meaningful, the convention that $\kappa_V \geq 0$ is chosen. The couplings modifiers used in the effective and resolved scenarios are given in table 6.2.

6.1.4 Higgs boson couplings results

The Higgs boson's mass is a free parameter of the standard model. Its discovery at 125 GeV [66] [87] is a serendipity for experimentalists considering it is the mass where decays in all final states is possible, and the measurement of its couplings to many elementary particles is enabled.

My contribution to the global combined result during run 1 was to provide the $t\bar{t}H \rightarrow$ ML combination *workspace* and insure its compatibility with general ATLAS couplings policy as well as those from CMS, such as the alignement of $t\bar{t}V$ generators, in order to allow ATLAS [63] and LHC couplings combination paper [64]. For run 2 analyses I have been advising students and teams on providing these results.

The analyses used to derive the latest results and corresponding datasets are detailed in table 6.3, and the analysis is described in [88]. The measurement combines results from the $H \rightarrow \gamma\gamma$, $H \rightarrow ZZ \rightarrow 4\ell$, $H \rightarrow WW \rightarrow e\nu\mu\nu$, $H \rightarrow \tau\tau$, VH, $H \rightarrow b\bar{b}$, $H \rightarrow \mu\mu$ and $t\bar{t}H \rightarrow$ MLand $t\bar{t}H \rightarrow b\bar{b}$. One of the major task towards combining these channels is a thorough examination of the correlation scheme. Anything that can possibly be correlated is, which is in particular enabled by the use of common objects reconstruction and identification, and previously agreed similar classification for theoretical sources of uncertainties. The global measured signal strength, all production modes combined as shown on figure 6.8b, is $\mu = 1.13^{+0.09}_{-0.08} = 1.13 \pm 0.05$ (stat.) $\pm$ 0.05 (exp.) $^{+0.05}_{-0.04}$ (sig. th.) $\pm$ 0.03 (bkg. th.).

The simultaneous measurement of Higgs boson couplings to fermions and bosons gives a

Production	Effective modifier	Resolved modifier
σ_{ggF}	κ_g^2	$1.04\,\kappa_t^2 + 0.002\,\kappa_b^2 - 0.04\,\kappa_t\kappa_b$
σ_{VBF}	-	$0.73\,\kappa_W^2 + 0.27\,\kappa_Z^2$
$\sigma_{qq/qg\to ZH}$	-	κ_Z^2
$\sigma_{gg\to ZH}$	-	$2.46\,\kappa_Z^2 + 0.46\,\kappa_t^2 - 1.90\,\kappa_Z\kappa_t$
σ_{WH}	-	κ_W^2
$\sigma_{t\bar{t}H}$	-	κ_t^2
σ_{tHW}	-	$2.91\,\kappa_t^2 + 2.31\,\kappa_W^2 - 4.22\,\kappa_t\kappa_W$
σ_{tHq}	-	$2.63\,\kappa_t^2 + 3.58\,\kappa_W^2 - 5.21\,\kappa_t\kappa_W$
$\sigma_{b\bar{b}H}$	-	κ_b^2
Partial decay width	**Effective modifier**	**Resolved modifier**
$\Gamma_{\gamma\gamma}$	κ_γ^2	$1.59\,\kappa_W^2 + 0.07\,\kappa_t^2 - 0.67\,\kappa_W\kappa_t$
Γ_{ZZ}	-	κ_Z^2
Γ_{WW}	-	κ_W^2
$\Gamma_{\tau\tau}$	-	κ_τ^2
Γ_{bb}	-	κ_b^2
$\Gamma_{\mu\mu}$	-	κ_μ^2
Γ_{gg}	κ_g^2	$1.11\,\kappa_t^2 + 0.01\,\kappa_b^2 - 0.12\,\kappa_t\kappa_b$
$\Gamma_{Z\gamma}$	$\kappa_{(Z\gamma)}^2$	$1.12\,\kappa_W^2 - 0.12\,\kappa_W\kappa_t$
Total width	**Efective modifier**	**Resolved modifier**
Γ_H	κ_H^2	$(0.58\,\kappa_b^2 + 0.22\,\kappa_W^2 + 0.08\,\kappa_g^2 + 0.06\,\kappa_\tau^2 + 0.03\,\kappa_Z^2 + 0.03\,\kappa_c^2$ $+0.0023\,\kappa_\gamma^2 + 0.0015\,\kappa_{(Z\gamma)}^2 + 0.0004\,\kappa_s^2 + 0.00022\,\kappa_\mu^2)/(1 - \mathrm{B_{BSM}})$

TABLE 6.2 – Description of the effective and resolved modifiers used for the resolved and effective scenarios [63].

Analysis	Integrated luminosity (fb^{-1})
$H \to \gamma\gamma$ (including $t\bar{t}H$, $H \to \gamma\gamma$)	79.8
$H \to ZZ^* \to 4\ell$ (including $t\bar{t}H$, $H \to ZZ^* \to 4\ell$)	79.8
$H \to WW^* \to e\nu\mu\nu$	36.1
$H \to \tau\tau$	36.1
VH, $H \to b\bar{b}$	36.1
$H \to \mu\mu$	79.8
$t\bar{t}H$, $H \to b\bar{b}$ and $t\bar{t}H$ multilepton	36.1

TABLE 6.3 – Analyses and datasets used for the Higgs boson couplings measurement [88].

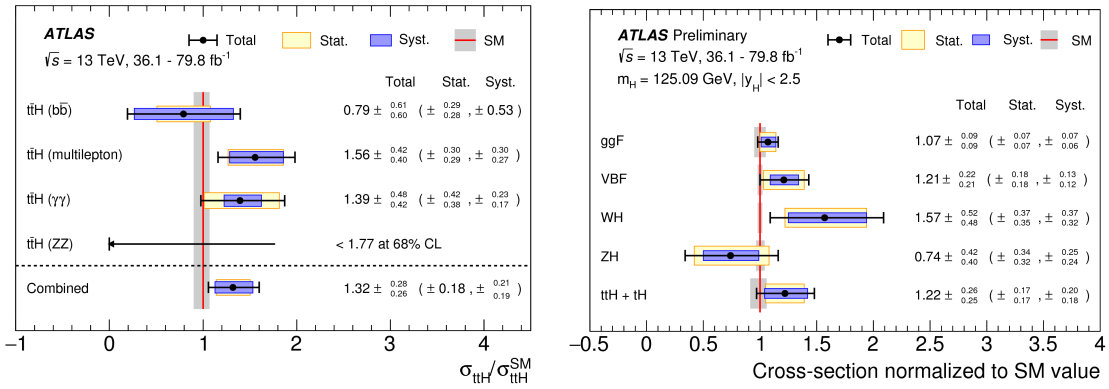

(a) $t\bar{t}H$ combination

(b) Higgs production modes combination

FIGURE 6.8 – Combination of all $t\bar{t}H$ results [40] (left) and combination of all Higgs production modes [88] (right). Right : Cross-sections for ggF, VBF, WH, ZH and ttH+tH normalised to their SM predictions, measured with the assumption of SM branching fractions. The black error bars, blue boxes and yellow boxes show the total, systematic, and statistical uncertainties in the measurements, respectively. The grey bands indicate the theory uncertainties in the cross-section predictions.

result of $\kappa_V = 1.06 \pm 0.04$ and $\kappa_F = 1.05 \pm 0.09$, for which confidence ellipses are shown in Figure 6.9b. The compatibility of this measurement with the SM corresponds to a p-value of 31%. Tables 6.4 shows the couplings modifiers measured on 80 fb^{-1} of 13 TeV data by combining all available Higgs boson production modes and decays analyses. As explained in section 6.1.3, the resolved loops scenario assumes means that we assume no unknown particle is entering the loops in the Higgs production and decay diagrams. That is in particular for the gluon fusion loop (Figure 1.5) and the $H \rightarrow \gamma\gamma$ loop (Figure 3.1). The effective photon and gluon coupling scenario makes no such assumption. The no B_{BSM} hypothesis means the branching ratio of the Higgs boson decaying to beyond standard model particles is set to 0, whereas it is left free in the fit in the scenario with B_{BSM}. Effective and resolved scenarios rely on the scheme displayed in 6.2.

Parameter	Result
κ_Z	1.10 ± 0.08
κ_W	1.05 ± 0.08
κ_b	$1.06^{+0.19}_{-0.18}$
κ_t	$1.02^{+0.11}_{-0.10}$
κ_τ	1.07 ± 0.15
κ_μ	< 1.51 at 95% CL.

Parameter	(a) $B_{inv} = B_{undet} = 0$	(b) B_{inv} free, $B_{undet} \geq 0$, $\kappa_{W,Z} \leq 1$	(c) $B_{BSM} \geq 0$, $\kappa_{off} = \kappa_{on}$
κ_Z	1.11 ± 0.08	> 0.87 at 95% CL	$1.16^{+0.18}_{-0.13}$
κ_W	1.05 ± 0.09	> 0.85 at 95% CL	$1.12^{+0.18}_{-0.15}$
κ_b	$1.03^{+0.19}_{-0.17}$	0.88 ± 0.13	$1.08^{+0.25}_{-0.20}$
κ_t	$1.09^{+0.15}_{-0.14}$	$[-1.03, -0.79] \cup [0.93, 1.24]$ at 68% CL	$1.14^{+0.19}_{-0.18}$
κ_τ	$1.05^{+0.16}_{-0.15}$	0.97 ± 0.13	$1.12^{+0.23}_{-0.21}$
κ_γ	1.05 ± 0.09	0.98 ± 0.07	$1.10^{+0.19}_{-0.13}$
κ_g	$0.99^{+0.11}_{-0.10}$	$1.01^{+0.13}_{-0.11}$	$1.02^{+0.22}_{-0.13}$
B_{inv}	-	< 0.30 at 95% CL	-
B_{undet}	-	< 0.22 at 95% CL	-
B_{BSM}	-	-	< 0.47 at 95% CL

TABLE 6.4 – Measured couplings modifiers [88] (see equation 6.1) with 80 fb^{-1} of 13 TeV data. (a) No invisible (B_{inv} : H→E_T^{miss}) or undetected (B_{undet} : undetected decays or to which no analysis is sensitive such as H→light quarks or H→BSM) contributions. (b) B_{inv} and B_{undet} left free floating. (c) $B_{BSM} = B_{inv} + B_{undet}$ as free parameter, and the off-shell and on-shell Higgs boson intensities are assumed to be the same.

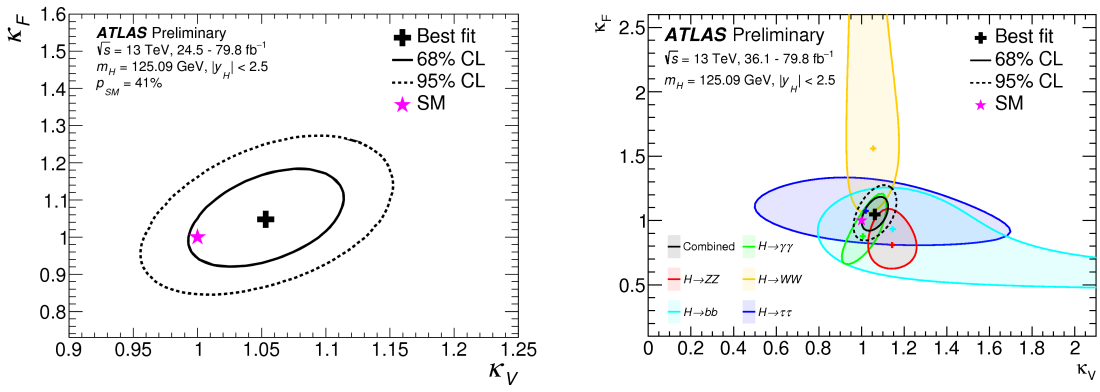

(a) κ_F and κ_V 1σ ellipse

(b) κ_F and κ_V 1σ per Higgs decay and combination

FIGURE 6.9 – Left : κ_F and κ_V 1σ ellipse with combined result [88]. Right : Constraint on relative Higgs boson couplings with fermions and bosons [88].

Reduced couplings strength as a function of the mass of the particle is shown 6.10a, and their best fit values in figure 6.10b. This plot illustrates how perfectly does the Higgs boson fit its standard model prediction, and seems to be symptomatic of how the phase space to spot new physics in the Higgs sector is shrinking. However, the relative precision measured on Higgs couplings parameters Δ^H_{rel} is related to the scale for new physics Λ_{BSM} through $\Lambda_{BSM} > \frac{g^*}{g^{SM}} \frac{v}{\Delta^H_{rel}}$ where v is the Higgs field vacuum expectation value, g^* and g^{SM} are the new and standard model couplings constants respectively. Therefore, while measured deviations of the order of 10% only probes new physics at a scale of $\Lambda_{BSM} \simeq 500$ to 1000 GeV, a phase space that has already ruled out by direct searches at the LHC, reaching a percent-level precision in the Higgs sector is however highly desirable in the search for beyond standard model physics. Several plans are made to go beyond a seemingly perfectly non-deviant Higgs boson. Further precision measurement on the kappas, splitting the kinematic phase space (see the STXS framework below) and measuring the Higgs boson self-coupling addressed in section 9.2, are ways to continue to challenge the standard model Higgs boson paradigm.

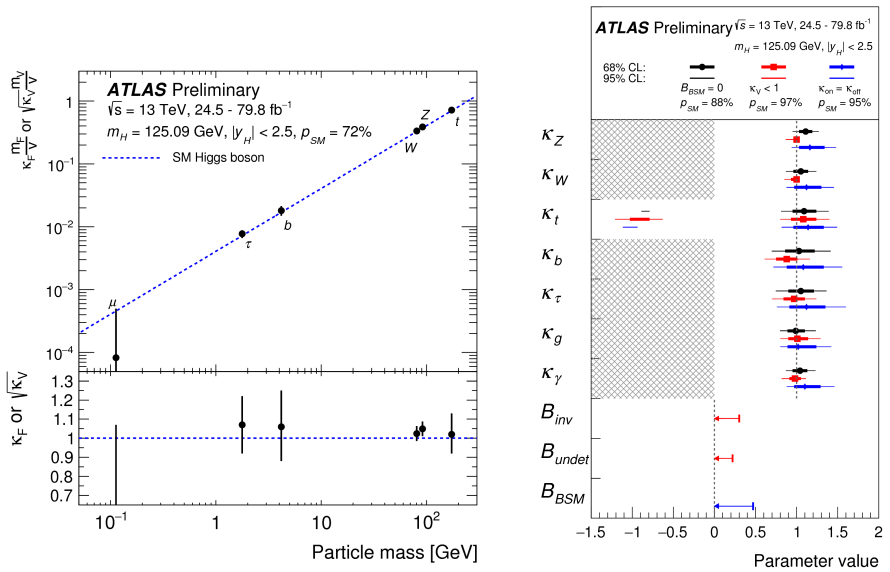

(a) Particle couplings vs mass

(b) Coupling modifiers

FIGURE 6.10 – Left : Measured coupling of elementary particles as a function of their mass (see equation 1.16), in particular the largest Yukawa to the top quark. The coupling to the bosons $\lambda_V \propto \frac{m_V^2}{v}$ is in GeV, so it is divided by the vev v for homogeneity with the unit-less $\lambda_F = \frac{1}{\sqrt{2}}\frac{m_F}{v}$ [88]. Right : couplings strength modifiers κ for photons, fermions t, b, τ, μ and weak gauge bosons W and Z. The couplings modifiers are measured assuming $B_{BSM} = 0$ (black) / B_{inv} and B_{undet} left free floating (red) / off-shell and on-shell Higgs boson intensities assumed to be the same (blue). The SM prediction for both cases is shown by a dotted line [88].

Analyses also now tend to be optimised in the context of the Simplified Template Cross Section (STXS) scheme, as for instance were the general $H \to \gamma\gamma$ and $H \to ZZ$ couplings results [89] performed on 36.1 fb^{-1} of 13 TeV data. Inclusive cross sections of all production and decay modes being so far SM-like, the objective is to further challenge the model by searching for deviations in various separated kinematic phase spaces. STXS is an ensemble of kinematic phase-space specific categories illustrated in Figure 6.11. Due to low statistics $t\bar{t}H$ is not yet split into categories for the first stages of the measurement, but on the contrary merged with tH production.

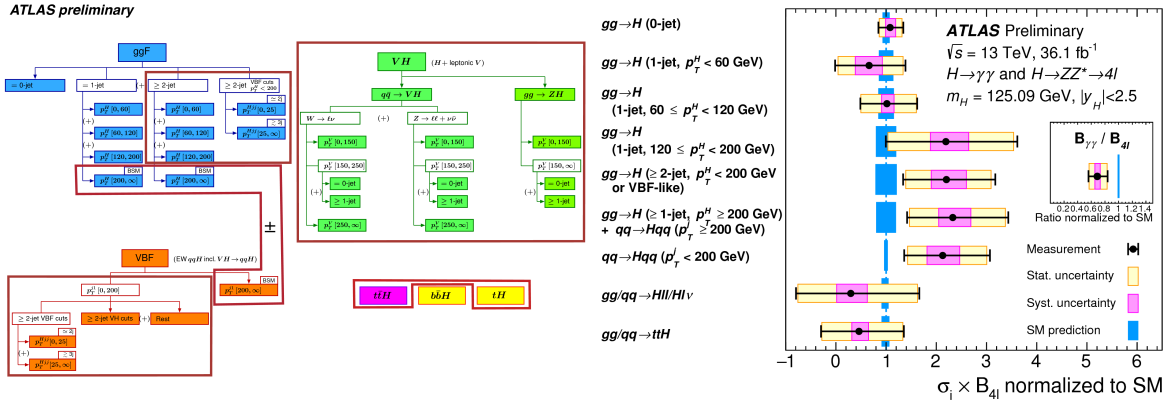

FIGURE 6.11 – Left : Simplified template cross section and stage-1 categories merging (red squares) [89]. Right : Best-fit results of the nine stage-1 STXS measurement regions for gluon fusion $H \to \gamma\gamma$ and $H \to ZZ$ for 36.1 fb^{-1} of 13 TeV data [89].

It is to be noted that, with the recent observations of $H \to b\bar{b}$ decay, as well as $t\bar{t}H$ and VH production by ATLAS [57], all major production modes and decays have been observed.

6.2 Flavour changing neutral currents re-interpretation

Considering the masses of the neutral bosons (Higgs boson with m_h =125 GeV, Z boson with m_Z =91 GeV and massless γ and gluon) compared to that of the top quark m_t =172.5 GeV, it is kinematically permitted for the top quark to decay into a charm or up quark and a neutral B boson $t \to qB$. In the SM, FCNC decays are very strongly suppressed since tqH interactions are forbidden at the tree level and even suppressed at higher-orders by the Glashow-Iliopoulos-Maiani (GIM) mechanism, where the flavour changing is done with a loop of two flavour changing charged current, see Figure 6.12a. The branching ratios are therefore theoretically predicted to be BR(t→Hu)$\simeq 10^{-17}$ and BR(t→ Hc)$\simeq 10^{-15}$. However, large enhancements in these branching ratios up to the level of BR(t→Hq)$\simeq 10^{-3}$ are possible in some beyond-SM scenarios where the GIM suppression can be relaxed and new particles can contribute to the loops, such as two-Higgs-doublet models (2HDM) among which the minimal supersymmetric SM (MSSM). This process can be searched for in $t\bar{t}H$ production where one of the top quarks decays through a FCNC process, as illustrated on figure 6.12b.

In the $pp \to t\bar{t}$, $\bar{t} \to bW$, $t \to qH$ final state, where one top decays leptonically and the Higgs decays to a pair of W bosons, a same sign lepton pair can arise and events can enter the $t\bar{t}H \to$ ML signal region. As a consequence, thanks to this vicinity of their final state, the

multilepton analysis could be statistically re-interpreted as a search for FCNC, which I performed by defining $t \rightarrow qH$ as signal, $t\bar{t}H$ as a standard model background, introducing new handles and reshaping the run 1 $t\bar{t}H \rightarrow$ ML combined workspace [65]. Indeed for that round of the multilepton analysis, the jet multiplicity was low enough ($N_j \geq 4$) for the ML analysis to include FCNC signal. For Run 2, ML final states jet multiplicity requirement for $2\ell_{SS}$ regions was later on raised from $N_j \geq 4$ to $N_j \geq 5$, since the change induced no loss in sensitivity but allowed for the data-driven fake estimate to increase its low N_{jets} control region statistics. Because of the lower jet multiplicity of the FCNC process compared to $t\bar{t}H$, a simple $t\bar{t}H \rightarrow$ ML re-interpretation was thus not possible. The analysis was then specifically re-optimised for run 2 with 36.1 fb^{-1} of 13 TeV data [90][91].

In run 1 analysis, only the three most sensitive ML channels, $2\ell_{SS}$, 3ℓ and $2\ell_{SS}+\tau_{\text{had}}$ are used. A counting experiment is performed with 3ℓ and $2\ell_{SS}+\tau_{\text{had}}$ as single bins and the $2\ell_{SS}$ final state split into six regions according to the lepton flavours (ee, eμ, $\mu\mu$) and jet multiplicity ($N_j = 4$ or $N_j \geq 5$). Comparison between data and predictions in each of those eight categories is shown on Figure 6.13. As shown on Figure 6.14 top, run 1 FCNC analyses results are coincidentally almost all pointing across final state to a $t \rightarrow Hu$ and $t \rightarrow Hc$ branching ratio of 0.2% [65]. The latest 13 TeV results for ML are now closer to zero (0.04% for tHu and -0.01% for tHu), as shown on Figure 6.14 bottom, and no significant excess is observed either in the $\gamma\gamma$ final state. The best observed upper limit on the branching ratio is measured by the ML analysis to be 0.16×10^{3} (resp. 0.19×10^{3}) for tHc (resp. tHu). Run 2 upper limits on the branching ratios for combined $\gamma\gamma$, ML and $b\bar{b}$ final states [92] are 1.1×10^{-3} observed (8.3×10^{-4} expected) for $t \rightarrow Hu$ and 1.2×10^{-3} observed (8.3×10^{-4} expected) for $t \rightarrow Hc$.

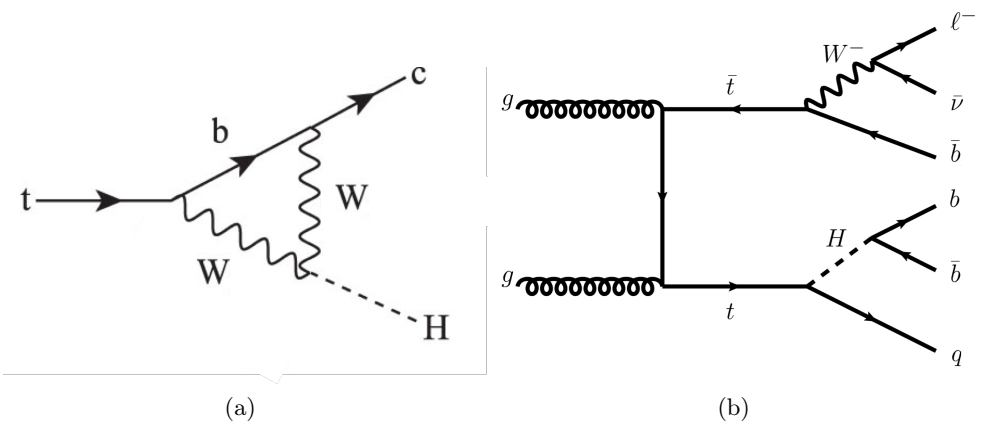

(a) (b)

FIGURE 6.12 – Left : Example of Feynman diagram for the decay $t \rightarrow cH$ in the SM. Right : Feynman diagram for flavour changing neutral current $t \rightarrow qH$ production.

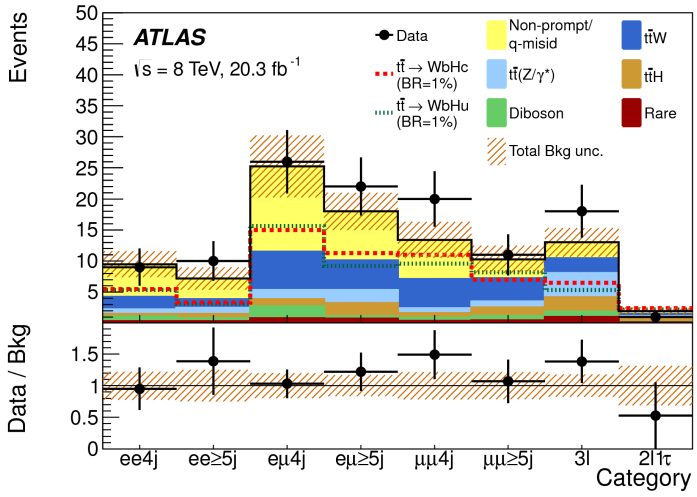

FIGURE 6.13 – Result of the ML FCNC analysis in each category [65].

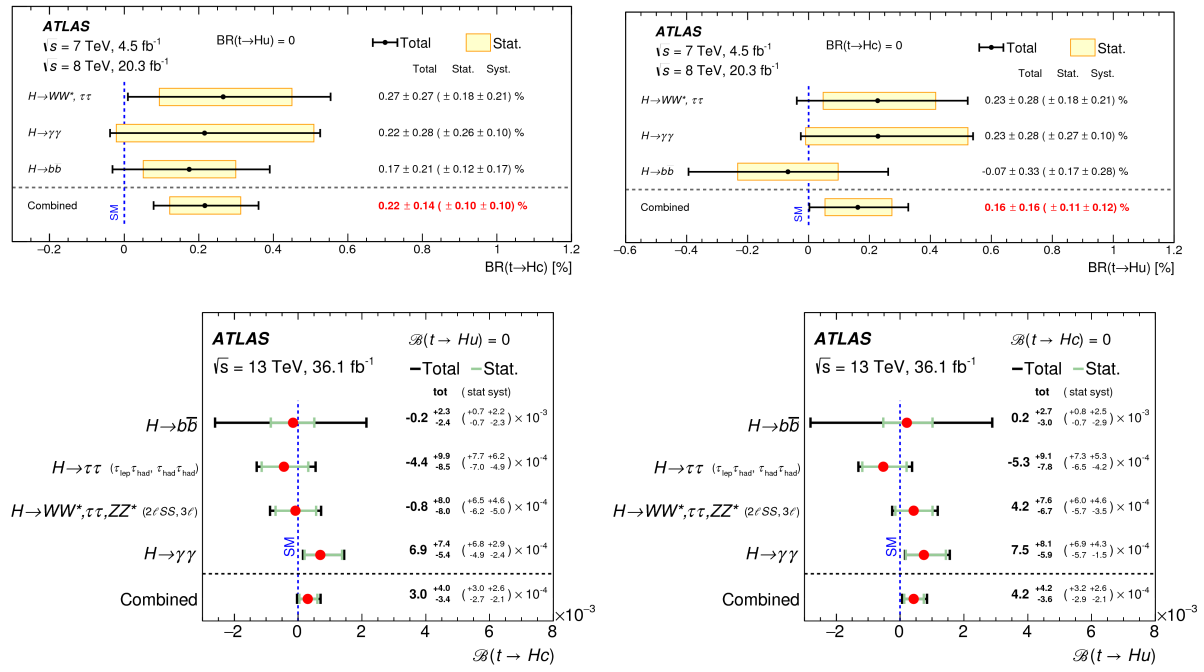

FIGURE 6.14 – Run 1 [65] (top) and run 2 [92] (bottom) result of the fitted branching ratio for $t \to cH$ (left) and $t \to uH$ (right) production search, for the $\gamma\gamma$, $b\bar{b}$ and ML final states and their combination.

III

Prospects

7. Future of $t\bar{t}H \rightarrow$ ML

The multilepton final state is currently facing two main limitations for its update with the full run 2 luminosity, that will be developed in the following sections. One of these issues concerns the fake leptons estimate, developed in section 7.1 and the other the growing relative importance of the irreducible $t\bar{t}V$ backgrounds 7.2. Finally, any longer term strategy involves the use of more refined techniques to extract every bit of information from the available dataset provided by the experiment. The possibility of using event reconstruction techniques and their compared advantages with deep learning techniques will be also be raised in this chapter.

Most of $t\bar{t}H \rightarrow$ ML final states are now starting to be limited by their systematic uncertainties. One of the best ways to improve its performance like that of many other analyses is to be involved in performance improvement studies. In particular, the high jet multiplicity of this final state makes it sensitive to jet energy scale and jet energy resolution. This aspect will be developed in section 8.

Now, one of the limitations to the ML analysis is the absence of resonance, unlike for the $\gamma\gamma$ and $b\bar{b}$ final states, which means that an excess in $t\bar{t}H \rightarrow$ ML alone without confirmation from other final states can be interpreted with difficulty. Indeed multilepton final states are the signature of many beyond standard model searches, in exotics and supersymmetric theory models. There is therefore a need for this analysis to be combined with other decay and production modes. A more global view of what can be done in terms of the couplings measurement of the lastly discovered elementary particle is developed in section 9.

7.1 Improvement of non-prompt lepton background rejection and estimate

One of the main issue appearing for $t\bar{t}H \rightarrow$ ML as data statistics accumulates concerns how to estimate the non-prompt leptons contribution in presence of photon conversions. Indeed photon conversion are not uniformly distributed across the kinematic discriminating variables used to optimise the channels, and their rate are different in control and signal regions. The increasing proportion of photon conversions is challenging the current fully data-driven estimate because it is only targeting b-jets faking leptons.

Indeed the composition of the fakes entering the $t\bar{t}H$ multilepton signal regions is not dominated by a single type, but a mixture of several types (semileptonic b-decays, photon conversions, etc.), as shown on figure 7.1.

In the current update of the future analysis, the custom lepton isolation described in 5.1.5 is further tightened to increase the rejection of the reducible background due to non-prompt leptons (fakes). This algorithm being based on isolation-related variables, like charged particles in a cone around the track, it is particularly efficient at rejecting heavy flavour (HF) jets faking

leptons, but tends to spare photon conversions. As a consequence, the relative composition of the non-prompt leptons is now very different in the tight region with respect to the loose where these cuts are not applied. In the loose region, non-prompt lepton fakes from heavy favour are dominant (90%), while after tight lepton requirement, a large fraction of photon conversion fakes emerges (up to 40%).

The Matrix Method, fake factor and ABCD methods are all relying on the usage of data events in low njets and loose lepton control regions, and are then badly biased. This bias gets even worse for some kinematical regions of discriminating variables that are used as training inputs for the multi-variate analyses (MVA). Studies on the Monte Carlo truth of same sign leptons events show photon conversion fakes and HF non-prompt fakes can have very different shapes, for instance the $\Delta R = \sqrt{\Delta\phi^2 + \Delta\eta^2}$ between the two leptons $\Delta R_{\ell\ell}$. In order to solve this problem, additional selection criterium like $\Delta R_{\ell\ell} > 0.5$ was applied (for events with at least one electron fake candidate) to exclude the region highly enriched in conversions. But that measure might not be sufficient to ensure a reliable fake estimate.

Given the limitations of the Matrix Method to handle the different mixture in control regions and signal regions, an alternative fakes estimate method has been developed : the template fit method. In this method, the normalisation of the different types of fakes are left free-floating in a fit to data, while the kinematic distributions (*templates*) of each background type is taken from Monte Carlo. The template fit method is therefore a semi-data-driven method.

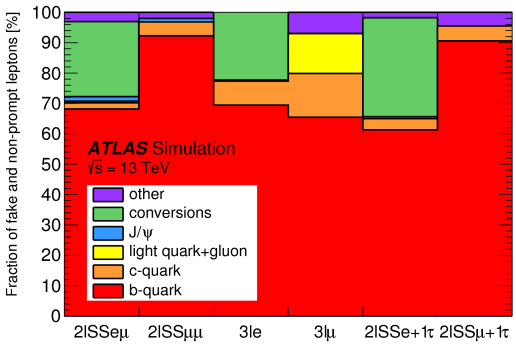

FIGURE 7.1 – Origin of non-prompt electrons and muons in various signal and control regions [62].

The main contribution to non-prompt lepton background comes from $t\bar{t}$, followed with a much smaller contribution by V+jets and single top. The truth classification of events containing a non-prompt lepton can be described as follows :

— Prompt leptons : leptons from Top , Bremsstrahlung radiation or rare Top decay.

— Conversion : Conversion photon fakes to electron

— B decay : non-prompt leptons from B decay

— C decay : non-prompt leptons from C decay

— Other decay : leptons from light quarks or other processes.

In the objective of understanding the origin of this large expected contribution from photon conversions, more advanced studies revealed that ATLAS reconstruction software requests a minimum of 20 mm radius for a conversion to be reconstructed as such. That choice was made because of the traditional $\gamma \rightarrow e^+e^-$ conversions needing material and thus not happening in

the vacuum of the beampipe. However it is found that many events with low $\Delta R_{\ell\ell}$ are actually conversions at a smaller radius. They arise from so called internal conversions (as opposed to material conversions or external conversions), where a γ^* is radiated by partons from the initial or final state (ISR/FSR) at the interaction point. These conversions are predicted by $t\bar{t}$ standard generator, Powheg+Pythia8, through the photon splitting provided by Pythia8. They can also arise from rare top decays $t \to bWl^+l^-$ which overlap with the standard $t\bar{t}$ but which invariant mass is that of the top, while it is above m_t for the $t\bar{t}\gamma^*$ [93].

The event topology where a $t\bar{t}$ event with a conversion can enter the signal region is typically a true lepton coming from one of the tops decaying leptonically, and the other same sign lepton is from a $\gamma^{(*)} \to e^+e^-$ conversion where one electron was lost. These events can be therefore drastically reduced (or exploited) by adding a cut on (or fitting) the number of tracks associated to the electron, peaking at 1 for a prompt electron, and peaking at 2 for a conversion. Another way to further reduce background from internal conversions is to apply a cut either on $M_{\ell\ell}$ or $\Delta R_{\ell\ell}$ both close to 0 for the dominant case of internal conversions with a low mass, virtual, off-shell γ^*.

Based on the truth classification stated above, the following main contributions are distinguished, and a free-floating normalisation factor (NF) is assigned to each of them :

- NF_e^{extCO} : normalisation factor applied to events with one fake electron from photon conversion. External conversions are defined as having a radius r>20 mm and a mass of tracks at the conversion vertex $0 < m(trk - trk)@CV < 100$ MeV
- NF_e^{intCO} : normalisation factor applied to events with one fake electron from photon internal conversion defined as not being external and having an invariant mass of tracks at the primary vertex $0< m(trk - trk)@PV < 100$ MeV
- NF_e^{HF} : normalisation factor applied to events with one non-prompt electron from B, C decay, or light hadron (dominated by B decay).
- NF_μ^{HF} : normalisation factor applied to events with one non-prompt muon from B decay, C decay or light hadron (dominated by B decay).
- NF_{ttW} : this additional normalisation factor is added to the fit because of the large contamination from $t\bar{t}W$ in the low jet multiplicity same sign control region used to derive the above three normalisation factors. The constriction power of this normalisation factor would benefit from the simultaneous fit of $t\bar{t}W$ enriched regions. The extraction of such regions is discussed in section 7.2. Furthermore, it is found that $t\bar{t}H \to$ ML regions select so much $t\bar{t}W$ process that free-floating its normalisation would result in a very efficient standard model measurement of the $t\bar{t}W$ cross section.

Additionally, due to the higher probability for the sub-leading lepton based on p_T to be the non-prompt, control regions are split into the ones enriched in muon fakes ($\mu\mu$ and $e\mu$ events) and the ones enriched in electron fakes (ee and μe). The fit can also be done separately in bins of b-tagged jets for the subleading electrons categories $N_B = 1, 2$ to provide additional discrimination between conversions and HF non-prompt electrons.

To better handle the normalisation of backgrounds, signal-depleted low jet multiplicity regions ($N_{jet} = 2, 3$) are considered. The low jet multiplicity region provides high statistics control regions enriched in non-prompt leptons from semileptonic b-decays. The lepton identification applied to both same sign leptons are as tight as those of the signal region to better reflect the composition. Leptons are therefore tightly identified and isolated, they also undergo the prompt lepton veto algorithm that is the upgrade of the prompt lepton isolation described in section 5.1.5. Finally

they also must pass the ambiguity flag described in section 2.1 to further reduce the conversion contribution.

In the 1 b-tag low N_{jets} ee+μe region the fit is done on the ΔR_{ll} variable to provide discrimination between conversions and HF fakes.

In the 2 b-tag low N_{jets} ee+μe and $\mu\mu$+eμ regions, the scalar sum H_T^{lep} of all leptons p_T is fitted in the two other regions to provide some discrimination against $t\bar{t}W$.

In high N_{jets} $2\ell_{SS}$ regions, a two-bin shape based on the sign of the same sign lepton pair (either ++ or –) is fitted in order to take advantage of $t\bar{t}W$ production charge asymmetry and allow discrimination against the abundantly present $t\bar{t}W$ background.

To summarise, the fit of the five aforementioned normalisation factor is performed simultaneously on 17 regions which discriminant is specified into brackets :

- ◇ High N_{jets} (≥ 4) heavy flavour $2\ell_{SS}$ related control regions (3) :
  - ▷ $t\bar{t}$ control region for ee+μe (++ ; –)
  - ▷ $t\bar{t}$ control region for $\mu\mu$+eμ (++ ; –)
  - ▷ $t\bar{t}W$ control region (++ ; –)
- ◇ Low N_{jets} (=2,3) heavy flavour $2\ell_{SS}$ related control regions (3) :
  - ▷ $t\bar{t}$ 1-b control region for ee+μe ($\Delta R_{\ell\ell}$)
  - ▷ $t\bar{t}$ 2-b control region for ee+μe (H_T^{lep})
  - ▷ $t\bar{t}$ control region for $\mu\mu$+eμ (H_T^{lep})
- ◇ Conversions dedicated control regions which definition follows that given for normalisation factors (4) :
  - ▷ External Conversion $2\ell_{SS}$ (counting)
  - ▷ External Conversion 3ℓ (counting)
  - ▷ Internal Conversion $2\ell_{SS}$ (counting)
  - ▷ Internal Conversion $2\ell_{SS}$+τ_{had} (counting)
- ◇ Signal regions (3) :
  - ▷ $2\ell_{SS}$ signal region (BDT against $t\bar{t}V$)
  - ▷ 3ℓ signal region (BDT from multiclass)
  - ▷ $2\ell_{SS}$+τ_{had} signal region (counting)
- ◇ 3ℓ control regions from multiclass BDT (4) :
  - ▷ $t\bar{t}$ (BDT from multiclass)
  - ▷ $t\bar{t}W$ (counting)
  - ▷ $t\bar{t}Z$ (counting)
  - ▷ VV diboson (counting)

The fits being performed on data, the blinding policy imposes a two-step study where a first set of the normalisation factors is derived from a fit to signal-depleted low jet multiplicity region and do not free-float the $t\bar{t}H$ signal strength. After validation of the method and unblinding approval only will the simultaneous fit be performed and provide its final values.

A simultaneous fit is preferred to a fit to the CR with an application of the normalisation factors in the SR (MVA application region) in order to insure a coherent treatment of all of the systematics correlations, both instrumental and modelling.

Due to the complexity of the fit described above, many checks must be done to understand the behaviour of normalisation factors and their dependence in particular to pile-up conditions and statistical fluctuations in the data. As of the date of edition of this thesis, issues concerning the management of this matter are still in the process of being understood.

7.2 Reduction of the irreducible backgrounds and further sensitivity improvement

The other issue is the tackling of the irreducible $t\bar{t}W$ and $t\bar{t}Z$ backgrounds. Thanks to a new version of the Prompt Lepton Isolation tool, reducible background can be more tightly cut away from the signal region. As a consequence the main purpose of multi-variate analyses becomes the separation of $t\bar{t}H$ and $t\bar{t}V$ (as well as diboson for 3ℓ) through event topology, angular variables and objects multiplicity.

The simultaneous fit of $t\bar{t}V$ normalisation provided by the template fit fake estimate method described in section 7.1 is all the more beneficial once $t\bar{t}W$ control regions are defined. In particular, the multiclass BDT used in the 3ℓ analysis already defined such a control region. The $t\bar{t}V$-vs-$t\bar{t}H$ BDT from the $2\ell_{SS}$ analysis, previously averaged with the $t\bar{t}$-vs-$t\bar{t}H$ BDT, would instead benefit from having its lowest BDT-score bin being used as a $t\bar{t}W$ control region. $2\ell_{SS}+\tau_{\text{had}}$ has lower statistics, and does not have a specifically designed $t\bar{t}W$ control region yet, but can benefit from those from 3ℓ and $2\ell_{SS}$ because of their final state vicinity. Although seemingly optimal, this new solution raises the conceptual problem of effectively measuring not only the $t\bar{t}H$ component, but also constraining the Standard Model value of the $t\bar{t}W$ process which already has a dedicated analysis and with which compatibility must be insured.

One side of the project is to re-orient categorisation and multivariate analyses towards the rejection of irreducible backgrounds. That is being done for the $2\ell_{SS}+\tau_{\text{had}}$ channel in two ways, one with a BDT and one with a simpler categorisation. With increasing statistics, that formerly historically low statistics channel now selects a sufficient number of events for shapes of discriminating variables to be checked in control regions and used in multi-variate analyses. In the future, higher level discriminating variables can be built, and for that purpose two different strategies can be confronted. One consists in building reconstruction variables. There is a french effort in that direction particularly from Clermont-Ferrand institute, with whom a collaboration is foreseen. Their preliminary studies show a combination of several methods seems very promising. First the use of a reconstruction BDT, which, on the contrary to the classification BDT used to increase the significance, is optimised to pick the most probable association of objects to their mother particle, in particular Ws from the top or the Higgs decay. That first step is not sufficient to create a discriminating variable but is necessary to decrease the number of combination to be tested in the second algorithm. That second algorithm is a Matrix Element Method (MEM).

In the MEM, the likelihood for a given event to be signal or background is a function of the parton distribution function, the theoretical matrix element, and the cross sections after the analysis cuts and efficiencies, as illustrated in Equation 7.2. For invisible particles like neutrinos, the quadrivector must be integrated over the whole phase space. In order to take into account detector resolution, transfer functions should be included and integrated over since the matrix element is a function of the truth as opposed to reconstructed particles quadrivectors. In the limit where the quadrivectors for each object in the final state are assigned to the right truth particle and known with perfect accuracy, the quantity calculated in this manner is the optimal test statistic. Hence, in optimal conditions, the MEM should be the most sensitive analysis possible.

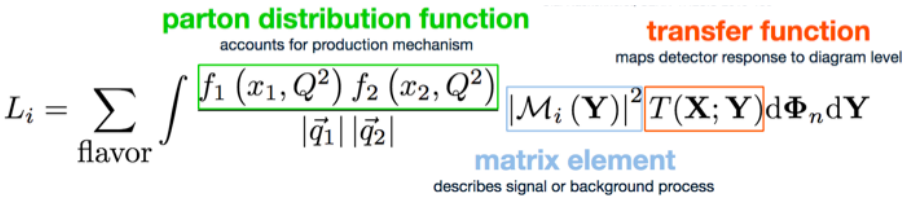

FIGURE 7.2 – Matrix element method formula.

The biggest advantage of event reconstructions techniques is that discriminants can be fully understood with physics. Built variables use physics theory predictions as inputs through the simulation, which make sense, is transparent and can be understood by the user.

The biggest limitation of the event reconstructions method is the computing time. And another parameter to be taken into account is the a priori unknown gain in discrimination of such methods. They have in the past, for other multilepton channels, sometimes been used (like the pseudo-Matrix element method for the 4ℓ channel), sometimes be dropped because of a too demanding computing time (like in $2\ell_{SS}$), and sometimes been dropped because not bringing any additional sensitivity compared to other simpler variables in the BDT (like it has been the case for the 3ℓ channel). The time investment in those techniques must therefore be carefully assessed.

Another possible strategy consists in using the higher statistics of collected data events to train low-level inputs BDT and let the algorithm decide of its high-level discriminating outputs. That second orientation can be related to a form of deep learning. As far as deep learning techniques go, data statistics is the key. In order to disentangle $t\bar{t}H$ and $t\bar{t}V$ processes, training must be done on simulated events. Hence the need to come up MC with smarter filters, like for instance a τ_{had} requirement in the $t\bar{t}$+X simulations.

The advantage of advanced machine learning methods is that with the right settings, the machine should manage to find the best combination of information required to the classification problem at hand with the minimum of central processing units (CPU), as opposed to the event reconstruction that needs to be oriented by the user and can be incomplete. The drawback from the use of deep learning algorithms in physics is its obvious lack of transparency, and on a more anthropocentric tone, the loss of initiative from the physicist. These obstacles can be overcome when realising that a backward-engineering review is needed to understand the algorithm, through the correlations of the output with known high level variables. Under that condition, one can be favour of exploiting the resources brought by current artificial intelligence progress and compare the relative benefits of human-mind-constructed and machine-build high level discriminating variables.

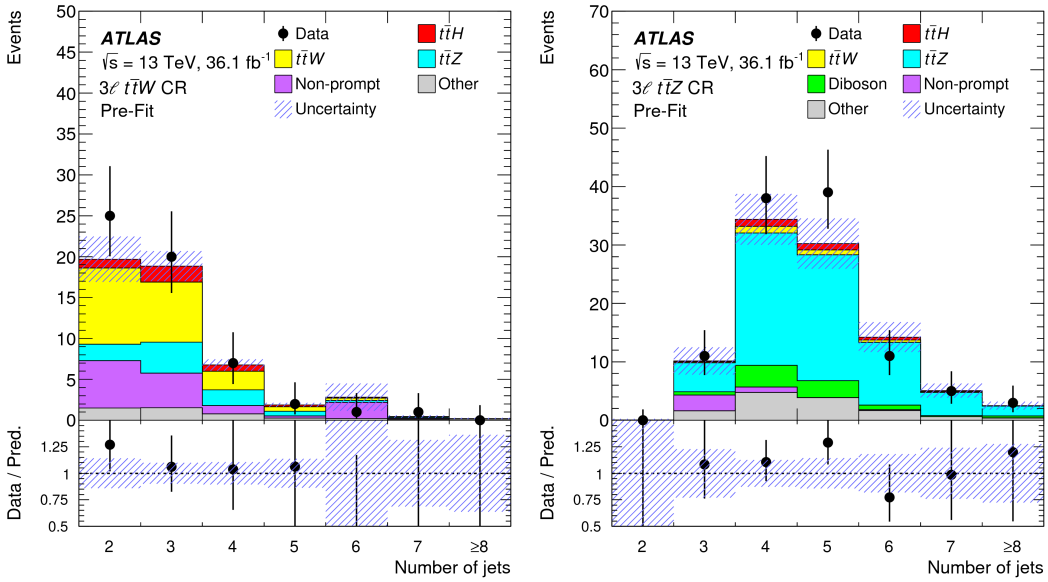

(a) $t\bar{t}W$ CR (b) $t\bar{t}Z$ CR

FIGURE 7.3 – $t\bar{t}W$ and $t\bar{t}Z$ control regions as defined and used from the multiclass 3ℓ analysis [62].

8. Improvement on the performance of objects reconstruction

After $t\bar{t}H$ modelling uncertainties, jet energy scale and resolution are the dominant systematics of the multilepton analysis. This counter intuitive importance for a final state focused on leptons is due to the high jet multiplicity of the considered final states, the omnipresence of jets whatever the lepton multiplicity, the full correlation of jet related systematics across final states, and the fact that electro-magnetic and muon systematic uncertainties are for instrumental reasons smaller than those of hadronic objects.

The future of this analysis and many others also therefore passes through the improvement of reconstruction and identification performance. A good jet resolution is also a key ingredient for the identification of an HH signal on top of the large non-resonant background which is a project developed in section 9.2. The project developed below, for which the LPSC has a leading role, is that of unifying two methods, particle flow at low jet p_T and TCC at high jet p_T. This merging into a unique jet collection represents a double advantage for ttH analyses, the first one being to feed a more optimal and simple jet reconstruction to the analysis, and the second one is to improve large-R jet reconstruction and pave the way to future inclusions of boosted category in the search for new physics in dedicated corners of the phase space.

The study of large-R jets is particularly relevant to heavy particles which decay product hadronic showers overlap and are reconstructed in one large-R jet because of a large boost. That applies for instance to $H \to b\bar{b}$, H$\to W(qq)W^*(qq)$ and t$\to W(qq)b$ decays. The distribution of energy inside a jet or *jet substructure* contains information that can be used for the discrimination of W, Higgs, and top jets against multi-jet QCD background originating from gluons or light quarks. In the simple example of a hadronically decaying vector boson V (W or Z boson), V$\to$qq, the two quarks become increasingly collimated as the parent particle becomes more energetic, following the approximation $\Delta R \simeq 2m_V/p_T$ where m_V and p_T are the mass and transverse momentum of the vector boson and $\Delta R = \sqrt{\Delta\phi^2 + \Delta\eta^2}$ their angular size. Up to recently, ATLAS was mostly using calorimeter-based jet substructure, which works well for jets initiated by particles with low to moderate boost, but is not suited to highly boosted regime.

Several methods now exist to include information from the tracker that allow to better resolve jet substructures.

At low p_T, the use of particle flow techniques [94] can improve jet angular and energy resolution by removing the calorimeter energy deposits from charged hadrons during jet reconstruction, and instead using measurements of their momenta from the inner tracker, while the calorimeter measurements of neutral-particle energies is kept. Particle flow also provides an effective suppression of jets originating from pile-up interactions by an order of magnitude within the tracker acceptance, with negligible inefficiency for jets from the hard-scatter interaction. It is efficient at

transverse momenta up to $\simeq$ 100 GeV. At higher p_T, clusters from various objects are more and more overlapping which creates confusion at the cell subtraction stage and causes particle flow performance to degrade to being slightly worse than standard reconstruction.

At higher p_T, one of the most efficient techniques to reconstruct jets is called the Track-CaloCluster (TCC)[95] method, that builds a new quadrivector using topoclusters for the energy scale component, exploiting the excellent calorimeter energy resolution, while using the track parameters to determine the angular (η, ϕ) coordinates, benefiting from the high tracker spatial resolution. Another algorithm designed to improve resolution for both jet mass and substructure variables are track assisted techniques for substructures (TAS)[96]. TAS algorithms use tracks whose p_T is scaled using calorimeter information to calculate mass and other substructure observables for standard large-R jets (jets with a large R = radius). They are called "assisted" techniques because the momentum of tracks from charge particles is "assisted" by additional calorimetric information on neutral jet components to which the tracker is not sensitive. The performance of TAS can be further improved by applying local corrections from particle flow or TCC when assisting tracks, instead of using a more traditional calorimetric only jet definition. This new type of object unifying tracking and calorimeter information, can then be an input to jet reconstruction. At very high p_T, even the tracking efficiency and accuracy is degraded due to the finite angular resolution of the detector, so both TCC and p-flow techniques that are relying on it are meeting limitations.

The objective is to merge both techniques, particle flow at low p_T and TCC at higher p_T, in order to have only one collection of jets most performant on the whole spectrum. At LPSC Grenoble, the team has strong expertise in jets reconstructions and is involved in the linking of these two techniques for improvement of the performance at medium jet p_T, the region of interest of many analyses. Such techniques promise to increase the sensitivity of the ATLAS physics program.

9. Future of Higgs boson couplings measurement

In this chapter, longer term future developments of the aforementioned Higgs couplings measurement endeavour will be discussed. Firstly, the future of the top Yukawa coupling with data from the high luminosity LHC will be broached in section 9.1. Finally, as a continuity of the discussion on the general Higgs couplings measurements developed in section 6.1.4, the ultimate project of measuring the Higgs coupling with itself is addressed in section 9.2.

9.1 Yukawa and couplings of Higgs boson to other particles

As far as the measurement of the Yukawa coupling of the Higgs boson to the top quark goes, the only existing high luminosity LHC $t\bar{t}H$ extrapolations concern the $\gamma\gamma$ final state [97]. Indeed $b\bar{b}$ and ML, respectively $t\bar{t}H$ leading final states during run 1 and run 2, were discarded from those studies for two main reasons :

— $t\bar{t}H \rightarrow \gamma\gamma$ is one of the only final state together with $t\bar{t}Z \rightarrow ZZ \rightarrow 4\ell$ to be solely limited by statistics instead of systematics, meaning they are the one that will benefit the most from the accumulated integrated luminosity. In comparison, $b\bar{b}$ and ML final states that are limited by systematic uncertainty will contribute by far less to the final statistical power of the combination at 3000 fb^{-1} of 14 TeV data.

— The sources of the dominant systematic uncertainties at work in $b\bar{b}$ and ML are difficult to extrapolate because of the unpredictable behaviour of their dominant background at higher pile-up. That is in particular true for the non-prompt fake estimates in ML, that has already proven its potential for unexpected issues, due to conversions for instance (see section 7.1). For the $b\bar{b}$ final state, systematics uncertainty control is highly dependent on the accuracy of predictions for its dominant background $t\bar{t}b\bar{b}$ which evolution is not clear to experimentalists.

  On the contrary, the $\gamma\gamma$ and the 4ℓ signatures systematics are mostly related to very well handled electromagnetic and muon-related systematics, which performance we can expect to at least not degrade and at best improve thanks to higher granularity trigger system readout to be installed during phase I and the upgrade of all of its electronics during phase II (see Figure 1.1).

Now that all Higgs production and decay modes have been observed as already discussed in section 6.1.4, constraining the Higgs sector goes through the increase of precision on the couplings measurement. Current values of uncertainty of the coupling on each particle (from ATLAS only) are roughly 20% for κ_b, 15% for κ_τ, 10% for κ_t, 8% for κ_W and κ_Z, and 7% for κ_γ and κ_g. These

values are expected to shrink with 3000 fb^{-1} of 14 TeV data to, depending on the systematic uncertainty scenario, to 2-3% for κ_γ, κ_W and κ_Z, 3-4% for κ_g and κ_τ, 4-6% for κ_b and κ_t, and $\simeq$7% for κ_μ, values roughly agreeing for CMS [98] and ATLAS [99] projections.

9.2 Higgs self-coupling measurement

Ultimately, as discussed in section 6.1.4, the goal of the $t\bar{t}H$ analysis is the measurement of the Yukawa coupling of the Higgs boson to the top quark, which is the largest of its couplings, and more generally the search for deviations from the Standard Model in any particle to the Higgs boson. But beyond the coupling of any particle to the Higgs boson, the Higgs self-coupling, discussed in equation 1.7, allows a very good test of it being Standard Model. This measurement suffers from low statistics at the LHC center of mass energy because it requires for the Higgs boson to be produced in an excited state above 250 GeV to allow for the $H \rightarrow HH$ decay. The process is made even rarer than $t\bar{t}H$ which final state weighs 475 GeV, because of the HH production diagram presenting a loop, and because of a destructive interference between the triangle and box top loop diagrams, as illustrated on Figure 9.1.

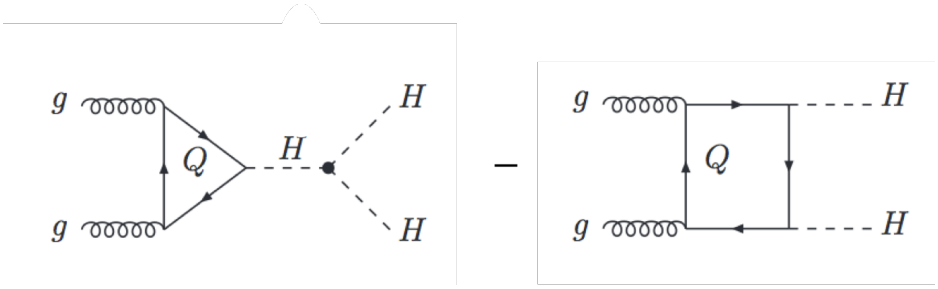

FIGURE 9.1 – Destructive interference between the two production diagrams of the di-Higgs final state.

Because of its low production rate, the HH analysis is expected to provide its full potential with the total integrated luminosity provided at the end of the exploitation period of the high luminosity LHC (HL-LHC) some time during the 2030 decade (see section 1.1). The expected integrated luminosity recorded then should be at the order of three thousand of inverse femto barns or three inverse atto barns 3000 $fb^{-1} = 3\ ab^{-1}$

To compensate for its low production rate, final states with at least one of the Higgs decays into a pair of bottom quarks following the largely dominant branching ratio. Depending on the decay of the other Higgs, different advantages are provided by various channels. The LPSC Grenoble is active in the search for $b\bar{b}\gamma\gamma$ and $b\bar{b}\tau\tau$ channels.

The ATLAS $HH \rightarrow b\bar{b}\tau\tau$ [100] currently sets the world's more stringent limit on the di-Higgs production with a single channel with an upper limit on $\sigma_{HH} \times BR(HH \rightarrow b\bar{b}\tau\tau)$ assuming standard model kinematics of 30.9 fb, that is 12.7 times the SM expectation at 95% CL with 36.1 fb^{-1} of 13 TeV data. Two channels are defined, one for which both τ being hadronic ($\tau_{had}\tau_{had}$) and one where one of the taus decays leptonically ($\tau_{lep}\tau_{had}$). For both channels a BDT (see section 5.2) is trained using kinematic variables such as the invariant mass of the di-Higgs mass, the di-τ system, the two b-jets invariant mass or the ΔR between the two τ decay products or the two b-jets. In recent extrapolation studies [101], it is found that the analysis can set an upper limit of 0.99 times the SM expectation with 3000 fb^{-1} of 14 TeV data for a scenario where

the instrumental systematics remain unchanged at the exception of the b-quark identification that would improve by 8% from the better performance of the upgraded tracker (ITK) to reject light jets (see section 1.2.1).

The $HH \to b\bar{b}\gamma\gamma$ [102] is the most promising channel for higher luminosity projections, thanks to its narrow $\gamma\gamma$ mass peak that provides a very clean di-Higgs signal. The analysis select events presenting two photons which invariant mass belong to a wide mass range 105 to 160 GeV mass range. Events are then split into two categories respectively called *2-tag* and *1-tag* depending on whether they have two 70% b-tagged jets (see section 5.1.4), or only one, more tighlty identified 60% b-tag jet. For the *1-tag* category, the second b-jet used to reconstruct the $H \to b\bar{b}$ invariant mass is picked thanks to a BDT relying on the vicinity of the dijet mass to that of the Higgs, and other kinematic variables namely the jet p_T, dijet p_T, dijet mass, jet η, dijet η, the $\Delta\eta$ between the selected jets, and whether the jet satisfies one of the looser b-tagging criteria. The correct jet is selected with an efficiency of 60-80%.

Each 1-tag and 2-tag category is further split into a loose and a tight categories. In the loose selection, the highest-p_T jet is required to have p_T>40 GeV, the sub-leading p_T jet must satisfy p_T>25 GeV, with the invariant mass of the jet pair (m_{jj}) required to lie between 80 and 140 GeV. For the tight selection, the leading and sub-leading jets are required to have p_T>100 GeV and p_T>30 GeV, and 90 GeV $< m_{jj} <$ 140 GeV. A profile likelihood fit is then performed simultaneously on the four categories.

The limit observed (expected) upper limit on the di-Higgs production rate times branching ratio $\sigma_{HH} \times BR(HH \to b\bar{b}\gamma\gamma)$ is 0.73 (0.93) pb which corresponds in terms of multiple of the SM production cross-section to an observed (expected) limits of 22 (28). Fixing all other SM parameters to their expected values, the Higgs boson self-coupling is constrained at 95% CL to -8.2< $\kappa_\lambda = \lambda_{HHH}/\lambda^{SM}_{HHH}$ <13.2 whereas the expected limits are -8.3< κ_λ <13.2. The expected allowed range at 95% CL for λ^{SM}_{HHH} with 3000 fb^{-1} of 14 TeV data including systematic uncertainties is $-1.4 < \lambda_{HHH}/\lambda^{SM}_{HHH} < 8.2$ [101].

The Standard Model analysis described here is non resonant. A beyond standard model resonant analysis also exist, that is searching for Kaluza-Klein gravitons or heavy H bosons decaying in two 125 GeV Higgs bosons. This analysis is very similar to the SM one and described in the same note [102].

All information about physics at the HL-LHC (High-Luminosity) and perspectives for the HE-LHC (High-Energy LHC) is summarised in the a HL-LHC Technical Design Report (TDR) citeATL-PHYS-PUB-2019-006.

The $HH \to b\bar{b}\gamma\gamma$ run 2 analysis has potential to be greatly improved with the introduction of more elaborate techniques, in particular the ones evoked in section 7.2 : the event reconstruction through matrix element method, and a deeper usage of machine learning techniques. Contributing to its optimisation is one of the leading projects of the LPSC ATLAS team, and has already started.

Appendices

A. $2\ell_{SS}+\tau_{\text{had}}$ event displays

Event displays of $2\ell_{SS}+\tau_{\text{had}}$ events from the Run 1 (Figure A.1) and Run 2 (Figure A.2) analyses.

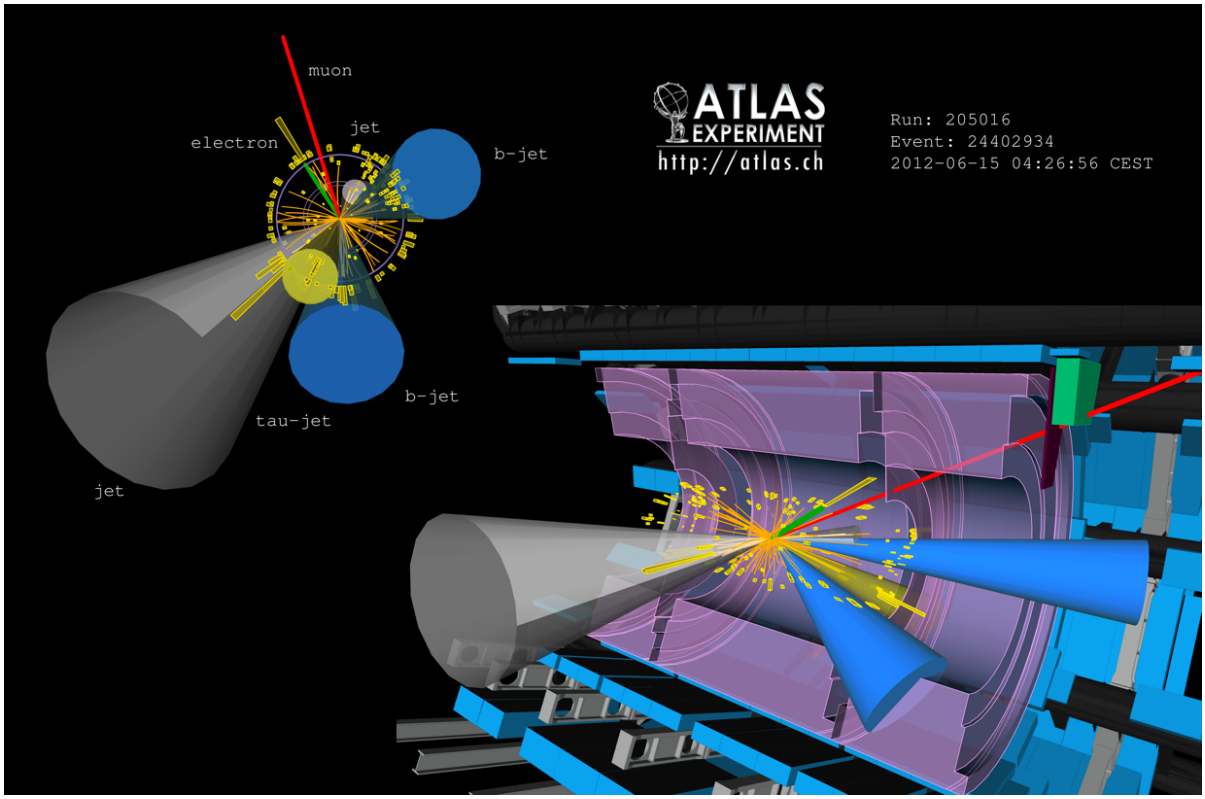

FIGURE A.1 – Event display of a $2\ell_{SS}+\tau_{\text{had}}$ event recorded in 2012 [60].

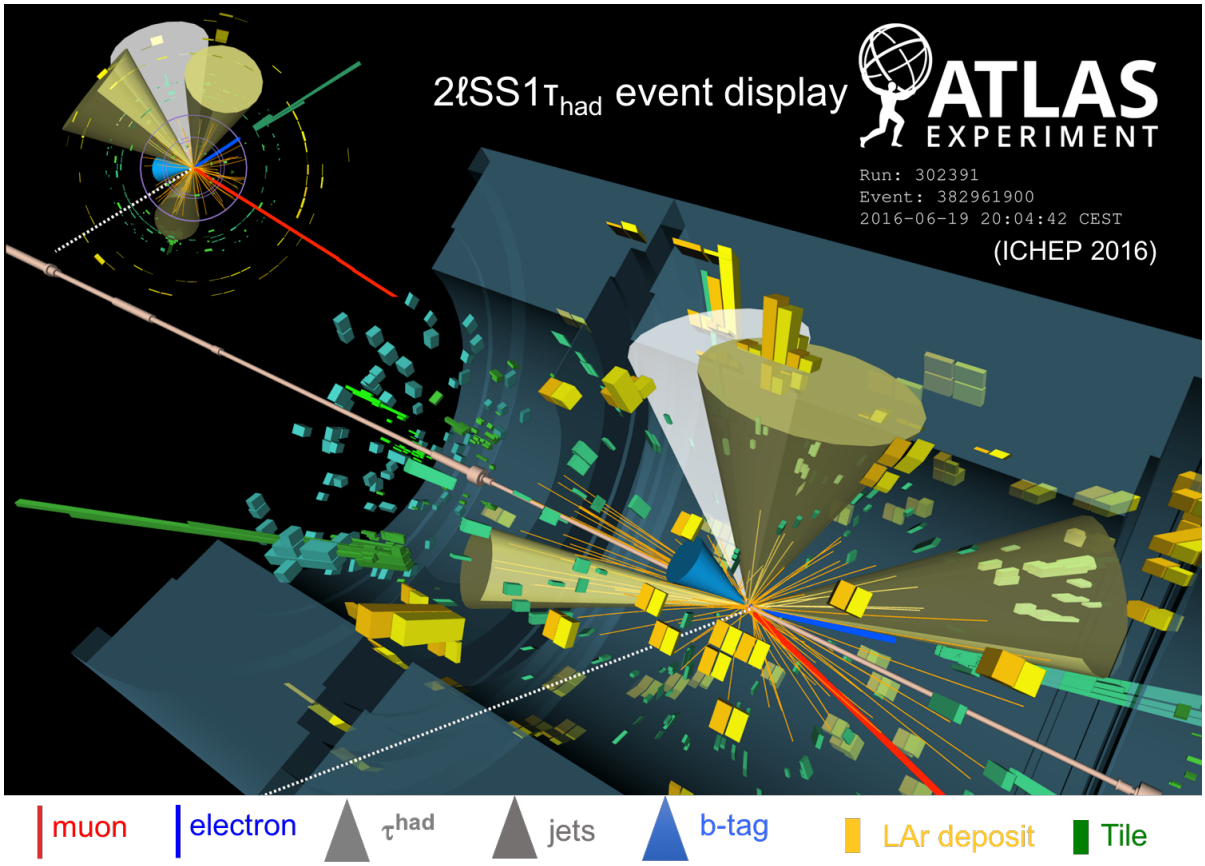

FIGURE A.2 – Event display of a $2\ell_{SS}+\tau_{\text{had}}$ event recorded in 2016 [61].

Bibliographie

[1] M. Kuna. *ATLAS electromagnetic calorimeter and electron reconstruction commissioning with the first LHC collision data. Study of the W‘ heavy gauge boson decaying in an electron and a neutrino discovery potential*. http://democrite.ccsd.cnrs.fr/view_by_stamp.php?&halsid=ifm7eradbmtinrj1vqtr7mhnb7&label=CPPM&langue=fr&action_todo=view&id=tel-00522254&version=1. 20/09/2010.

[2] The ATLAS Collaboration. "The ATLAS Experiment at the CERN Large Hadron Collider". In : *Journal of Instrumentation (JINST)* 3 (2008), S08003.

[3] J. Alwall et al. "The automated computation of tree-level and next-to-leading order differential cross sections, and their matching to parton shower simulations". In : *JHEP* 07 (2014), p. 079. doi : 10.1007/JHEP07(2014)079. arXiv : 1405.0301 [hep-ph].

[4] Stefano Frixione, Paolo Nason et Giovanni Ridolfi. "A Positive-weight next-to-leading-order Monte Carlo for heavy flavour hadroproduction". In : *JHEP* 09 (2007), p. 126. doi : 10.1088/1126-6708/2007/09/126. arXiv : 0707.3088 [hep-ph].

[5] T. Gleisberg et al. "Event generation with SHERPA 1.1". In : *JHEP* 02 (2009), p. 007. doi : 10.1088/1126-6708/2009/02/007. arXiv : 0811.4622 [hep-ph].

[6] Frank Siegert. "A practical guide to event generation for prompt photon production with Sherpa". In : *J. Phys.* G44.4 (2017), p. 044007. doi : 10.1088/1361-6471/aa5f29. arXiv : 1611.07226 [hep-ph].

[7] Torbjorn Sjostrand, Stephen Mrenna et Peter Z. Skands. "PYTHIA 6.4 Physics and Manual". In : *JHEP* 05 (2006), p. 026. doi : 10.1088/1126-6708/2006/05/026. arXiv : hep-ph/0603175 [hep-ph].

[8] Torbjorn Sjostrand, Stephen Mrenna et Peter Z. Skands. "A Brief Introduction to PYTHIA 8.1". In : *Comput. Phys. Commun.* 178 (2008), p. 852–867. doi : 10.1016/j.cpc.2008.01.036. arXiv : 0710.3820 [hep-ph].

[9] M. Bahr et al. "Herwig++ Physics and Manual". In : *Eur. Phys. J.* C58 (2008), p. 639–707. doi : 10.1140/epjc/s10052-008-0798-9. arXiv : 0803.0883 [hep-ph].

[10] S. Agostinelli et al. "Geant4, a simulation toolkit". In : *Nucl. Instrum. Meth.* A506 (2003), p. 250.

[11] The ATLAS Collaboration. "Luminosity determination in pp collisions at $\sqrt{s} = 8$ TeV using the ATLAS detector at the LHC". In : *Eur. Phys. J.* C76.12 (2016), p. 653. doi : 10.1140/epjc/s10052-016-4466-1. arXiv : 1608.03953 [hep-ex].

[12] The ATLAS Collaboration. *Luminosity Public Results Run 2*. https://twiki.cern.ch/twiki/bin/view/AtlasPublic/LuminosityPublicResultsRun2.

[13] The ATLAS Collaboration. *Public Event Displays*. https://twiki.cern.ch/twiki/bin/view/AtlasPublic/EventDisplayStandAlone.

[14] P. W. Higgs. "Broken symmetries, massless particles and gauge fields". In : *Physics Letters* 12 (1964), p. 132–133.

[15] F. Englert et R. Brout. "Broken symmetry and the mass of gauge vector mesons". In : *Phys. Rev. Lett.* 13 (1964), p. 321–323.

[16] P. W. Higgs. "Broken symmetries and the masses of gauge bosons". In : *Phys. Rev. Lett.* 13 (1964), p. 508–509.

[17] C. Hagen G. Guralnik et T. Kibble. "Global conservation laws and massless particles". In : *Phys. Rev. Lett.* 13 (1964), p. 585–587.

[18] P. W. Higgs. "Spontaneous Symmetry Breakdown without Massless Bosons". In : *Phys. Rev. Lett.* 145 (1966), p. 1156–1163.

[19] T. W. B. Kibble. "Symmetry breaking in non-Abelian gauge theories". In : *Phys. Rev. Lett.* 155 (1967), p. 1554–1561.

[20] M. Veltman. *Reflections on the Higgs system*. CERN-97-05, http://cds.cern.ch/record/2654857/files/CERN-97-05.pdf. 1997, p. 18–19.

[21] The ATLAS Collaboration. "Measurement of the photon identification efficiencies with the ATLAS detector using LHC Run-1 data". In : *Eur. Phys.J.C* 76, 666 (2016). arXiv : 1606.01813 [hep-ex].

[22] The ATLAS Collaboration. " Expected photon performance in the ATLAS experiment". In : *ATL-PHYS-PUB-2011-007* (2011). ATL-PHYS-PUB-2011-007.

[23] G. P. Salam M. Cacciari et G. Soyez. "The anti-k_t jet clustering algorithm". In : *JHEP* 04 (2008). CERN-PH-EP-2015-304, p. 063. doi : 10.1140/epjc/s10052-017-5004-5. arXiv : 0802.1189 [hep-ph].

[24] M. Kuna ; K. Liu ; Y. Liu ; G. Marchiori ; M. Pitt. "Measurement of the identification efficiency of isolated prompt photons with the matrix method in pp collisions at sqrt(s)=8TeV using 21 fb^{-1} of ATLAS data ". In : ATL-COM-PHYS-2013-1628 (2013).

[25] The ATLAS Collaboration. "Measurement of the isolated di-photon cross-section in pp collisions at $\sqrt{s} = 7$ TeV with the ATLAS detector". In : *Phys. Rev.* D85 (2012), p. 012003. doi : 10.1103/PhysRevD.85.012003. arXiv : 1107.0581 [hep-ex].

[26] The ATLAS Collaboration. "Measurements of integrated and differential cross sections for isolated photon pair production in pp collisions at $\sqrt{s} = 8$ TeV with the ATLAS detector". In : *Phys. Rev.* D95.11 (2017), p. 112005. doi : 10.1103/PhysRevD.95.112005. arXiv : 1704.03839 [hep-ex].

[27] C. Balazs et al. "Calculation of prompt diphoton production cross sections at Fermilab Tevatron and CERN LHC energies". In : *Phys. Rev. D* 76 (2007), p. 013009.

[28] T. Binoth et al. "A full next-to-leading order study of direct photon pair production in hadronic collisions". In : *Eur. Phys. J. C* 16 (2000), p. 311.

[29] The CDF Collaboration. " Measurement of the Cross Section for Prompt Isolated Diphoton Production in p$\bar{p}$ Collisions at $\sqrt{s} = 1.96$ TeV". In : *Phys. Rev. D* 84 (2011), p. 052006. arXiv : 1106.5131 [hep-ex].

[30] The D0 Collaboration. " Measurement of direct photon pair production cross sections in collisions at p$\bar{p}$ Collisions at $\sqrt{s} = 1.96$ TeV". In : *Phys. Lett. B* 690 (2010), p. 108.

[31] The CMS Collaboration. " Measurement of differential cross sections for Higgs boson production in the diphoton decay channel in pp collisions at $\sqrt{s} = 8$ TeV". In : *Eur. Phys. J. C* 76 (2016), p. 13. arXiv : 1508.07819 [hep-ex].

[32] Henso Abreu et al. "Background Studies for Higgs to gamma-gamma (1.08 fb^{-1} 7 TeV)". In : ATL-COM-PHYS-2011-782 (2011).

[33] Henso Abreu et al. "Search for the Higgs Boson Decaying to Two Photons with 3.43 fb^{-1} (7 TeV)". In : ATL-COM-PHYS-2011-1512 (2011).

[34] Henso Abreu et al. "Search for the Higgs Boson Decaying to Two Photons with 4.8 fb^{-1} (7 TeV)". In : ATL-COM-PHYS-2011-1600 (2012).

[35] HSG1 Working Group. "Improved analysis of the Search for the Higgs Boson Decaying to Two Photons with 4.8 fb^{-1} of 7 TeV data". In : ATL-COM-PHYS-2012-502 (2012).

[36] HSG1 Working Group. "Background Studies for the Search of Higgs Boson Decaying to Two Photons with 4.8 fb^{-1} of 7 TeV data with the ATLAS Experiment". In : ATL-COM-PHYS-2012-515 (2012). **Editor**.

[37] HSG1 Working Group. "Background Studies for the Search of Higgs Boson Decaying to Two Photons with 8TeV data (4.8 fb^{-1})". In : ATL-COM-PHYS-2012-754 (2012). **Editor**.

[38] The ATLAS Collaboration. "Observation and study of the Higgs boson candidate in the two photon decay channel with the ATLAS detector at the LHC". In : ATLAS-CONF-2012-168 (2013). **Editor**.

[39] The ATLAS Collaboration. "Measurement of Higgs boson properties in the diphoton decay channel with 36 fb^{-1} of pp collision data at $\sqrt{s}$ =13 TeV with the ATLAS detector". In : *Submitted to : Phys. Rev. D.* (2018). CERN-PH-EP-2017-288. arXiv : 1802.04146 [hep-ex].

[40] The ATLAS Collaboration. "Observation of Higgs boson production in association with a top quark pair at the LHC with the ATLAS detector". In : *Phys. Lett.* B784 (2018), p. 173–191. doi : 10.1016/j.physletb.2018.07.035. arXiv : 1806.00425 [hep-ex].

[41] The ATLAS Collaboration. "Search for the Standard Model Higgs boson in the two photon decay channel with the ATLAS detector at the LHC". In : *Phys. Lett. B* 705, Issue 5 (2011), p. 452–470. arXiv : 1108.5895v1 [hep-ex].

[42] The ATLAS Collaboration. "Observation of an excess of events in the search for the Standard Model Higgs boson in the gamma-gamma channel with the ATLAS detector". In : ATLAS-CONF-2012-091 (2012).

[43] M. Kuna ; B. Laforge ; J. Ocariz. "Fit of the Transverse Calorimetric Isolation Energy for the Higgs to Two Photons Analysis Sensitivity Improvement". In : ATL-COM-PHYS-2013-685 (2013). **Editor**.

[44] Georges Aad et al. "Electron and photon energy calibration with the ATLAS detector using LHC Run 1 data". In : *Eur. Phys. J.* C74.10 (2014), p. 3071. doi : 10.1140/epjc/s10052-014-3071-4. arXiv : 1407.5063 [hep-ex].

[45] E. Gross et O. Vitells. "Trial factors or the look elsewhere effect in high energy physics". In : *Eur.Phys.J.C* 70 (2010), p. 525–530. arXiv : 1005.1891.

[46] Glen Cowan et al. "Asymptotic formulae for likelihood-based tests of new physics". In : *Eur. Phys. J.* C71 (2011). [Erratum : Eur. Phys. J.C73,2501(2013)], p. 1554. doi : 10.1140/epjc/s10052-011-1554-0,10.1140/epjc/s10052-013-2501-z. arXiv : 1007.1727 [physics.data-an].

[47] The ATLAS Collaboration. "Observation of a new particle in the search for the Standard Model Higgs boson with the ATLAS detector at the LHC". In : *Phys. Lett. B* 716 (2012), p. 1–29. arXiv : 1207.7214 [hep-ex].

[48] LEP Electroweak Working Group. "Precision Electroweak Measurements and Constraints on the Standard Model". In : (2010). CERN-PH-EP-2010-095, FERMILAB-TM-2480-PPD, LEPEWWG-2010-01, TEVEWWG-2010-01, ALEPH-2010-001-PHYSICS-2010-001, CDF-NOTE-10338, D0-NOTE-6130, DELPHI-DELPHI-2010-001-PHYS-952, L3-NOTE-2837, OPAL-PR432, SLAC-PUB-14301. arXiv : 1012.2367 [hep-ex].

[49] The ATLAS Collaboration. "Evidence for the spin-0 nature of the Higgs boson using ATLAS data, ATLAS Collaboration". In : *Phys. Lett. B* 726 (2013), p. 120–144. arXiv : 1307.1432 [hep-ex]. url : http://atlas.web.cern.ch/Atlas/GROUPS/PHYSICS/PAPERS/HIGG-2013-01/.

[50] The ATLAS Collaboration. "Study of the spin and parity of the Higgs boson in diboson decays with the ATLAS detector". In : *Eur. Phys. J. C* 75 (2015), p. 476. arXiv : 1506.05669 [hep-ex].

[51] Yanyan Gao et al. "Spin determination of single-produced resonances at hadron colliders". In : *Phys. Rev.* D81 (2010), p. 075022. doi : 10.1103/PhysRevD.81.075022. arXiv : 1001.3396 [hep-ph].

[52] L. J. Dixon et M. S. Siu. "Resonance-continuum interference in the diphoton Higgs signal at the LHC". In : *Phys. Rev. Lett.* 90 (2003), p. 252001. arXiv : 0302233 [hep-ph].

[53] The ATLAS collaboration. "Evidence for the Higgs-boson Yukawa coupling to tau leptons with the ATLAS detector". In : *JHEP* 04 (2015), p. 117. doi : 10.1007/JHEP04(2015)117. arXiv : 1501.04943 [hep-ex].

[54] CMS Collaboration. "Observation of the Higgs boson decay to a pair of τ leptons with the CMS detector". In : *Phys. Lett.* B779 (2018), p. 283–316. doi : 10.1016/j.physletb.2018.02.004. arXiv : 1708.00373 [hep-ex].

[55] The ATLAS collaboration. "Search for the standard model Higgs boson produced in association with top quarks and decaying into a $b\bar{b}$ pair in pp collisions at $\sqrt{s} = 13$ TeV with the ATLAS detector". In : *Phys. Rev.* D97.7 (2018), p. 072016. doi : 10.1103/PhysRevD.97.072016. arXiv : 1712.08895 [hep-ex].

[56] The ATLAS collaboration. "Evidence for the H$\to b\bar{b}$ decay with the ATLAS detector". In : *JHEP* 12 (2017), p. 024. doi : 10.1007/JHEP12(2017)024. arXiv : 1708.03299 [hep-ex].

[57] The ATLAS Collaboration. "Observation of $H \to b\bar{b}$ decays and VH production with the ATLAS detector". In : (2018). CERN-EP-2018-215. arXiv : 1808.08238 [hep-ex].

[58] D. de Florian et al. "Handbook of LHC Higgs Cross Sections : 4. Deciphering the Nature of the Higgs Sector". In : (2016). FERMILAB-FN-1025-T, CERN-2017-002-M. DOI : 10.23731/CYRM-2017-002. arXiv : 1610.07922 [hep-ph].

[59] A. D. Martin et al. "Parton distributions for the LHC". In : *Eur. Phys. J.* C63 (2009). https://mstwpdf.hepforge.org/plots/plots.html, p. 189–285. DOI : 10.1140/epjc/s10052-009-1072-5. arXiv : 0901.0002 [hep-ph].

[60] The ATLAS Collaboration. "Search for the associated production of the Higgs boson with a top quark pair in multilepton final states with the ATLAS detector". In : *The European Physical Journal C* 749 (2015), p. 519–541. arXiv : 1506.05988 [hep-ex].

[61] The ATLAS Collaboration. "Search for the Associated Production of a Higgs Boson and a Top Quark Pair in Multilepton Final States with the ATLAS Detector". In : ATLAS-CONF-2016-058 (2016).

[62] The ATLAS Collaboration. "Evidence for the associated production of the Higgs boson and a top quark pair with the ATLAS detector". In : *Phys. Rev. D* 97 (2018), p. 072003. DOI : 10.1103/PhysRevD.97.072003. arXiv : 1712.08891 [hep-ex].

[63] The ATLAS Collaboration. "Measurements of the Higgs boson production and decay rates and coupling strengths using pp collision data at $\sqrt{s}$=7 and 8 TeV in the ATLAS experiment". In : *Phys. Lett. B* (2015), p. 64. DOI : 10.1140/epjc/s10052-015-3769-y. arXiv : 1507.04548 [hep-ex].

[64] The ATLAS Collaboration. "Measurements of the Higgs boson production and decay rates and constraints on its couplings from a combined ATLAS and CMS analysis of the LHC pp collision data at *sqrts*= 7 and 8 TeV". In : *JHEP* 08 (2016), p. 045. DOI : 10.1007/JHEP08(2016)045. arXiv : 1606.02266 [hep-ex].

[65] The ATLAS Collaboration. "Search for flavour-changing neutral current top quark decays t→Hq in pp collisions at $\sqrt{s}$=8 TeV with the ATLAS detector". In : *Journal of High Energy Physics* 12 (2015), p. 061. arXiv : 1509.06047 [hep-ex].

[66] ATLAS et CMS Collaborations. "Combined Measurement of the Higgs Boson Mass in pp Collisions at $\sqrt{s}$=7 and 8 TeV with the ATLAS and CMS Experiments". In : *Phys. Rev. Lett.* 114 (2015), p. 191803. DOI : 10.1103/PhysRevLett.114.191803. arXiv : 1503.07589 [hep-ex].

[67] Peter Skands Torbjörn Sjöstrand Stephen Mrenna. "A Brief Introduction to PYTHIA 8.1". In : *Comput.Phys.Commun.* 178 (2008), p. 852–867. DOI : 10.1016/j.cpc.2008.01.036. arXiv : 0710.3820 [hep-ph].

[68] Richard D. NNPDF Collaboration : Ball et al. "Parton distributions for the LHC Run II". In : *JHEP* 04 (2015), p. 040. DOI : 10.1007/JHEP04(2015)040. arXiv : 1410.8849 [hep-ph].

[69] The ATLAS collaboration. *Run 1 Pythia8 tunes*. ATL-PHYS-PUB-2014-021, https://cds.cern.ch/record/1966419. 2014.

[70] D. de Florian et al. "Handbook of LHC Higgs Cross Sections : 4. Deciphering the Nature of the Higgs Sector". In : (2016). FERMILAB-FN-1025-T, CERN-2017-002-M. DOI : 10.23731/CYRM-2017-002. arXiv : 1610.07922 [hep-ph].

[71] The ATLAS collaboration. "Muon reconstruction performance of the ATLAS detector in proton-proton collision data at $\sqrt{s} = 13$ TeV". In : *Eur. Phys. J. C* 76 (2016). CERN-EP-2016-033, p. 292. DOI : 10.1140/epjc/s10052-016-4120-y. arXiv : 1603.05598 [hep-ex].

[72] The ATLAS collaboration. *Electron efficiency measurements with the ATLAS detector using the 2015 LHC proton-proton collision data*. ATLAS-CONF-2016-024, https://cds.cern.ch/record/2157687. 2016.

[73] The ATLAS collaboration. "Electron reconstruction and identification in the ATLAS experiment using the 2015 and 2016 LHC proton-proton collision data at $\sqrt{s} = 13$ TeV". In : *Submitted to : Eur. Phys. J.* (2019). CERN-EP-2018-273. arXiv : 1902.04655 [physics.ins-det].

[74] The ATLAS collaboration. *Reconstruction, Energy Calibration, and Identification of Hadronically Decaying Tau Leptons in the ATLAS Experiment for Run-2 of the LHC*. ATL-PHYS-PUB-2015-045, https://atlas.web.cern.ch/Atlas/GROUPS/PHYSICS/PUBNOTES/ATL-PHYS-PUB-2015-045. 2015.

[75] The ATLAS collaboration. *Measurement of the tau lepton reconstruction and identification performance in the ATLAS experiment using pp collisions at $\sqrt{s}$=13 TeV*. ATLAS-CONF-2017-029, https://cds.cern.ch/record/2261772. 2017.

[76] The ATLAS Collaboration. "Topological cell clustering in the ATLAS calorimeters and its performance in LHC Run 1". In : *Eur. Phys. J. C* 77 (2017). CERN-PH-EP-2015-304, p. 490. DOI : 10.1140/epjc/s10052-017-5004-5. arXiv : 1603.02934 [hep-ex].

[77] The ATLAS collaboration. *Properties of jets and inputs to jet reconstruction and calibration with the ATLAS detector using proton-proton collisions at $\sqrt{s} = 13$ TeV*. ATL-PHYS-PUB-2015-036, https://cds.cern.ch/record/2044564. 2015.

[78] The ATLAS Collaboration. "Jet energy scale measurements and their systematic uncertainties in proton-proton collisions at $\sqrt{s} = 13$ TeV with the ATLAS detector". In : *Phys. Rev. D* 96 (2017). CERN-EP-2017-038, p. 072002. DOI : 10.1103/PhysRevD.96.072002. arXiv : 1703.09665 [hep-ex].

[79] The ATLAS collaboration. *Expected performance of the ATLAS b-tagging algorithms in Run-2*. ATL-PHYS-PUB-2015-022, https://cds.cern.ch/record/2037697. 2015.

[80] The ATLAS collaboration. *Optimisation of the ATLAS b-tagging performance for the 2016 LHC Run*. ATL-PHYS-PUB-2016-012, https://cds.cern.ch/record/2160731. 2016.

[81] The ATLAS collaboration. *Expected performance of missing transverse momentum reconstruction for the ATLAS detector at $\sqrt{s} = 13$ TeV*. ATL-PHYS-PUB-2015-023, https://cds.cern.ch/record/2037700. 2015.

[82] The ATLAS collaboration. *Performance of missing transverse momentum reconstruction with the ATLAS detector in the first proton-proton collisions at $\sqrt{s} = 13$ TeV*. ATL-PHYS-PUB-2015-027, https://cds.cern.ch/record/2037904. 2015.

[83] The ATLAS Collaboration. "Measurement of the Higgs boson coupling properties in the $H \to ZZ \to 4\ell$ decay channel at $\sqrt{s} = 13$ TeV with the ATLAS detector". In : *JHEP* 03 (2018), p. 095. DOI : 10.1007/JHEP03(2018)095. arXiv : 1712.02304 [hep-ex].

[84] A. Hoecker et al. "TMVA - Toolkit for Multivariate Data Analysis". In : (2007). CERN-OPEN-2007-007. eprint : arXiv:physics/0703039.

[85] The ATLAS Collaboration. "Measurements of Higgs boson properties in the diphoton decay channel with 36 fb^{-1} of pp collision data at $\sqrt{s} = 13$ TeV with the ATLAS detector". In : (2018). CERN-EP-2017-288. arXiv : 1802.04146 [hep-ex].

[86] CERN Yellow Report. *tH Process cross section at $\sqrt{s}$=13 TeV*. https://twiki.cern.ch/twiki/bin/view/LHCPhysics/CERNYellowReportPageAt13TeV#tH_Process.

[87] The ATLAS Collaboration. "Measurement of the Higgs boson mass in the $H \to ZZ^* \to 4\ell$ and $H \to \gamma\gamma$ channels with $\sqrt{s} = 13$ TeV pp collisions using the ATLAS detector". In : *Phys. Lett.* B784 (2018), p. 345–366. DOI : 10.1016/j.physletb.2018.07.050. arXiv : 1806.00242 [hep-ex].

[88] The ATLAS collaboration. *Combined measurements of Higgs boson production and decay using up to 80 fb^{-1} of proton-proton collision data at $\sqrt{s}$= 13 TeV collected with the ATLAS experiment*. ATLAS-CONF-2019-005. 2019.

[89] The ATLAS collaboration. "Combined measurements of Higgs boson production and decay in the $H \to ZZ^* \to 4\ell$ and $H \to \gamma\gamma$ channels using $\sqrt{s} = 13$ TeV pp collision data collected with the ATLAS experiment". In : (2017). ATLAS-CONF-2017-047.

[90] The ATLAS Collaboration. "Search for flavor-changing neutral currents in top quark decays $t \to Hc$ and $t \to Hu$ in multilepton final states in proton-proton collisions at $\sqrt{s} = 13$ TeV with the ATLAS detector". In : *Phys. Rev.* D98.3 (2018), p. 032002. DOI : 10.1103/PhysRevD.98.032002. arXiv : 1805.03483 [hep-ex].

[91] The ATLAS Collaboration. "Search for top quark decays $t \to qH$, with $H \to \gamma\gamma$, in $\sqrt{s} = 13$ TeV pp collisions using the ATLAS detector". In : *JHEP* 10 (2017), p. 129. DOI : 10.1007/JHEP10(2017)129. arXiv : 1707.01404 [hep-ex].

[92] The ATLAS collaboration. "Search for top-quark decays $t \to Hq$ with 36 fb^{-1} of pp collision data at $\sqrt{s} = 13$ TeV with the ATLAS detector". In : *JHEP* 05 (2019), p. 123. DOI : 10.1007/JHEP05(2019)123. arXiv : 1812.11568 [hep-ex].

[93] Peter Onyisi et Aaron Webb. "Impact of rare decays $t \to \ell'\nu b\ell\ell$ and $t \to qq'b\ell\ell$ on searches for top-associated physics". In : *JHEP* 02 (2018), p. 156. DOI : 10.1007/JHEP02(2018)156. arXiv : 1704.07343 [hep-ph].

[94] The ATLAS Collaboration. "Jet reconstruction and performance using particle flow with the ATLAS Detector". In : *Eur. Phys. J.* C77.7 (2017), p. 466. DOI : 10.1140/epjc/s10052-017-5031-2. arXiv : 1703.10485 [hep-ex].

[95] The ATLAS Collaboration. "Improving jet substructure performance in ATLAS using Track-CaloClusters". In : *ATL-PHYS-PUB-2017-015* (2017). ATL-PHYS-PUB-2017-015.

[96] The ATLAS Collaboration. "Track assisted techniques for jet substructure". In : *ATL-PHYS-PUB-2018-012* (2018). ATL-PHYS-PUB-2018-012.

[97] The ATLAS Collaboration. "HL-LHC projections for signal and background yield measurements of the $H \to \gamma\gamma$ when the Higgs boson is produced in association with t quarks, W or Z bosons". In : *ATL-PHYS-PUB-2014-012* (2014). ATL-PHYS-PUB-2014-012.

[98] CMS COLLABORATION. *Preliminary Higgs signal strength and coupling extrapolations for HL-LHC*. ATL-PHYS-PUB-2015-023, https://twiki.cern.ch/twiki/bin/view/LHCPhysics/GuidelinesCouplingProjections2018. 2018.

[99] *Projections for measurements of Higgs boson cross sections, branching ratios, coupling parameters and mass with the ATLAS detector at the HL-LHC*. Rapp. tech. ATL-PHYS-PUB-2018-054. ATL-PHYS-PUB-2018-054. Geneva : CERN, déc. 2018. URL : http://cds.cern.ch/record/2652762.

[100] The ATLAS COLLABORATION. "Search for resonant and non-resonant Higgs boson pair production in the $b\bar{b}\tau^+\tau^-$ decay channel in pp collisions at $\sqrt{s} = 13$ TeV with the ATLAS detector". In : *Phys. Rev. Lett.* 121.19 (2018). [Erratum : Phys. Rev. Lett.122,no.8,089901(2019)], p. 191801. DOI : 10.1103/PhysRevLett.122.089901,10.1103/PhysRevLett.121.191801. arXiv : 1808.00336 [hep-ex].

[101] *Measurement prospects of the pair production and self-coupling of the Higgs boson with the ATLAS experiment at the HL-LHC*. Rapp. tech. ATL-PHYS-PUB-2018-053. ATL-PHYS-PUB-2018-053. Geneva : CERN, déc. 2018. URL : http://cds.cern.ch/record/2652727.

[102] The ATLAS COLLABORATION. "Search for Higgs boson pair production in the $\gamma\gamma b\bar{b}$ final state with 13 TeV pp collision data collected by the ATLAS experiment". In : *JHEP* 11 (2018), p. 040. DOI : 10.1007/JHEP11(2018)040. arXiv : 1807.04873 [hep-ex].